題目(和文)	Xenonガスジェット型13.5 nm 極端紫外線プラズマ光源のZピンチダイナミクスに関する研究
Title(English)	Z-pinch Dynamics in a Xenon Gas Jet Type 13.5 nm Extreme Ultraviolet Plasma Source
著者(和文)	黄 斌
Author(English)	Bin Huang
出典(和文)	学位:博士(工学), 学位授与機関:東京工業大学, 報告番号:甲第9520号, 授与年月日:2014年3月26日, 学位の種別:課程博士, 審査員:堀田　栄喜,堀岡　一彦,奥野　喜裕,肖　鋒,藤井　隆
Citation(English)	Degree:Doctor (Engineering), Conferring organization: Tokyo Institute of Technology, Report number:甲第9520号, Conferred date:2014/3/26, Degree Type:Course doctor, Examiner:,,,,
学位種別(和文)	博士論文
Type(English)	Doctoral Thesis

TOKYO INSTITUTE OF TECHNOLOGY

DOCTORAL THESIS

Z-pinch Dynamics in a Xenon Gas Jet Type 13.5 nm Extreme Ultraviolet Plasma Source

---

Author:
Bin HUANG

Supervisor:
Prof. Eiki HOTTA

A thesis submitted in partial fulfilment of the requirements
for the degree of Doctor of Philosophy

in the

Department of Energy Sciences
Interdisciplinary Graduate School of Science and Engineering
Tokyo Institute of Technology

February 2014

“Thanks to my solid academic training, today I can write hundreds of words on virtually any topic without possessing a shred of information, which is how I got a good job in journalism.”

Dave Barry

Abstract

Extreme Ultraviolet (EUV) lithography is the leading candidate of the next generation lithography technology. To date, insufficient source power remains a critical issue for the High Volume Manufacturing (HVM) of EUV lithography. Z-pinch is an efficient method for producing the 13.5 nm EUV radiation. However, it is inherently susceptible to Magneto-Rayleigh-Taylor (MRT) instabilities, which causes the non-uniformity of the EUV radiation and degrades the output. In this thesis, both experimental and numerical investigations on the Z-pinch dynamics of an gas jet type Xenon (Xe) Discharge Produced Plasma (DPP) EUV source are presented. The EUV radiation characteristics, time-resolved visible plasma imaging, time-integrated EUV pinhole imaging, electron density evolution, and ion kinetics in decay phase are studied experimentally. The EUV radiation fluctuation caused by MRT instability with a wavelength 1 mm is observed by EUV pinhole imaging. To investigate the Z-pinch dynamics and the MRT instabilities in the DPP EUV source, a Magneto-Hydrodynamics (MHD) code is developed. Important plasma parameters for Z-pinch (e.g. electron density and electron temperature) are simulated. The evolutions of MRT instabilities with single mode, multi-mode and random mode initial perturbations are presented. The simulation shows that MRT instabilities tend to converge to a mm-scale wavelength around 1 mm, in consistence with experimental result. The MRT instabilities will cause the electron density and temperature fluctuations along Z axis at pinch stagnation, which finally lead to the non-uniformity of the EUV radiation. Preferred initial conditions and possible MRT mitigation methods are also proposed to optimize the EUV source.

Acknowledgements

Foremost, I would like to express my most sincere gratitude to my advisor Prof. Eiki Hotta for the continuous support of my Ph.D. study and research, for his patience, motivation, enthusiasm, and immense knowledge. Prof. Hotta provided me with every bit of guidance, assistance, and expertise that I needed; then, when I felt ready to venture into research on my own and branch out into new research areas, He gave me the freedom to do whatever I wanted, at the same time continuing to contribute valuable feedback, advice, and encouragement. I could not have imagined having a better advisor and mentor for my Ph.D. study. Meanwhile, I would like to thank his family members for their great kindnesses and hospitalities.

Besides, my sincere thanks also go to Prof. Feng Xiao and Prof. Yoshihiro Okuno for their help in developing the numerical code. Also, I would like to say thanks to Dr. Masato Watanabe for his cooperation and suggestions on my research. I am deeply indebted to Prof. Tohru Kawamura for his perceptive comments on my research. I am very grateful to Prof. Kazuhiko Horioka, Prof. Akitoshi Okino, Prof. Takashi Fuji, and Prof. Koushichi Nemoto. In addition, I would like to thank Prof. Qi Wang and Prof. Yongpeng Zhao in Harbin Institute of Technology, and Prof. Bill Graham in Queen's University Belfast.

I would like to express my gratitude to all the members of Hotta Laboratory. They offered me much help. Particularly, I want to thank Mr. Taku Tomizuka, Dr. Bin Xie, and Mr. Yasuhiro Takimoto for their cooperation, without them I cannot finish this research. I also thank Dr. Yusuke Sakai, Dr. Qiushi Zhu, Dr. Inho Song, Dr. Kunihiko Tomiyasu, Dr. Jia Li, Mr. Fei Jiang, Mrs. Mamie Oka, and Mr. Ryo Sugihara for their help with my study and life in Japan.

In addition, I sincerely acknowledge the financial support of the Japanese Government Scholarship from the Ministry of Education, Culture, Sports, Science, and Technology.

This scholarship is crucial to the successful completion of my study. I am also grateful to the International Training Program sponsored by Japan Society for the Promotion of Science, which gave me a chance to study in Queen's University Belfast for two months.

Finally, I am deeply thankful to my family for their love, support, and sacrifices. Without them, this thesis would never have been written.

Contents

List of Figures

List of Tables

Abbreviations

EUV	**e**xtreme **u**ltra**v**iolet
NA	**N**umerical **A**perture
IF	**I**ntermediate **F**ocus
HVM	**H**igh **V**olume **M**anufacturing
NGL	**n**ext **g**eneration **l**ithography
MLM	**m**ulti**l**ayer **m**irror
ML	**m**ulti**l**ayer
DPP	**D**ischarge **P**roduced **P**lasma
LPP	**L**aser **P**roduced **P**lasma
SMB	**S**hifted **M**axwell–**B**oltzmann
RF	**R**adio-**F**requency
IC	**I**ntegrated **C**ircuit
CE	**C**onversion **E**fficiency
MHD	**M**agneto-**H**ydro**d**ynamics
LTE	**L**ocal **T**hermodynamic **E**quilibrium
MRT	**M**agneto-**R**ayleigh-**T**aylor
CFL	**C**ourant-**F**riedrich-**L**ewy
TVD	**T**otal **V**ariation **D**iminishing
TVD-LF	**T**otal **V**ariation **D**iminishing scheme in **L**ax-**F**rieddrich formulation
MPC	**M**agnetic **P**ulse **C**ompressor
FFT	**F**ast **F**ourier **T**ransform

To my family

Chapter 1

Introduction

In this chapter, the development of EUV source and EUV lithography are reviewed. The basic physics of Z-pinch plasma are introduced, including the basic Z-pinch models, EUV emission properties, and basic concept of MRT instabilities in Z-pinch. Then, the scope and outline of this study are present.

1.1 EUV Lithography: a Historical Perspective

Photolithography is a patterning technology for the fabrication of the integrated circuits (ICs). It has been introduced to semiconductor industry since the invention of the IC in 1958. In a photolithography tool, a circuit pattern is manufactured on a mask (or reticle). Light radiates onto the mask through an illumination optical system, and projects the pattern image onto a silicon wafer through the projection optical system. The wafer is coated with photosensitive chemical photoresist in advance, or simply resist, on which, the circuit pattern is produced by the transmitted pattern image[1]. Then, after a series of chemical treatments that are used for ion implantation, removing the uppermost layer of the substrate in the areas that are not protected by photoresist, stripping the useless photoresist, plasma vapor deposition, etc. Electronic pathways are finally produced

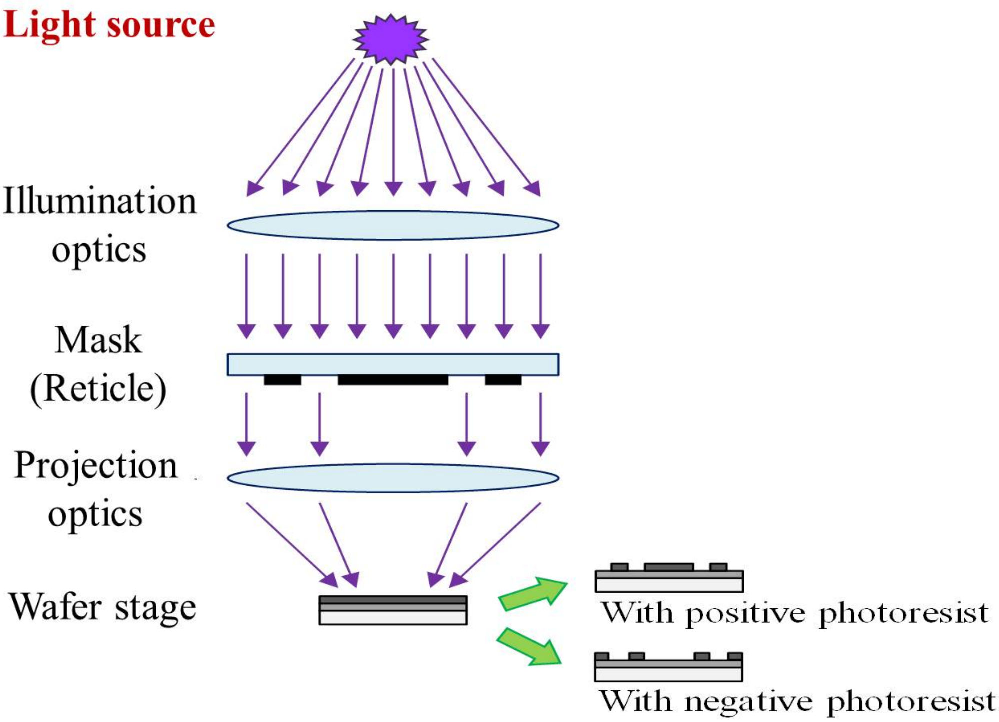

FIGURE 1.1: Schematic of optical Lithography system.

on the wafer[2]. The photolithography system and a typical working procedure are illustrated in Figs. 1.1 and 1.2.

Thanks to the advancement in the photolithography technology, during the past three decades, the number of transistors on a chip has grown exponentially, doubling on the average of every 18 months, as described by Moore in 1965[3]. The two fundamental relationships describing lithographic imaging system resolution (RES) and depth of focus (DOF) are[4]

$$RES = \frac{k_1 \lambda}{NA}, \tag{1.1}$$

and

$$DOF = \pm \frac{k_2 \lambda}{(NA)^2}, \tag{1.2}$$

where λ is the wavelength of the light source, and NA is the numerical aperture of the imaging system. The parameters k_1 and k_2 are empirically determined and take on the values that depend on the critical dimension (CD) tolerance and the size of acceptable IC manufacturing process window. As technology advanced and feature size

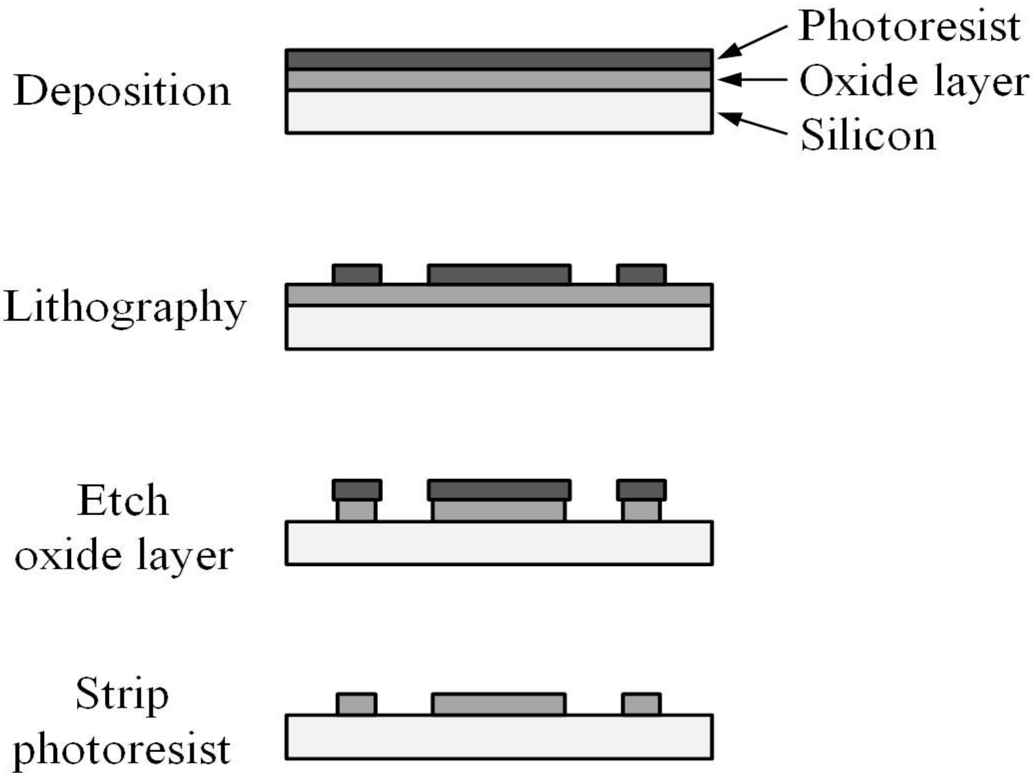

FIGURE 1.2: A simple subtractive patterning process.

shrank, the wavelength of exposure light decreased several times. Original lithography used visible g-line (436 nm) and ultraviolet i-line (365 nm) lights produced by mercury arc lamps. When IC feature size shrank to approximately half a micron, these wavelengths met a significant challenge, which gave rise to deep ultraviolet 248 nm KrF and 193 nm ArF excimer lasers for lithography. With the printed feature size of the semiconductor chips continuously decreasing and now coming under the 22 nm node, double patterning (DP) lithography based on 193 nm deep ultraviolet (DUV) lithography systems is being employed[5–7]. For smaller feature size ICs, shorter wavelength lithography, known as next generation lithography (NGL), was studied using 157 nm wavelength, extreme ultraviolet (EUV) light (i.e. 13.5 nm), x-ray (0.4 nm), and even shorter wavelengths of electron and ion beams[8]. Later, the 157 nm lithography was abandoned because the immersion exposure technology makes the 193 nm wavelength lithography feasible to be used for the 45 nm technology node. Now, the 13.5 nm EUV lithography is considered as the most promising candidate for NGL. The EUVL optics

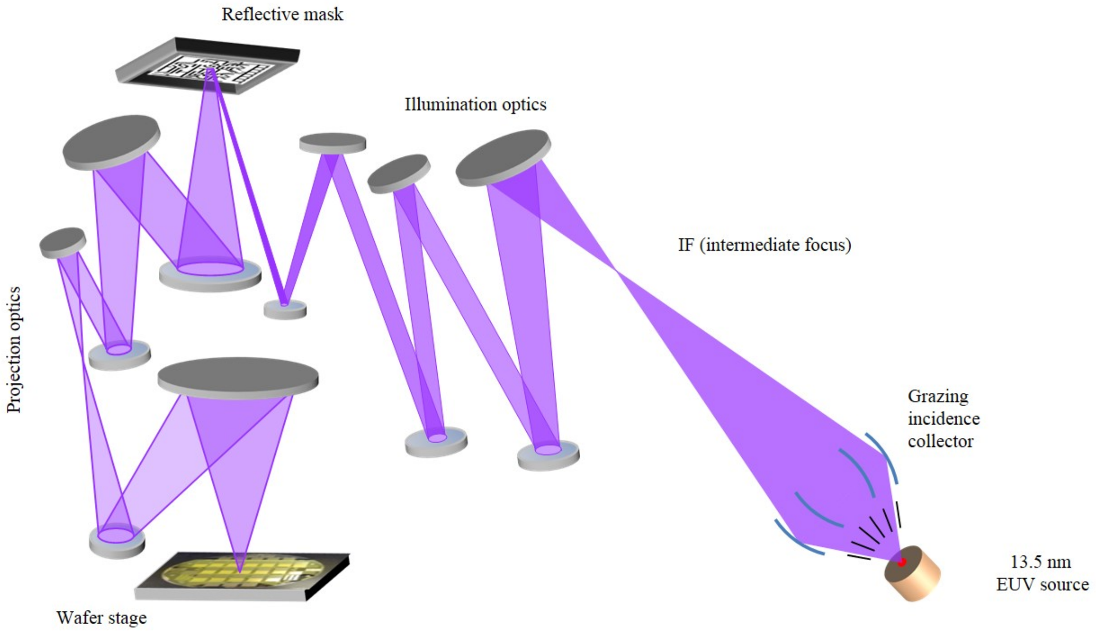

FIGURE 1.3: Schematic of EUV Lithography system

are all reflection-based systems instead of refraction-based system used in traditional photolithography systems.

Compared with other NGL methods, such as proximity x-ray lithography, electron projection lithography, and ion projection lithography, EUVL is a new member of NGLs. Because it possesses special optical advantages, known as the natural extension of optical lithography, EUVL development has been relatively fast. It provides a higher resolution and a larger depth of focus because it utilizes a shorter wavelength (13.5 nm) and employs a smaller numerical aperture (NA) imaging system ($0.93 \sim 1.35$ NA)[9] Most other NGLs require 1X membrane masks, but EUVL uses masks with four or five fold image reduction, which makes mask fabrication feasible with current technology. Reflective optics have been used in EUVL optical systems, because all available materials are strong absorbers of EUV light and no materials are transparent enough to make use of refractive optics. EUV light is reflected on multilayer mirrors (MLM), i.e., the Bragg reflectors, usually consisting of molybdenum and silicon (Mo/Si) multilayer[8]. A schematic of EUVL system proposed by ASML in 2011 is shown in Fig. 1.3[10].

The concepts for EUVL first emerged during the 1980s using soft x-rays in the 4 to

40 nm wavelength range[11–13]. The first demonstration of the technology's potential and of nearly-diffraction-limited imaging took place in 1990[14]. From 1993 to 1996, the focus of R&D work worldwide shifted from demonstrations of EUV imaging to the development of EUV imaging system that could provide larger image fields and smaller wavefront errors, and to EUVL system integration. In the early and mid-1990s, systematic research was mainly performed by the Lawrence Livermore National Laboratory (LLNL)[15–29], Sandia National Laboratory (SNL)[30–34], Lawrence Berkeley National Laboratory (LBNL)[35–38], AT&T Bell Laboratories[39–44], and several universities[45–49]. The commercialization efforts of EUVL began in early 1997 when an industrial consortium, EUV LLC, was formed by Intel, Motorola, and Advanced Micro Device. At the same time, Virtual National Laboratories was also formed by LLNL, SNL, and LBNL to conduct a program sponsored by EUV LLC.

In Europe, an industrial consortium, Extreme Ultraviolet Concept Lithography Development System (EUCLIDES), was formed in 1998 by ASM Lithography (ASML), Carl Zeiss, and Oxford Instruments. Since then, EUVL studies in Europe have made significant progress, with ASML leading. In Japan, original studies on EUVL were performed in NTT LSI Laboratories, and publications were found dating from 1989. Other EUVL pioneer work was carried out by Nikon and Hitachi around 1990. The Association of Super-Advanced Electronics Technologies (ASET) was established in 1996, launching its EUVL program in 1998. The Extreme Ultraviolet Lithography System Development Association was established in 2002. Many early EUVL studies in Japan were conducted in the 1990s[50–53]. Today, commercial EUV exposure-tool development is underway at ASML, Canon, and Nikon. A number of universities, national laboratories, and semiconductor consortia have been actively participating in EUV infrastructure development.

1.2 EUV Source for Lithography

1.2.1 EUV Source Requirements

The cost-effective implementation of EUVL in High Volume Manufacturing (HVM) has many technical challenges. To push EUVL to HVM, which produces ICs 24×7 at an acceptable cost to customers, specific requirements on the 13.5 nm EUV source should be satisfied. In 2009, three stepper manufacturers: Nikon, Canon, and ASML published the industrial requirements for 13.5 nm EUV sources on the in-band power, emission stability, contamination control, source size, collectable angle, and damages to optics. The industrial requirements for 13.5 nm EUV sources are listed in Table. 1.1[54]. The EUV power determines manufacturing capacity: the number of wafers that the stepper can process per hour. The required power is decided by the sensitivity of photoresist. For HVM, the in-band EUV power at the intermediate focus (IF) point should reach 115 W at the resist sensitivity of 5 mJ/cm^2, and 200 W at 10 mJ/cm^2. The EUV power at the IF is proportional to the luminous efficacy and the collection efficiency. High collection efficiency is guaranteed by small etendue, which is related to the size of a plasma source and the total solid angle of the lights. Based on the design of the optics, the etendue of the source should be less than 3.3 mm^{2}sr, with a solid angle input to the illuminator of less than 0.2 sr. To scale up the EUV power, achieving high repetition frequency of the light emission is one of the key issues. HVM EUVL needs the repetition rate of more than 10 kHz, with no upper limit. Beside, the repetition rate and the integrated energy stability of the light source together determine the dose uniformity of the EUV emission, which related to the final line quality on a wafer and the production yield. Thus, the integrated energy stability is required to be no larger than 0.2%. Meanwhile, the contamination (atoms, ions and clusters) from the source towards optics should also be considered, since the life time of optical components relates to the cost of the lithography. The source should be clean enough to guarantee that the optics after IF works more than 3000 hours with the reflectivity degradation of no more than

TABLE 1.1: Joint requirements for EUV sources towards HVM EUVL

Source characteristics	Requirements
Wavelength	13.5 nm
EUV power (in-band) @ IF	115 W @ 5 mJ·cm^{-2} $\sim$ 200 W @ 10 mJ·cm^{-2}
Repetition frequency	$>$ 10 kHz
Integrated energy stability	$\pm$ 0.2%, 3σ over 50 pulses
Source cleanliness (debris)	Reflectivity degradation $\leq$ 10% after 30,000 light-on hours
Etendue of source output	Max. 3.3 mm^{2}sr
Max. solid angle input to illuminator	0.03 $\sim$ 0.2 sr

10%. Moreover, since the out-of-band radiation with respect to the wavelength band of a Mo/Si multilayer mirror will degrade the line quality on resist and harm the optics by the heat load, total radiation should also be carefully controlled to reach high spectral purity at 13.5 nm within 2% bandwidth. To date, insufficient source power remains a critical issue[55]. Therefore, the development of suitable 13.5 nm EUV sources with sufficient in-band power has been the most principal issue for HVM EUVL.

1.2.2 Selection of the Exposure Wavelength

The choice of the exposure wavelength is one of the most important decision made in the field of EUVL. It influences the design of the projection optics, the peak reflectivity and bandwidth of the multilayer (ML) reflective coatings, and the performance of EUV resist materials. The primary purpose of EUVL was to develop exposure tool capable of a higher resolution and a larger depth of focus than was possible with 193 nm lithography. Due to the substantially reduced wavelength, EUVL is expected to be capable of printing significant smaller features size .

EUV generally refers to the emission with the wavelength between $\sim$5 nm (250 eV) and $\sim$40 nm (30 eV)[56]. It overlaps with a part of X-ray region. In the EUV region, the absorbance of most of known materials becomes too high to be used for fabricating refractive optical elements. Therefore reflective optics based on the ML technique has been used in the EUVL systems. ML coatings are efficient normal-incidence reflectors at EUV wavelengths from $4.5 \sim 30$ nm[57]. A ML consists of alternating layers of high-Z and low-Z materials, functioning like a quarter-wave stack, i,e., it provides enhanced reflectivity over a narrow wavelength band peaked at the Bragg wavelength, $\lambda = 2d\sin(\theta)$, where d is the ML period and θ is the angle of incidence. Generally, the highest reflectivity occurs at wavelength for which the absorption of the low-Z material in the ML is at a minimum and occurs in discrete bands near atomic absorption edges. The best low-Z materials for ML coatings are C (for wavelengths longer than 4.4 nm), B (for wavelengths longer than 6.7 nm), beryllium (Be) (for wavelengths longer than 11.3 nm), Si (for wavelengths longer than 12.5 nm), and lithium (Li) (for wavelengths longer than 23.9 nm)[58]. For practical application, the ML must provide $\sim 30\%$ or more peak reflectivity and have a bandwidth of $0.3 \sim 0.4$ nm so that the different angles of incidence on all of the mirrors in a multimirror projection optics can be matched[59].

The sensitivity and absorption depth of an EUV resist depends almost entirely on its EUV absorption coefficient. Taking into account the required resolution, DOF, ML reflectance, bandwidth and resist performance, the choice of exposure wavelength was narrowed to two wavelength regions: from 4.5 to 7 nm and from 11.5 to 13 nm[59]. The choice was narrowed to discrete wavelength bands in the vicinity of 11.3, 13, 17, and 24 nm in a later work[58]. Today, based on more practical considerations such as overall system throughput and worker safety concerns over the use of Be-based MLs in a semiconductor fab, the choice of exposure wavelength has become a narrow band of wavelength near 13.5 nm because at this wavelength, the Mo/Si ML mirrors have the highest reflectivity of 70%[9]. The cross-section TEM micrograph of a Mo/Si MLM (a) and reflectivity of Mo/Si MLM (b) are shown in Fig.1.4.

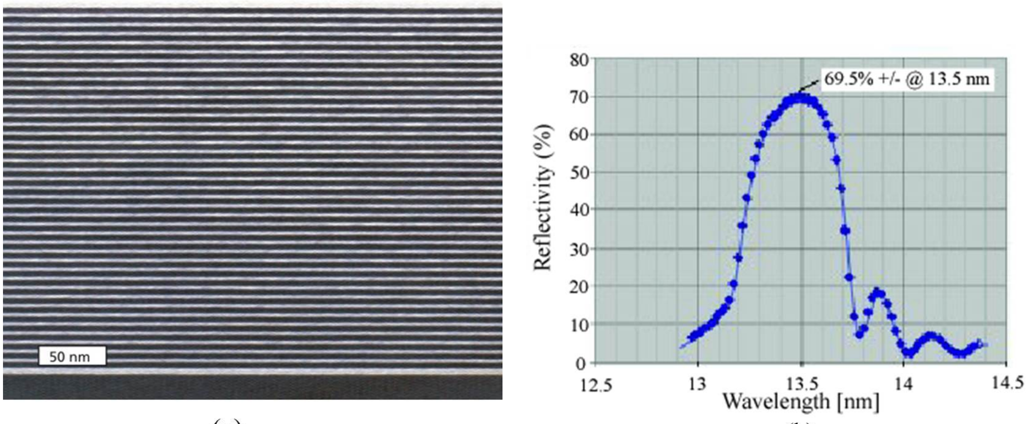

(a) (b)

FIGURE 1.4: Cross-section TEM micrograph of a Mo/Si MLM (a) and reflectivity of Mo/Si MLM (b)

1.2.3 Source Material

Since the spontaneous EUV radiation is emitted from excited ions or atoms, it is essential to find excited states with large transition probabilities. Many experiments had been done previously on X-ray-emitting plasmas, and atomic states that are preferable for 13.5 nm EUV emission were found among gases Xe, oxygen (O), and metals Li, tin (Sn). Their spectra in the 10-nm region are shown in Fig. 1.5 [60, 61]. For low-Z (atomic number) elements Li and O, the radiations in the 10-nm range are both single line emissions: Li III $1s\ ^2S - 2p\ ^2P$ and O V $1s^22s^2\ ^1S - 1s^22s4p\ ^1P$. The widths of both line emissions are much narrower than the FWHM of the reflectivity profile of a Mo/Si ML. This property limits the total energy of the in-band EUV emission, and also indicates that a very small thickness change on the multilayer leads to significantly change of the reflected light intensity. Therefore, Li and O are not considered as the proper elements for EUVL.

The EUV spectra of two other candidates, Xe and Sn, have been investigated in detail in Ref. [62–64]. The emission from Xe in the 10-nm region can be classified into two groups: the unresolved transition arrays (UTAs) of 4-4 transitions $(4d - 4f)$, mainly around 11 nm, and 4-5 transitions (Xe XI $4d - 5p$) around 13.5 nm. However, comparing

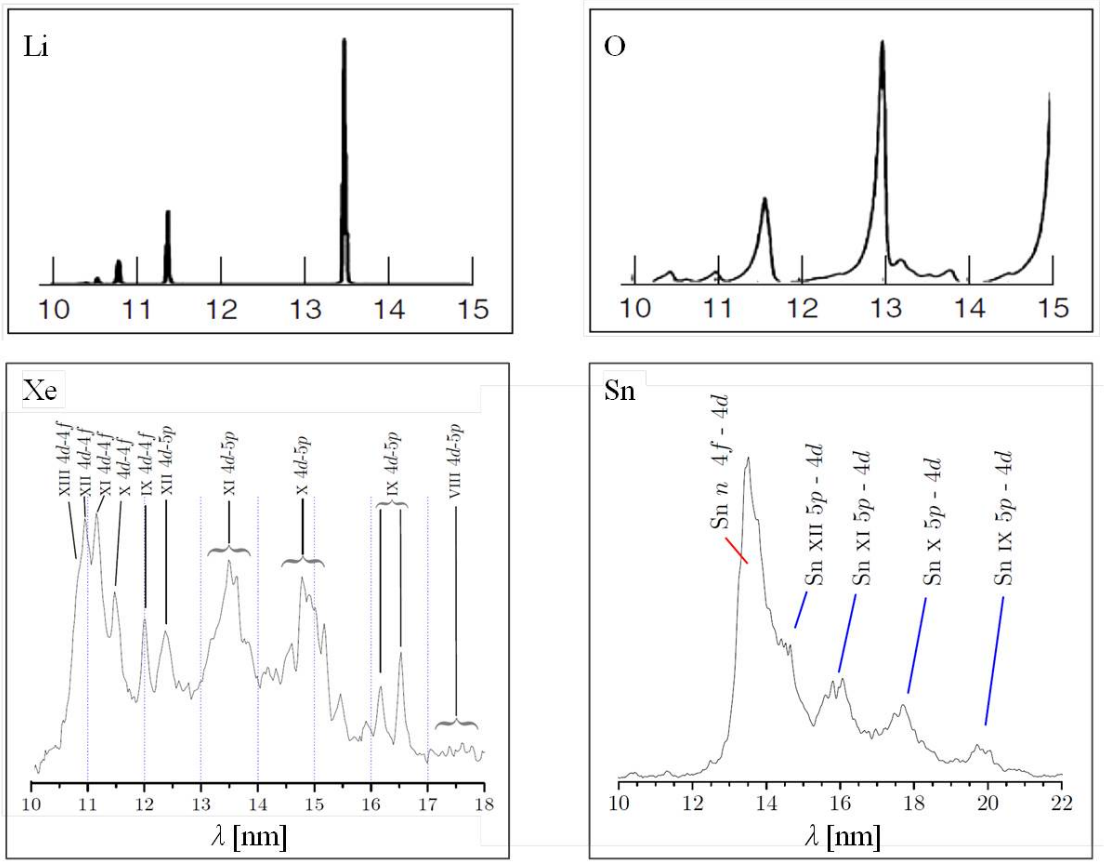

FIGURE 1.5: Spectra of Li, O, Xe, and Sn in the 10-nm range

with 4-5 transitions, 4-4 transitions have higher transition probabilities and locate in a condenser spectral region. Therefore, the intensity of Xe emissions around 11 nm is much higher than that of the in-band 13.5 nm, which significantly lowers the energy CE to ∼1%. For Sn EUV, so far the best CE achieved in tin based 13.5 nm EUV sources is about 5-6% [65–70]. Nevertheless, Xe is still used for laboratory-type installations [71, 72].

1.2.4 Concepts for EUV Source: LPP and DPP

To generate large amount of excited Xe XI ions, impact ionization and excitation by electrons in high density and temperature plasma is the most efficient way. In general, there are two prospective concepts to produce proper plasmas: laser produced plasma (LPP) and discharge produced plasma (DPP).

1.2.4.1 LPP

LPP has a long history to generate powerful x-rays. It is generated by focusing a pulsed laser beam to strike a target material to obtain the in-band EUV emissions. In LPP, laser energy with the power density of 10^{11}∼10^{12} W·cm^{-2} is used to evaporate the target surface[68, 70, 73–75]. The initial ionization of the target occurs through photo-ionization, and the electric field of the laser accelerates these electrons. Nonelastic collisions further ionize the plasma while elastic collision with the ions transfer the electron's kinetic energy into ionic kinetic energy. This process of heating plasma by free-free absorption is called inverse bremsstrahlung absorption (IBA). The absorption coefficient for IBA is given by[76]

$$\alpha_{IB} = \frac{1.08 \times 10^{-5}}{\lambda^2} Z^* (\frac{n_e}{n_c}) \frac{\ln\Lambda}{\sqrt{1 - (n_e/n_c)}} \frac{1}{T_e^{3/2}} \tag{1.3}$$

This equation is written in SI system of units with the absorption coefficient expressed in m^{-1} units, where λ is the wavelength of the incident laser beam in m units, Z^* the average ion charge, T_e the electron temperature in eV units, n_e the electron density, and n_c the critical density at which the electron plasma frequency is equal to the laser light frequency. When $n_e = n_c$, the laser light is reflected from the target.

High temperature electrons and ions collide with each other in dense plasma and create a large amount of excited high charge state ions. The CE of LPP for 13.5 nm EUV generation is determined by the absorption and reflection of the laser energy[69], the spatial match of an optimum electron density and temperature for in-band EUV emissions[77], and the re-absorption of the EUV emission by ions and electrons[78, 79]. All of these aspects are directly decided by the temporal and spatial distributions of electron density and temperature of laser produced plasma, which, together with the spectral purity and the debris generations, were found to be influenced by the geometry and the chemical composition of a target, and the wavelength, power density, spot area, and the pulse duration of a laser irradiation.

In LPP, Q-switched Nd:YAG laser is often used. Mass-limited target material, such as Sn droplet, is also used because the debris generation can be suppressed by fully vaporizing the target. Besides, instead of pure material, compound material is used to reduce re-absorption in the plasmas, and to increase CE. Traditional Nd:YAG lasers are replaced by CO_2 lasers with a wavelength of 10.6 μm to further increase CE. Moreover, a pre-pulse laser is adopted to produce an initial plasma on a target surface with lower electron density and low density gradient, the energy of the main laser pulse can be better absorbed, thus higher CEs are achieved[76]. LPP owns certain advantages: stabilized energy balance in producing plasma, higher reproducibility, smaller source size, less debris, and capable of achieving high repetition rate. However, since the power of the EUV emission is decided by the power of laser irradiation, LPP demands powerful lasers, which are very expensive and need careful maintenance. Besides, the energy CE of laser itself should be taken into account.

1.2.4.2 DPP

DPP is another efficient concept to create EUV source[80–84]. In DPP, hot plasma is created through magnetic compression of low temperature plasma, called the “pinch effect”. Plasma is compressed by the magnetic field generated by the current used to heat the plasma. There are two typical geometries for generating DPP, i.e., Z-pinch and θ-pinch. Because plasma is compressed by magnetic field B from current I, which generates the plasma, the plasma is self-heating. Two forces are present, the magnetic field pressure $B^2/2\mu_0$ and the plasma pressure. Here μ_0 is the vacuum permeability, which is 1 in Gaussian units (cgs). When these two forces are equal, the plasma achieve equilibrium state, and the pinch stops. Then we have the Bennett relation[85]:

$$(Z^* + 1)N_i k_B T_e = \frac{\mu_0 I^2}{4\pi} \tag{1.4}$$

where $N = \pi r^2 n_i$ is the line density of plasma column and k_B the Boltzmann constant.

For a typical industrial EUV source, the stored energy is in the range of 2 to 20 J, with a maximum current from 10 to 30 kA and a first current half circle lasting from about 100 ns to 500 μs[76]. The main concern in DPP is related to power scaling, because a large amount of heat must be dissipated close to the electrode surfaces and in the source system. As an example, to generate 200 W of 2% bandwidth EUV radiation with 2% CE, and 10% collection efficiency, 100 kW of power is needed in a very small volume on the order of 1 cm^3. Besides, DPP produces larger amount of debris due to the erosion and sputtering of electrode. The reproducibility of DPP is also not quite good. However, DPP has an important advantage – it directly converts electric energy to photon energy. Besides, the discharge setup is relatively cheaper than LPP and maintenance of DPP is easier. These advantages lower the cost of ownership, thus DPP sources have gained great commercial interests. There are several different electrode configurations for DPP EUV source using Sn or Xe gas: hollow cathode triggered discharge, capillary discharge, dense plasma focus, star pinch, and laser-assisted discharge plasma (LDP). All these schemes are based on the above mentioned current induced magnetic confinement. Their configurations and working processes are extensively reviewed in Ref. [86]. In this thesis, we focus on the DPP concept.

1.3 Physics of Z-pinch Plasma

Self-constricted plasma configurations are among the most fascinating objects in plasma physics, both because of their natural occurrence in a number of situations, including geophysics (lightning) and astrophysics (current channels at galactic scales), and because of their importance for a variety of applications. The first systematic attempts to analyze these configurations began in 1934, with the publication of a paper by W. H. Bennett on the equilibrium of streams of charged particles with a finite temperature[85]. L. Tonks in 1937 introduced the term “pinch” to describe these configurations. Later, in the 1950s, the prefix “Z” was added to distinguish self-constriction by the axial (z) current from compression of a plasma column by an inductively driven azimuthal (θ) current. Only the former configuration, the Z-pinch, will be considered in this thesis. The various types of Z-pinches can be categorized as several groups[87]: the dynamic pinch, where the kinetic energy of the implosion dominates most other heating mechanisms at stagnation; the equilibrium pinch, where ohmic and compressional heating are most important; the dense plasma focus, a μs-implosion where the sheath is initiated by surface flashover and mass accretion and axial shear are important; and vacuum arcs, where kinetic effect and beams dominate. A broad attack on the study of Z-pinches began in the early 1950s in conjunction with research on controlled thermonuclear fusion[88]. The early work using Z-pinches for producing soft x-ray sources was summarized in Ref.[89].

The DPP concept also belongs to Z-pinches. In a DPP source, a pulsed current is applied on electrodes for discharge. The gas is usually pre-ionized to enhance the initial uniformity, which can help improve the stability of Z-pinch[90]. Due to the skin effect, the pulsed current concentrates in the conducting sheath close to the plasma-vacuum interface. This plasma is then accerated and accelerated toward the axis by the pressure of the azimuthal magnetic field, which is induced by the pulsed current, as shown in Fig. 1.6. During the implosion phase, the high temperature of the compressed plasma ahead of the piston produce a high pressure region, which leads to the formation of a shock wave. In this section we discuss the case of an “ideal” implosion that occurs in the absence of instabilities.

1.3.1 Thin-shell Model

The gross dynamic properties of the pinch implosion, such as the implosion time of the Z-pinch, can be computed reasonably in a zero-dimensional approximation. The simplest model is thin-shell model, which assumes that the imploding plasma is infinitely

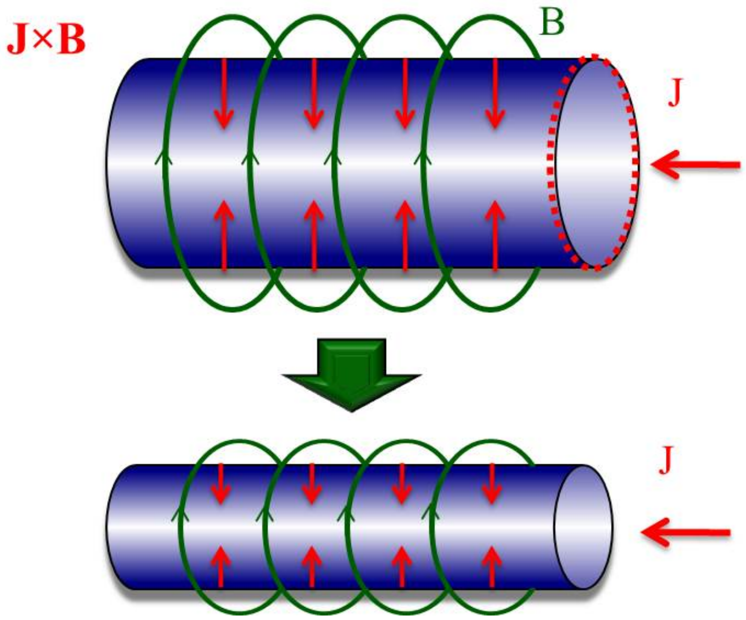

FIGURE 1.6: Illustration of Z-pinch dynamics

thin. The radial position of the plasma shell as a function of time should be consistent with the acceleration by the **J** × **B** Lorentz force, and a constant mass per unit length. The equation of motion of the shell reads

$$\frac{m}{2\pi r}\frac{d^2r}{dt^2} = -\frac{\mu_0 I^2}{8\pi^2 r^2} \tag{1.5}$$

where m is the mass per unit length and μ_0 the vacuum permeability. By introducing dimensionless variables $\widetilde{r} = r/r_0$, $\widetilde{t} = t/\tau$, and $\widetilde{I} = I/I_{max}$, where I_{max} is the maximum current, r_0 the initial radius, and τ the time within which the current reaches its maximum. Eq. (1.5) can be rewritten as

$$\widetilde{r}\frac{d^2\widetilde{r}}{dt^2} = -\Pi\widetilde{I}^2 \tag{1.6}$$

where

$$\Pi = \frac{\mu I_{max}^2 \tau^2}{4\pi\mu r^2} \tag{1.7}$$

is a dimensionless scaling parameter of the problem. To provide good efficiency for converting the energy stored in the pulsed-power generator into kinetic energy of the imploding pinch, one should choose an optimum mass of the pinch material. This mass should be such that the implosion time is approximately equal to the time within which the current reaches its maximum value: if the mass is too large, the current pulse ends before the pinching occurs, and if the mass is too small, the pinching occurs before the current reaches its maximum, also implying poor efficiency. In other words, for every current pulse shape there exists an optimum value of the parameter Π.

1.3.2 Snowplow Model

The snowplow model is another commonly used model to predict the implosion. In this model, an ideal conducting cylindrical shell is assumed to remain infinitely thin and cylindrical symmetric in the process of implosion. This model suggests that all the mass is swept up by the shell as if the magnetic pressure were a snowplow. The snowplow model, first reported in the 1950s, is a widely used picture of the formation of pinch in an initially cold, non-conducting gas or plasma column. The idea was that the nonconducting gas was ionized as it was snowplowed into the sheath.

Consider a cylindrical plasma volume, which is collapsing toward the axis under the pressure of an azimuthal magnetic field, B_θ, produced by a pinch current, I, carried by the imploding Z-pinch shell along the z axis. The plasma is imploding toward the axis into the inner space filled by unperturbed resting plasma. The sharp increase in the pinch current drives the implosion of the current sheath with a shock wave propagating ahead of the current sheath at the beginning of the implosion. Here we consider the snowplow model that takes into account only the increase in the mass of the collapsing shell. The equation of motion reads

$$\frac{m^*}{2\pi r}\frac{d^2r}{dt^2} - \rho(r)\frac{dr}{dt} = -\frac{\mu_0 I^2}{8\pi^2 r^2} \tag{1.8}$$

where

$$m^* = -2\pi r \frac{dr}{dt} \rho(r) \tag{1.9}$$

is the instantaneous mass accreted at the piston. The second term on the left-hand side of Eq. (1.8) describes the momentum imparted to the piston by the accreted material.

The snowplow model predicts pinch time and its dependence on plasma parameters well. However, this model is not adequate to describe the behavior of plasma after pinch. Later, T. Miyamoto derived the snowplow energy equation from the energy equation of the fluid equation[91]. This revised model takes into account kinetic energy, internal energy and magnetic energy in the plasma. Using the snowplow energy equation, the reflection of the shock front can be described.

1.3.3 Fluid Model

It is essential to understand the transport processes in plasma, such as particle diffusion and heat conduction across the magnetic field, electric resistivity, viscosity, and energy transfer to address the critical issues in Z-pinch research. These processes may be described either in terms of binary collisions between particles or collective effects involving the scattering of particles by plasma waves. In general, the state of a fully ionized plasma of electrons and ions can be specified in terms of the velocity distribution functions, which satisfy kinetic equations for electrons and ions. In the limit of no collisions this equation is commonly referred to as the Vlasov or the collisionless Boltzmann equation. This description of ions and electrons in terms of distribution function is often more detailed than required. When the plasma is close enough to equilibrium, it is sufficient to describe the plasma in terms of macroscopic variables such as density, mean velocity, pressure, temperature, etc. Under such circumstance, we can use Magneto-Hydrodynamics (MHD) model to describe the plasma. The validity of the fluid approximation is ensured by the condition[92]

$$K_n = \frac{\zeta}{L_c} \ll 1 \tag{1.10}$$

where K_n is the Knudsen number, $\zeta = \sqrt{(m_i/m_e)}v_{thi}\tau_i$ is the mean free path corresponding to electron-ion energy relaxation,

$$v_{thi} = 9.79 \times 10^5\ \mu^{-1/2}T_i^{1/2}\ \text{[cm/s]}$$

is the ion thermal velocity, μ the ion mass expressed in units of the proton mass.

$$\tau_i = 2.08 \times 10^7\ \frac{\mu^{1/2}T_i^{3/2}}{(Z^*)^4 n_i \ln\Lambda}\ \text{[s]}$$

is the ion collisional time, T_i the ion temperature expressed in eV, and L_c the characteristic length scale. By assuming that the initial ion temperature is 1 eV, ion number density is 10^{17} cm^{-3}, initial average charge state is 1, and initial plasma radius is 1 cm, we have $K_n \sim 10^{-2}$. For pinch stagnation, by assuming that the ion temperature is 30 eV, the ion density is on the order of 10^{19} cm^{-3}, average charge state is 10, and pinch radius is 0.1 mm, we have $K_n \sim 10^{-3}$. Therefore, Eq. (1.10) is satisfied and the fluid model for plasma is valid in our study. The detailed derivation of the MHD equations will be reported in Chapter 4.

1.3.4 Properties of EUV-emitting Plasmas

In a Z-pinch, the energy transfer processes are rather complicated. They include, for example, adiabatic heating, ionization, recombination, excitation, de-excitation, etc. The 13.5 nm in-band EUV emission is generated from the $4d - 5p$ transition of Xe X. For a certain ion, the emissivity η_ν and opacity κ_ν of an electric dipole transition at the frequency ν can be written as

$$\eta_\nu = \frac{h\nu_{ij}}{4\pi} n_i A_{i,j} L(\nu), \tag{1.11}$$

and

$$\kappa_\nu = \frac{h\nu_{ij}}{4\pi} n_j B_{i,j} L(\nu), \tag{1.12}$$

where, i and j are the upper and lower energy levels, $h = 6.626 \times 10^{-27}$ [erg s] the Planck constant, n_i the density of ions in the energy level i, A and B are Einstein coefficients, and $L(v)$ the spectral profile function. The population distribution equation reads[93]

$$\frac{dn_i}{dt} = n_e \sum_{j \neq i} n_j Q_{ji}(T_e) + \sum_{j>i} n_j \Psi_{ji} - n_i[n_e \sum_{j \neq i} Q_{ij}(T_e) + \sum_{j<i} \Psi_{ij}], \tag{1.13}$$

where $Q(T_e)$ represents the rate coefficient for electron impact excitation or deexcitation, and Ψ the radiative decay rate. The atomic data needed can be calculated with the Hebrew University-Lawrence Livermore atomic code (HULLAC)[94]. For simplicity, Local Thermodynamic Equilibrium (LTE) are assumed, thus the population follows Boltzmann distribution.

Considering the configuration of the plasma source, the integrated spectral radiance (ISR in W/cm^2/sr) of a certain transition emerging in the normal direction from a slab medium reads[93]

$$ISR_\lambda^z = \frac{2hc^2}{\lambda_{ij}^4} (\frac{g_i n_i^z}{g_j n_j^z} - 1)^{-1} (\frac{W_\lambda}{\lambda_{ij}}), \tag{1.14}$$

where g is the statistical weight and W is the equivalent line-width. Finally, assuming that the plasma is a column with finite length, and intrinsic homogeneous, the CE in 4π solid angle reads[93]

$$CE = \frac{\sum\limits_{z}\sum\limits_{\lambda 2\%} \pi I S R_{\lambda}^{z} S_p \Delta\tau}{E n_i V_p + \sum\limits_{z}\sum\limits_{\lambda 2\%} \pi I S R_{\lambda}^{z} S_p \Delta\tau} \tag{1.15}$$

For the in-band EUV emission, $\lambda = 13.5$ nm, S_p and V_p are plasma surface and volume, respectively, $\Delta\tau$ is the emission duration. Since emissions with continuous spectra are negligible in the EUV region, E is defined as the minimum energy needed to heat and ionized a plasma to a given ionization state:

$$E = \sum_{1}^{\overline{Z}} E_z + \frac{3}{2}T_i + \frac{3}{2}\overline{Z}T_e + E_c, \tag{1.16}$$

where E_z is the ionization potential, T_i the ion temperature, T_e the electron temperature, E_c the cohesive energy. If we assume $T_i = T_e$ at the maximum implosion, CE will only depend on the electron temperature and density, which means that the electron density and temperature of the Z pinch plasma are the major factors towards EUV emission. The optimum electron temperature and density for 13.5 nm EUV emission from Xe plasmas, given in Refs. [95, 96], are $25 \sim 30$ eV and $10^{18} \sim 10^{19}$ cm^{-3}, respectively.

1.3.5 Instabilities in Z-pinches

The instability of a heavy fluid layer supported by a light one is generally known as Rayleigh-Taylor (RT) instability. In a Z-pinch, the Magneto-Rayleigh-Taylor (MRT) instability plays an important role. This instability is universal and very difficult to stabilize. It is a key factor in limiting the performance of fast Z pinches and other pulsed-power devices. There are two important specific features in the stabilities analysis of dynamic Z-pinches. First, the unperturbed state is itself time dependent, so that the time dependence of the perturbation cannot be taken in the form exp(γt), and it is not obvious which parameters should be used to characterize the growth instead of the conventional experiential growth rate. Second, the MRT instability now comes into play. Indeed,

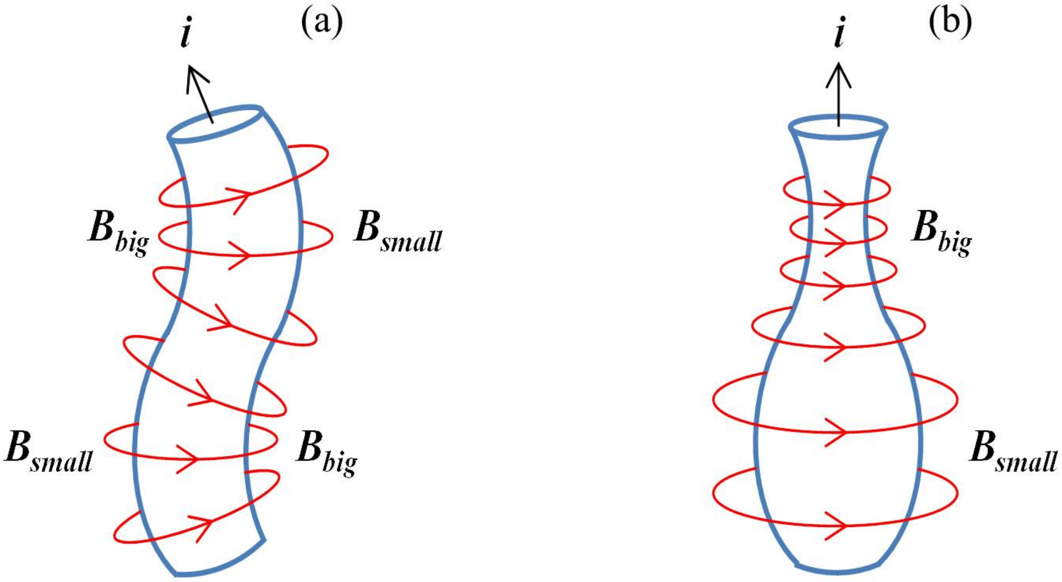

FIGURE 1.7: Physical mechanism of the (a) m=1 kink instability and (b) m=0 sausage instability modes in Z-pinch.

plasma is imploded by the pressure due to the azimuthal magnetic field in Z-pinch. Thus, the plasma, in its own frame of reference, represents a “heavy fluid”, which is supported by a “massless fluid”(i.e., by the magnetic field) in the gravitational field $\mathbf{g} = -\mathbf{a}$, where $\mathbf{a}$ is its acceleration, and this configuration inevitably exhibits the MRT instability. In cylindrical geometry, the perturbation displacement vector is expressed by

$$\boldsymbol{\xi}(r,t) = \xi(r)\text{exp}(\gamma t + im\theta + jkz) \tag{1.17}$$

where m and k are azimuthal and axial wave numbers. $Re(\gamma)$ is the growth rate of the MRT instability. The physical mechanism of the $m = 1$ kink instability and $m = 0$ sausage instability modes in Z-pinch are shown in Fig. 1.7[97, 98]. The $m = 1$ kink perturbation forces the magnetic lines to concentrate on the concave side of the column, and the increased magnetic field acts as a destablizing force. The $m = 0$ sausage perturbation increases the magnetic field in the neck, because the same current flows in a smaller core section and the increased magnetic pressure tends to deepen the neck further.

1.4 Scope and Outline of the Thesis

The EUV source is one of the most critical issues for commercialization of EUVL. The Z-pinch dynamics is vital in determining the CE of DPP EUV source. An insight into the Z-pinch physics is necessary to further optimize the light source. Because of the intrinsic complexity of the Z-pinch, both experimental and numerical methods are necessary to grasp the essence of the problem. Therefore, the goal of the work, reported here, is to learn the Z-pinch dynamics of the DPP EUV source both experimentally and numerically and try to optimize the EUV source. The scope of this research is limited to the 13.5 nm Xe gas jet type DPP EUV source and the simulation is restricted to initial uniform plasma. However, the diagnostic techniques and numerical method adopted in this research are also applicable to some other related researches.

In Chapter 1, the history of EUVL is reviewed. Then we introduce the EUV source, including the requirements from industry, the selection of the wavelength, source material, and two prospective concepts (DPP and LPP). The basic models of Z-pinch (thin-shell model and snowplow model), CE calculation in LTE approximation, and basic concept of MRT instabilities are also presented in this chapter.

In Chapter 2, the Xe DPP EUV source setup and diagnostic techniques are introduced. The RF pre-ionization system, the structure of the electrode, and the pulsed power circuit are discussed in detail. The diagnostic techniques adopted includes time-resolved EUV intensity measurement system and visible region plasma imaging system, time-integrated EUV pinhole imaging, Nomarski interferometer for electron density measurement, and Faraday cup (FC) for particle kinetics measurement.

In Chapter 3, the experimental results of the diagnostics are reported. The relationship between EUV emission and experimental conditions are studied. Time-resolved visible region imaging and time-integrated EUV imaging are presented. In addition, the electron density evolution in Z-pinch and the particle kinetics in decay phase are also scrutinized.

In Chapter 4, the MHD model in cylindrical coordinate system based on single-fluid two-temperature approximation are derived. The Total Variation Diminishing (TVD) algorithm for the hyperbolic system and the sparse band matrix scheme for the diffusion terms are introduced.

In Chapter 5, the simulation results of the plasma behavior are present. The evolution of the plasma and the influences of initial conditions on pinch dynamics are studied. The Magneto-Rayleigh-Taylor (MRT) instabilities in Z-pinch are studied in detail. The mitigation methods for MRT instability are also present.

Finally, we conclude our study in Chapter 6 and propose possible ways to optimize the EUV source.

Chapter 2

Xe Gas Jet Type DPP EUV Source and Diagnostic Techniques

This chapter focuses on the experimental setup and diagnostic techniques. In the first part of this Chapter, the DPP EUV source experimental setup is introduced in detail. The main part of this setup contains a pulsed power circuit, a double nozzle gas jet type electrode, and an RF pre-ionization system. In the second part of this chapter, the diagnostic techniques used in this research are present, including EUV photodiode EUV emission detection, visible region plasma imaging, EUV pinhole imaging, Nomarski interferometry, and Faraday cup. These diagnostic tools are important to understand EUV emission characteristics and plasma dynamics. In this chapter, the experimental setup of the Xe gas jet type EUV source and the diagnostic techniques are introduced. The main components of the DPP EUV device are a pulsed power supply, an RF pre-ionization system, and a double nozzle gas jet type electrode. An EUV emission detection system was assembled to gauge the EUV signal waveform. A high speed camera was adopted to record the visible region plasma image. Then a pinhole imaging system was assembled to record the EUV pinhole image. The electron density evolution was measured by a Nomarski interferometer. Finally, Faraday Cup (FC) was used to diagnose the particle kinetics.

2.1 Experimental Setup of the Xe DPP Source

The schematic of gas jet type DPP EUV source setup is shown in Fig. 2.1. The Xe gas is supplied through quartz glass tube to the chamber. The gas flow rate was adjusted by the flow control valve 248A-00010-R manufactured by MKS INSTRUMENTS. The detailed specifications of the gas flow control is given in Table. 2.1. The maximum inlet pressure is 1034.3 kPa. The minimum controllable flow rate is 0.2% of F.S. when the flow rate is smaller than 100 sccm and 0.1% of F.S. when the flow rate is larger than 100 sccm. The pressure controllable range is between 1.33×10^{-2} and 666.6 kPa. The working temperature of the gas flow controller is between -10 and 60 °C. The quartz glass tube is 30 mm in outer diameter and 500 mm in length. The particle number density for main discharge is controlled by the amount of gas supplied into the chamber. The pressure value is read from the Baratton absolute pressure transducer 622A01TDA manufactured by MKS INSTRUMENTS, whose detailed specifications is given in Table. 2.2. The entire system can provide a maximum pressure of 43 Torr. The Xe gas is first pre-ionized by the RF with a working frequency of 13.56 MHz and maximum RF power of 100 W.

TABLE 2.1: Specifications of the gas flow control

Specifications	Values
External leakage	$< 10^{-9}$ sccm/sec
Max. input pressure	1034.3 kPa
Max. full-scale	10 slm
Min. controllable flow rate	0.2 % F.S. (< 100 sccm) 0.1 % F.S. (>100 sccm)
Pressure controllable range	$1.33\times10^{-2}\sim$ 666.6 kPa
Response time	15 m·sec
Temperature range	-10∼60°C

The vacuum chamber and observation windows are shown in Fig. 2.2. Two pairs of vacuum system consisting of a Turbo Molecular Pump (TMP) and a rotary pump are installed separately in order to provide a high vacuum environment in the chamber. Such system is possible to maintain the chamber pressure on the order of 10^{-5} Torr in

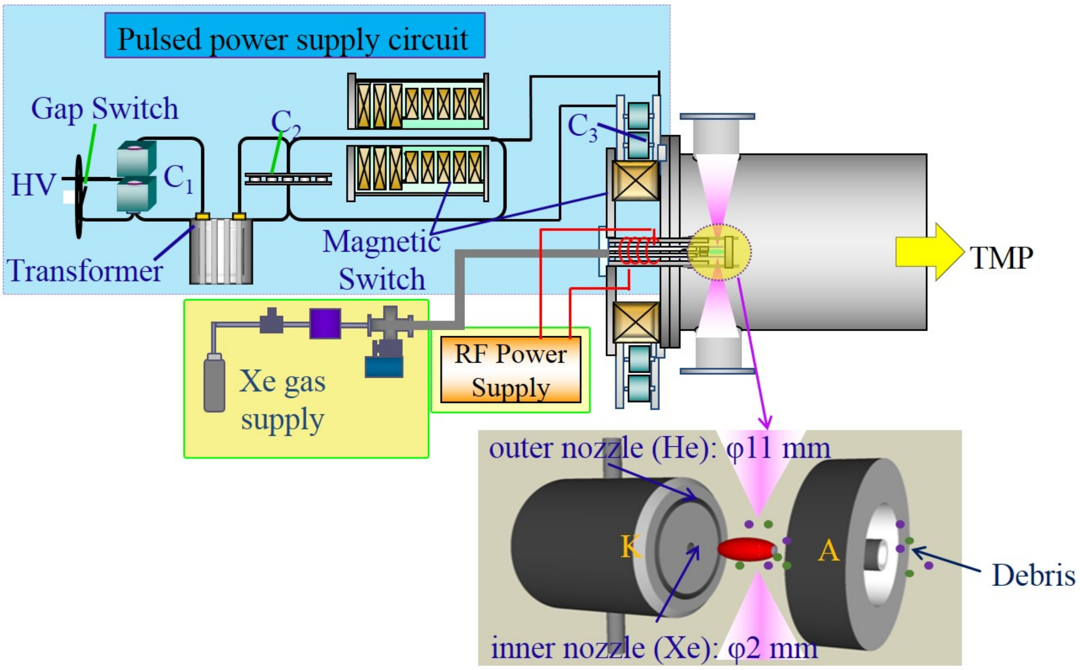

FIGURE 2.1: Schematic of the Xe gas jet type DPP EUV source.

absence of gas supply. In addition, it provides several observation ports to enable us to install the diagnostic devices inside or outside the vacuum chamber so that various measurements from different angles can be performed.

2.1.1 RF Pre-ionization System

The schematic of the RF pre-ionization system is shown in Fig. 2.3. The Xe gas is pre-ionized in the quartz glass tube by using the RF that is about 20 cm away from the main discharge electrode. The RF power supply (T161-5066A, manufactured by Thamway) can provide a maximum RF power of 100 W at working frequency of 13.56 MHz. The

TABLE 2.2: Specifications of the Baraton absolute pressure transducer

Specifications	Values
Full-scale range	133.32 kPa
Effective measurement range	1×10^{-4} F.S.
Operating temperature range	0∼50°C
Max. overpressure	310.3 kPa
Time constant	$<$ 20 m·sec

FIGURE 2.2: External view of the vacuum chamber.

load coil is a 4-turn coil made of copper wire of 3 mm in diameter. The distance from the electrode to the load coil can be arranged from 10 to 50 cm. By providing a 13.56 MHz RF current via the matching box to the load coil, induced magnetic field is generated in the quartz glass tube. Then Xe gas is excited and ionized, forming an RF plasma. The plasma is then sent into the vacuum chamber for discharge.

2.1.2 Electrode Structure

The coaxial double nozzle type electrodes are adopted in the DPP EUV setup, as shown in Fig. 2.1. The inner nozzle is 2 mm in diameter, and the outer nozzle is 11 mm in diameter. Xe gas is supplied through the inner nozzle to form a gas jet and He gas, if used, is supplied via the outer nozzle to form a gas curtain. Due to the constraints on the electrode shape, conventional DPP sources usually emit EUV radiation in the axial

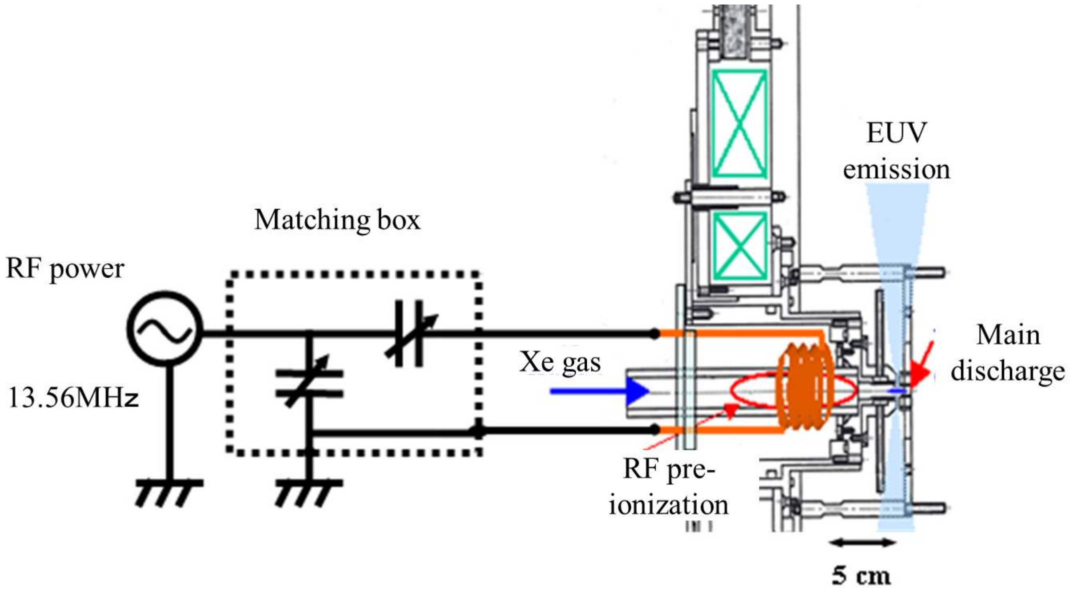

FIGURE 2.3: Schematic of the RF pre-ionization system.

direction, thus collection angle is relatively small. However, the electrode designs employed here can provide a 1.8 π sr collection angle by collecting in the radial direction. Another advantage of such electrode structure is that there is no capillary, so that less debris is produced during discharge. In addition, the debris is mainly ejected in the axial direction while we collect EUV emission in the radial direction, thus such structure enable us to collect less debris.

2.1.3 Pulsed Power Circuit

The pulsed power supply consists of a gap switch, a 2.7 kV high voltage power supply, an LC inversion circuit, a 1:3 step-up transformer, and a two-stage magnetic pulse compressor, as shown in Fig. 2.4.

The pulsed power circuit can provide a current pulse with a peak value of about 20 kA and a rise time of about 110 ns. A typical pulsed current waveform and its corresponding voltage waveforms on capacitors C_2 and C_3 with RF power of 20 W and gas inlet pressure of 24 Torr are shown in Fig. 2.5.

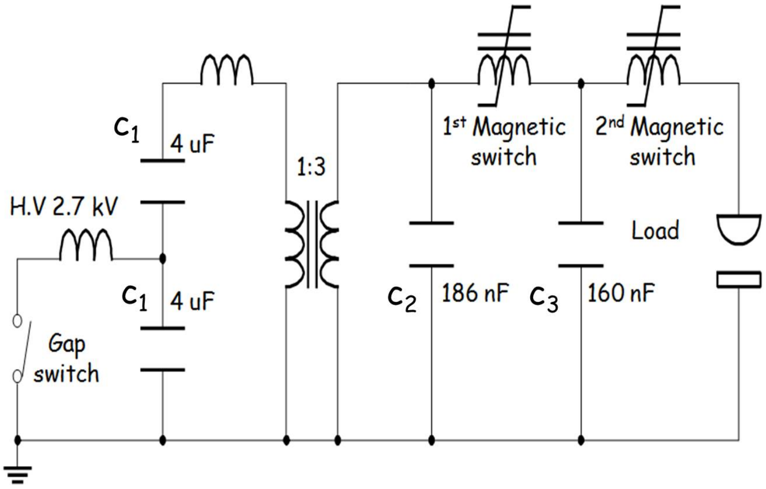

FIGURE 2.4: Schematic of the pulsed power supply circuit.

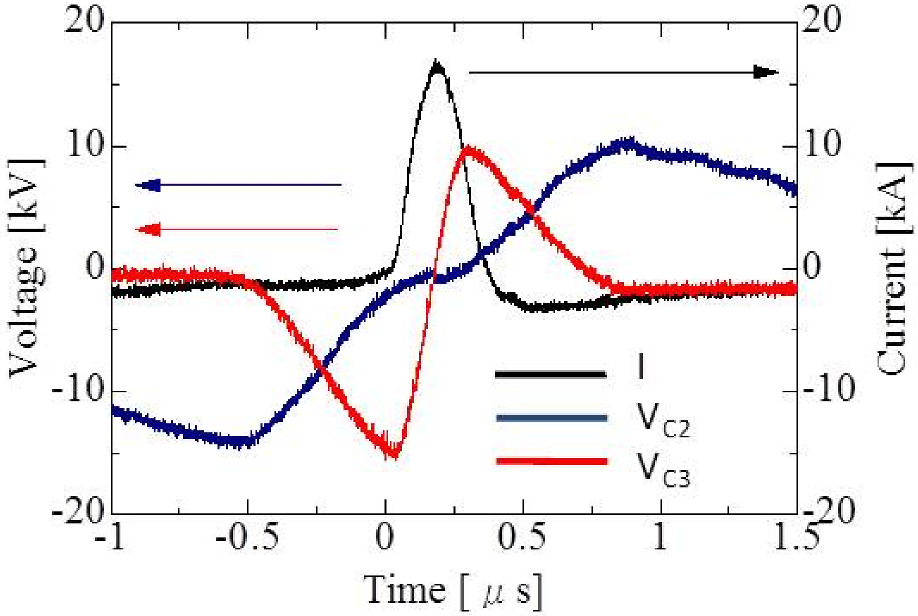

FIGURE 2.5: Pulsed current waveform and its corresponding voltage waveforms on capacitors C_2 and C_3 with RF power of 20 W and gas input pressure of 24 Torr

TABLE 2.3: Specifications of the capacitor

Capacity	Rated voltage	Max. current	Inductance	Size
2 μF	5 kV	25 kA	20 nH	$59 \times 150 \times 77$

TABLE 2.4: Specifications of the high voltage supply 802L

Max. voltage [kV]:	15
Charing rate [kJ/sec]:	8000
CE:	85%

2.1.3.1 LC Inversion Circuit

In the setup, the LC inversion circuit is used as high voltage generator to double the initial 2.7 kV high voltage. First of all, the lower capacitor voltage of C_1 is charged to $V_0 = 2.7$ kV. Then the capacitor is discharged through the inductor by turning on the switch gap, and the polarity of the voltage is inverted. Therefore when $t = \pi\sqrt{LC}$, the output voltage of the LC inversion becomes -2V_0. The specifications of the capacitors used in the LC inversion circuit are shown in Table. 2.3. The capacity is 2 μF and maximum current is 25 kA. The high voltage power supply (802L) for charging the capacitor is manufactured by LAMBDA EMI, whose specifications are shown in Table. 2.4. It can provide a maximum voltage of 15 kV.

2.1.3.2 Main Switch

The pulsed power supply requires such a main switch that can withstand a high voltage when cut off. On the other hand, it has a short switching time when it turns on. In addition, it is also necessary to be capable of passing through a large current when conducted. A trigger gap switch is adopted in the pulsed power supply. The schematic of the trigger electrode is shown in Fig. 2.6. It consists of a main electrode and a needle-shaped trigger electrode. By applying a voltage of several kV, discharge is induced between the main electrodes and the trigger electrode; ultraviolet rays and plenty of charged particles are generated simultaneously. As a result, the gap between electrodes

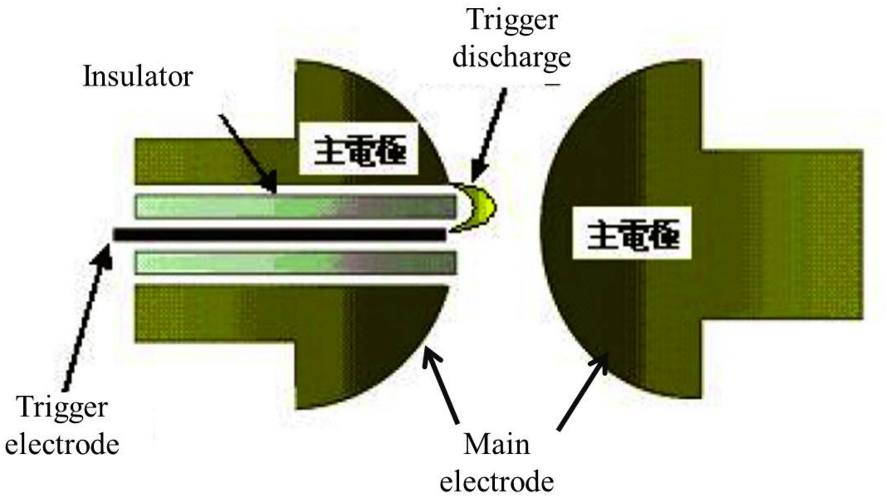

FIGURE 2.6: Schematic of the trigger gap switch

is weakly ionized. Electric field near the trigger electrode is strained due to the space charge distribution. Therefore main electrode gap is broken down and spark discharge is formed.

2.1.3.3 Pulse Transformer

The pulse transformer is manufactured by Nihon Denji Co., Ltd. The nanocrystalline soft magnetic material FINEMET FT-3M manufactured by Hitachi Metals Co., Ltd. is used for the core. The turn ratio of the secondary winding and the primary one is 1:3. Its purpose is to not only boost the voltage but also to protect the switch and power supply by electrically insulated the primary side of this pulse transformer from the main discharge portion.

2.1.3.4 Two Stage Magnetic Pulse Compressor

In order to obtain a discharge current with short rise time for producing the EUV radiation, a two-stage magnetic pulse compressor (MPC) is used in the pulsed power circuits. The magnetic compression circuit can provide a pulsed current with a Full Width at Half Maximum (FWHM) of $\sim$210 ns and a rise time of $\sim$110 ns.

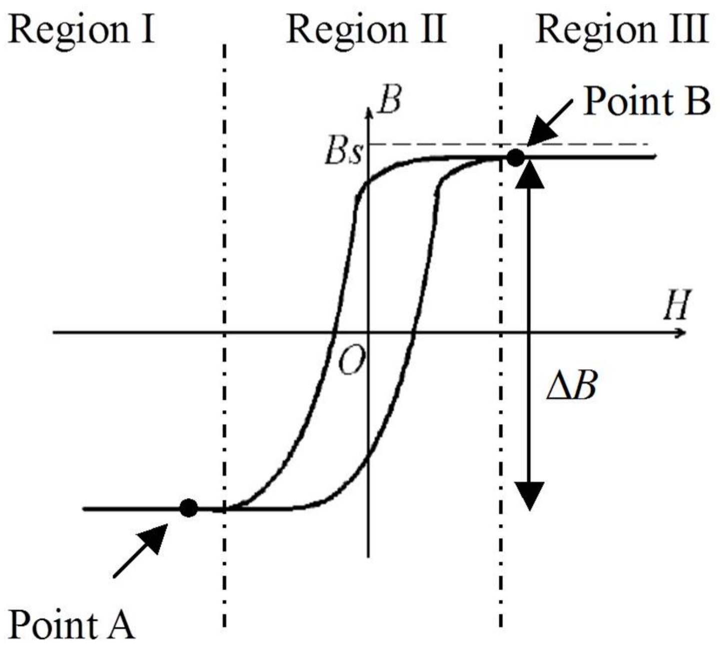

FIGURE 2.7: B-H curve of a typical magnetic core used in a magnetic switch.

The magnetic pulse compression circuit consists of a start switch and a magnetic switch. The magnetic switch typically consists of a winding which surrounds a core of magnetic material having a B-H curve as shown in Fig. 2.7. Initially, the magnetic switch is biased (or reset) at the negative saturation flux (point A). When a voltage is applied across the magnetic switch, the magnetic domains within the core of the switch reorient such that the bias point of the core moves into region II of the B-H curve. While in this region, the slope of the B-H curve is very steep and the magnetic switch can support a significant voltage by virtue of Faraday's law. Therefore, little current flows through the windings of the magnetic switch and the device is seen to have a large impedance. As voltage continues to be applied across the magnetic switch, the working point of the core moves further up the B-H curve until the positive saturation flux is reached. When the magnetic core saturates, the rate of change of the flux, which is necessary to support a substantial voltage, cannot be sustained any more. As a result, the voltage across the magnetic switch is significantly reduced and current is forced to flow through the winding.

In general, the magnetic core material of the magnetic switch should satisfy several requirements listed below:

TABLE 2.5: Specifications of the FINEMET FT-1H

Specifications	Values
Maximum flux density B_s	1.35 T
Rectangular ratio B_r/B_s	0.9
Coercive force H_c	0.8 A/m
Permeability	5000@1 kHz 1500@100 kHz
Resistivity	1.1 $\mu\Omega$m

a) Large saturation magnetic flux density.

b) Large relative permeability μ_R during the non-saturated region and $\mu_R \approx 1$ during the saturated region.

c) Supplying several μs order of magnetization time.

d) Reset circuit for stable high repetition rate operation.

Table. 2.5 shows the specifications of the magnetic core material (FINEMET FT-1H, Hitachi Metals) used in present circuit. The precursor of FINEMET is amorphous metal obtained by rapid quenching the liquid alloy, consisting of Fe, Si, B, and small amount of Cu and Nb. FINEMET has high saturation magnetic flux density comparable to Fe-based amorphous metal and high permeability comparable to Co-based amorphous metal and low eddy current loss. The maximum magnetic flux density of FINEMET FT-1H is 1.35 T. The rectangular ratio is 0.9, permeability is 5000 at 1 kHz and 1500 at 100 kHz, and the resistivity is 1.1 $\mu\Omega$m.

The MPC is the assembling of a series of magnetic switches. The principle of MPC has been documented in many literatures[99–101]. The MPC is based on a resonant energy transfer circuit as shown in Fig 2.8. Capacitor C_0 is initially charged to V_0. When switch is closed at t =t_0, C_0 is connected to C_1 through magnetic switch MS_0. Therefore the energy stored in C_0 is resonantly transferred to C_1, resulting in a rising voltage on C_1. The magnetic core of MS_1 is initially biased at its negative saturation flux. When the voltage across C_1 begins to increase, the voltage is also impressed across

MS_1 causing the magnetic flux density in the core to increase. MS_1 is designed such that the flux density reaches the positive saturation flux at the moment when the voltage on C_1 reaches its maximum value. When the saturation flux is reached, the relative permeability of the magnetic core decreases significantly, causing the reduction in the value of inductance associated with MS_1. Therefore the energy stored in C_1 now can be transferred to C_2. By assuming that C_0=C_1=C_2, the energy transfer time from C_0 to C_1 is

$$\tau_1 = \pi\sqrt{\frac{L_0C_0}{2}} \tag{2.1}$$

and from C_1 to C_2 is

$$\tau_2 = \pi\sqrt{\frac{L_1C_1}{2}} = \pi\sqrt{\frac{L_1C_0}{2}} \tag{2.2}$$

where $L_{0,1}$ are the saturated inductances of MS_0 and MS_1, respectively.

The peak current passing through C_0 and C_1 are

$$I_{1max} = V_0\sqrt{\frac{C_0}{2L_0}} \tag{2.3}$$

and

$$I_{2max} = V_0\sqrt{\frac{C_0}{2L_1}} \tag{2.4}$$

Therefore we have the pulse compression ratio or the peak current amplification ratio:

$$G = \frac{\tau_2}{\tau_1} = \frac{I_{1max}}{I_{2max}} = \sqrt{\frac{L_0}{L_1}} \tag{2.5}$$

If the saturated inductance of MS_1 is much smaller than that of MS_0, the energy transfer from C_1 to C_2 is much faster than that from C_0 to C_1. By connecting a series of such C-L-C circuits, a peak power gain with faster rise time can be realized.

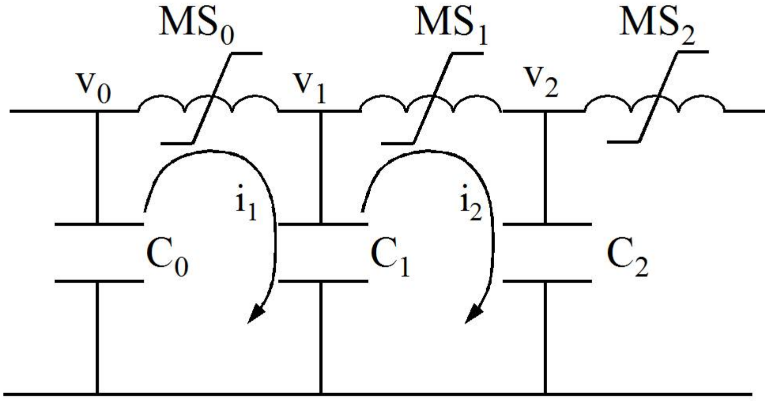

FIGURE 2.8: Equivalent circuit for MPC.

2.2 Diagnostic Techniques for the DPP Source

In order to experimentally investigate the radiation properties and various physical processes in the 13.5 nm DPP EUV source, proper plasma diagnostic techniques are necessary. The most common diagnostic techniques adopted for laboratory plasmas are probe methods and optical methods. Langmuir probe, for example, is extensively used in many cases. It is a convenient way to obtain important plasma parameters, e.g., the electron density, electron temperature, and Electron Energy Distribution Function (EEDF)[102, 103]. However, the probe diagnostics is an intrusive method that may disturb the plasma and change the plasma state. Besides, the geometric size of the probe also limits the spatial resolution of the measurement. In case of the DPP source studied in this thesis, the plasma radius is on the order of several millimeters; therefore the resolution of conventional probe is insufficient to provide an accurate experimental results. In addition, due to the high temperature of the Z-pinch plasma, the probe is easy to be destroyed. The non-intrusive methods, on the other hand, can avoid disturbing the plasma. Optical diagnostics, which is one of the most widely used non-intrusive methods, is characterized as a method of high resolution detection. In this section, the configurations and principles of the diagnostic techniques utilized for studying the DPP EUV source are presented.

The radiation output is the most important aspect of evaluating an EUV radiation source.

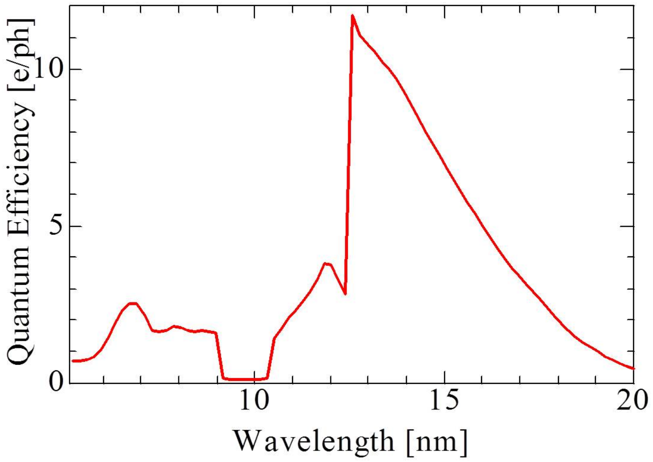

FIGURE 2.9: Quantum efficiency of AXUV series high speed phitodiode.

Here we first present the experimental results of EUV radiation output. Then, the time-resolved visible region plasma imaging and time-integrated EUV pinhole imaging are measured.

2.2.1 Time-resolved EUV Emission Detection

The AXUV-high speed series photodiode (AXUV20HS1 manufactured by IRD. Inc..) and a 40 μm pinhole was mounted in the radial direction to record time-resolved EUV radiation. This photodiode is Si/Zr coated and has a band pass of 11-18 nm; therefore it can eliminates the influences of non-EUV emission. The quantum efficiency of AXUV20HS1 is shown in Fig 2.9. It has a maximum efficiency near the wavelength of 13 nm.

The schematic of the time-resolved measurement system for EUV radiation output is shown in Fig. 2.10. In addition, it also prevents too many photons from being collected and the saturation of photodiode signal. The photodiode signal is recorded by an oscilloscope (LT584L, manuactured by LeCroy). An example of detected EUV signal waveform and its corresponding current waveform with electrode gap length of 6 mm

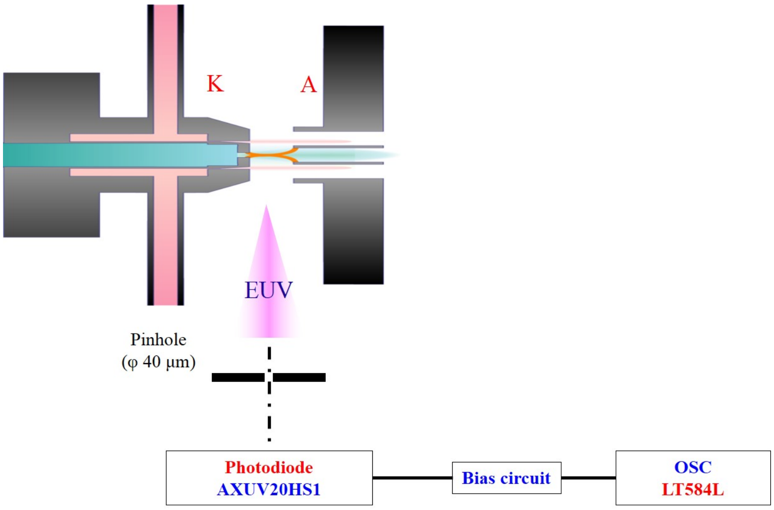

FIGURE 2.10: Schematic of the time-resolved EUV emission measurement system.

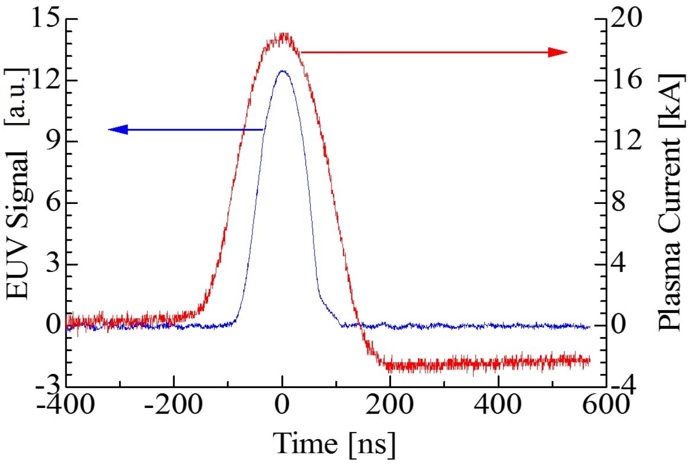

FIGURE 2.11: An example of EUV signal waveform and its corresponding current waveform with electrode gap legnth: 6 mm and Xe gas pressure: 25 Torr.

and Xe inlet gas pressure of 25 Torr is shown in Fig. 2.11. The current is measured with a Rogowski coil. The EUV signal intensity is expressed in arbitrary unit (a.u.) because the absolute calibration of the EUV signal is not available. The FWHM of the EUV signal is ∼100 ns, while that of the current pulse is ∼200 ns.

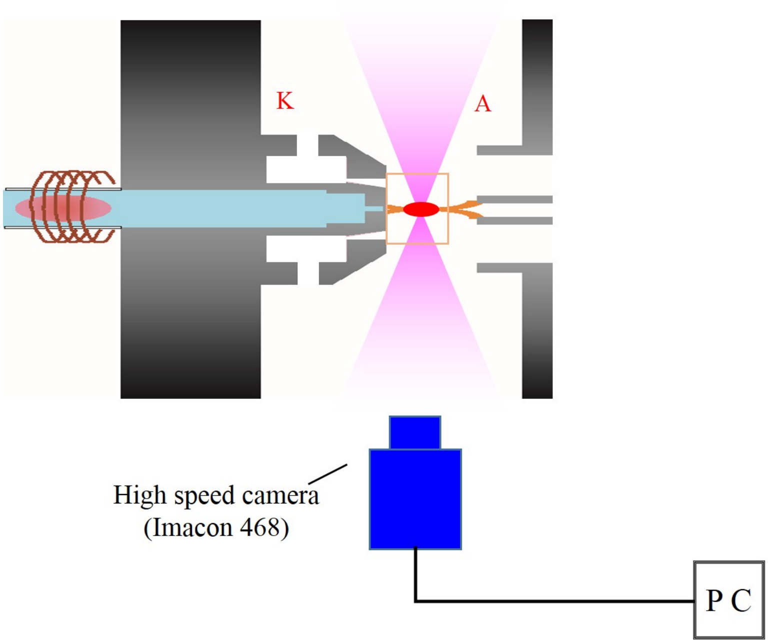

FIGURE 2.12: Schematic of the visible region time-resolved plasma imaging system with high speed camera.

2.2.2 Time-resolved Plasma Imaging

The plasma imaging includes both time-resolved visible region imaging and time-integrated EUV pinhole imaging. A high speed camera (Imacon 468, manufactured by DRS HADLAND) is used to record the visible region plasma radiation in the radial direction. The exposure time is 10 ns; while the typical pinch time is several hundred nanoseconds, therefore such experiment can be considered as time-resolved. The high speed camera is synchronized with the trigger system of the DPP setup so that it can capture the plasma imaging at desired time. The plasma images are stored in a PC. The schematic of the time-resolved plasma imaging system with high speed camera in visible region is shown in Fig. 2.12.

2.2.3 Time-integrated Plasma Imaging

The EUV pinhole camera is a suitable equipment to observe the spatially resolved EUV emission from a plasma source. The pinhole image camera usually consists of an x-ray

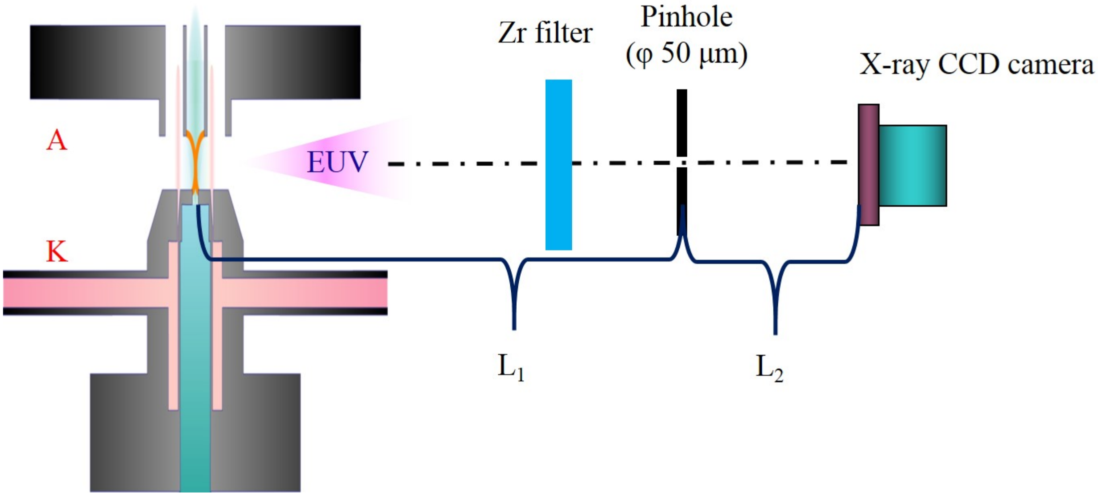

FIGURE 2.13: Schematic of the pinhole camera system.

CCD camera (DO434, manufactured by Andor Technology, 1024 × 1024 pixels, 13 × 13 μm^2, detector size 13.3 × 13.3 mm^2), a pinhole of 50 μm in diameter, and a Zr filter with band pass of 7∼16 nm. The schematic of the pinhole camera is shown in Fig. 2.13. L_1 is the distance from the plasma source to the pinhole, and L_2 the distance from CCD camera to the pinhole. The Zr filter with 150 nm in thickness is put in front of the pinhole. The pinhole image is projected onto the x-ray CCD camera, which has a quantum efficiency of 45% for EUV emission at 13.5 nm.

The resolution of the pinhole camera is determined by diffraction at the pinhole and by the geometry of the setup[104]. The resolution due to diffraction is

$$R_d = 0.61\frac{L_1\lambda}{r} \tag{2.6}$$

where λ is the wavelength, and r the radius of the pinhole. The resolution due to the geometry is

$$R_g = 2\cdot r(\frac{L_1}{L_2}+1) \tag{2.7}$$

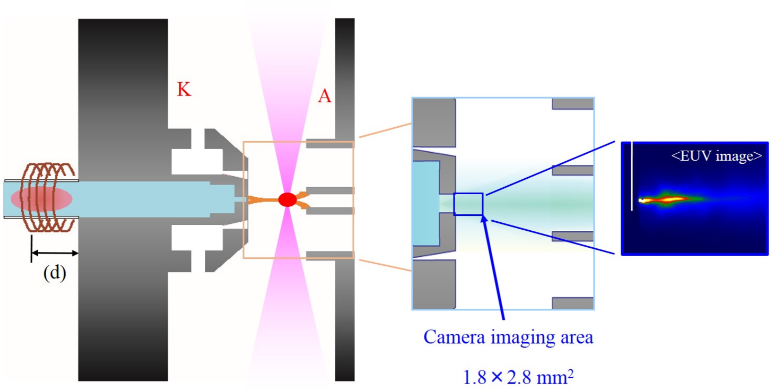

FIGURE 2.14: The observation region of the pinhole imaging system and an example of the time-integrated EUV pinhole image.

The resolution of the pinhole camera system is

$$R_p = \sqrt{R_d^2 + R_g^2} \tag{2.8}$$

In our experiment, we have $L_1 = L_2$ =285 mm; consequently, R_d =47 μm, $R_g = 200$ μm, and thus $R_p = 205$ μm.

The observation region of the pinhole imaging system and an example of the time-integrated EUV pinhole image are shown in Fig. 2.14.

2.2.4 Electron Density Measurement

The electron density is one of the most important parameters of Z-pinch plasmas. There are several diagnostic techniques frequently used for measuring the electron density, including laser interferometry, Stark broadening, Thomson scattering, and Langmuir probe. The Thomson scattering method can determine the electron density and temperature simultaneously. However, due to the low intensity of the scattered signal, it needs spectrometers with quite high sensitivity. The experimental procedures to reduce the noise level is also very complicated and currently not available. In case of Langmuir probe, it is a convenient way to analyze the plasma parameters; however, in our

Z-pinch DPP device, its spatial resolution cannot satisfy our requirements thus limits its application.

The interferometry is a method that can quantitatively measure the variation of the refractive index of a plasma by detecting the phase shift of the light wavefront, from which the absolute electron density distribution can be obtained. In an interferometer, two beams pass through separate paths before they interfere with each other. One passes through the plasma and the other, which serves as the reference beam, passes through vacuum. The phase shift caused by the plasma can be visualized by the fringe shift in the interferograms when the two beams interfere with each other. There are various different configurations of interferometers, but their basic principles are the same . The most commonly used are Michelson interferometer, Mach Zehnder interferometer, Sagnac interferometer, shearing interferometer, Nomarski interferometer, and Moire deflectometer. The principles of these interferometers are summarized in Ref. [105, 106]. Compared with the other interferometers, the main advantages of Nomarski interferometer lie in its relatively simple structure and absence of alignment and stability issues. In this section, the Nomarski interferometer is introduced to study the spatial-resolved electron density evolution in Z-pinch..

The schematic of the Nomarski interferometer adopted to diagnose the gas discharge of the Xe DPP source is shown Fig. 2.15. It consists of a Nd:YAG laser, two polarizers, a Wollaston prism, a high speed camera (Imacon 468), several lenses and several mirrors. The laser wavelength is 532 nm and its pulse duration is 5 ns. The first polarizer linearly polarizes the circularly polarized output beam of the Nd:YAG laser. The Wollaston prism, which is carefully aligned, splits the laser beam into two equal branches with orthogonal planes of vibration. The polarization plane of the second polarizer is set at 45° to the vibration planes of both branches so that after passing through it, the two beams interfere with each other and form a fringe pattern. With no plasma, the Nomarski interferometer forms a straight fringe pattern, which serves as a background;

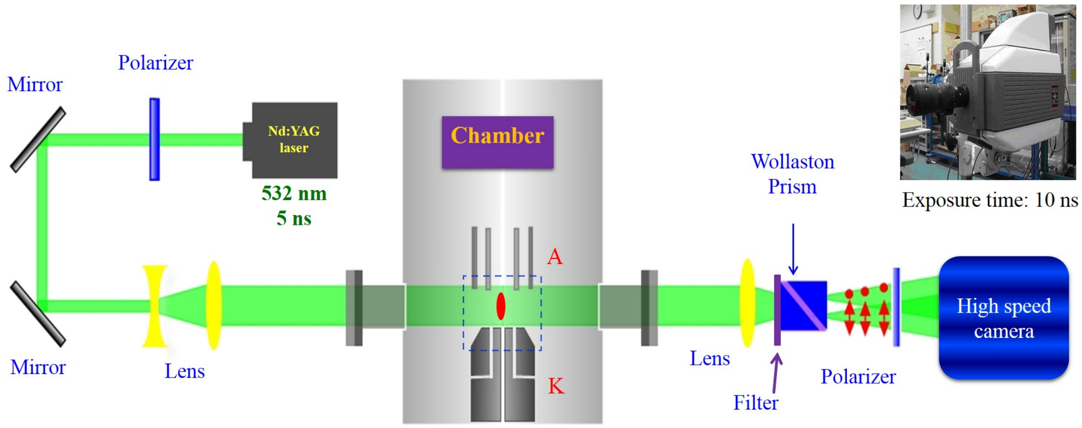

FIGURE 2.15: Schematic of the Nomarski interferometer system.

when the plasma is present, it causes fringe shifts which contain the desired electron density information.

A sample interferogram with the fringe shift caused by the plasma is shown in Fig. 2.16. The phase shift $\Delta\phi$ is the function of the frequency of the probe laser ω, the path length through the plasma l, and the electron number density of the plasma n_e[107, 108]:

$$\Delta\phi = \frac{\omega}{c}\int[1-(1-\frac{n_e}{n_c})^{1/2}]dl, \tag{2.9}$$

where c is the speed of light in vacuum, n_c=2.3$\times$10^{21} cm^{-3} the critical density at the wavelength of 532 nm. If we neglect the reflectivity of the neutral atoms, and assume the electron density n_e is much less than the critical density of the probe laser n_c, the phase shift can be simplified as

$$\Delta\phi \approx \frac{\omega}{2cn_c}\int n_e dl \tag{2.10}$$

Using D to denote the fringe shift number, then $\delta\phi = 2\pi D$. The chord-integrated electron density is given by

$$\int n_e dl = 2Dn_c\lambda \tag{2.11}$$

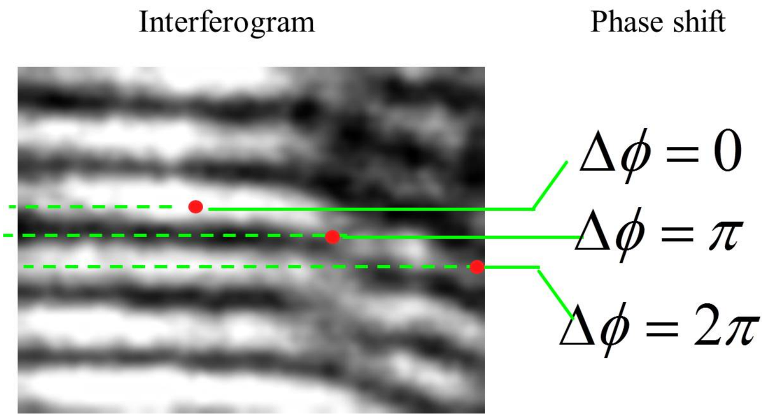

FIGURE 2.16: A sample interferogram with the fringe shift caused by the plasma.

where $\lambda = 532$ nm is the laser wavelength. D can be easily obtained from the fringe patterns. By assuming that the electron density distribution inside the plasma column is axisymmetric, the radial electron density distribution can be obtained by using Abel inversion

$$n_e(r) = -\frac{\lambda c}{\pi^2}\int_r^R \frac{d\phi}{dz}\frac{1}{\sqrt{z^2 - r^2}}dz \tag{2.12}$$

The geometric parameters Z, R, and r are illustrated in Fig. 2.17. The spatial resolution of the interferometry system is determined by the fringe separation, which is adjustable as introduced above. The time resolution of the interferometer setup depends on the pulse width of the probe laser or the detector gating. The minimum density increment δn_e that can be detected depends on the minimum detectable fringe shift. The maximum electron density measurable by interferometry is limited to the critical density of the wavelength of the probe laser. However, when the plasma density is on the order of 1% of the critical density, refraction and opacity effects become significantly so that the accuracy of such diagnostics cannot be ensured.

2.2.5 Particle Kinetics Measurement

In addition to radiate the 13.5 nm in-band EUV emission, the DPP EUV source will also produce debris in the forms of energetic ions, neutral particles, and out-of-band

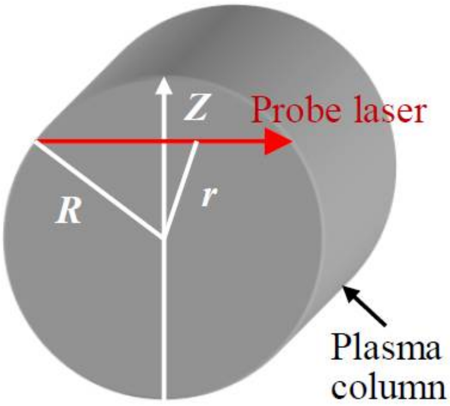

FIGURE 2.17: Plasma column and geometric parameters for Abel inversion.

emission[109]. The debris produced from the ablation of the electrode is an especially severe issue. The ionized and neutral particle flux can cause the sputtering and implantation of the debris species into the MLM coating, lowering its reflectivity[110]. In order to meet the requirements of HVM EUV lithography, the lifetime of the MLMs must last a long time. Several mitigation schemes have been proposed to improve the lifetime of the MLM, for example, magnetic fields[111–113], gas curtain[109, 114], low energy prepulse[115], and mass-limited target for LPP sources[116, 117].

Several intrusion methods are available to measure the velocity and energy distribution of charged particles in Z-pinch. They are FC, Langmuir probe, energy analyzers, and the multichannel plate (MCP) Among them, FC is the most popular and simplest method. They provide an integrated ion signal containing all charge states, and the space charge effects could distort the FC signal[118]. Nevertheless, it is still a very useful tool to obtain the integrated ion flux, the velocity of the ions, and thus the kinetic energy (KE) distribution.

In general, the FC measurement system consists of a metal cup, a bias circuit, and a detect circuit. Since both electrons and ions exist in gas discharge produced plasmas, a negative bias voltage is applied to the FC through the bias circuit to repel electrons from being collected and get the saturated ion current. The saturated current signal $I(t)$

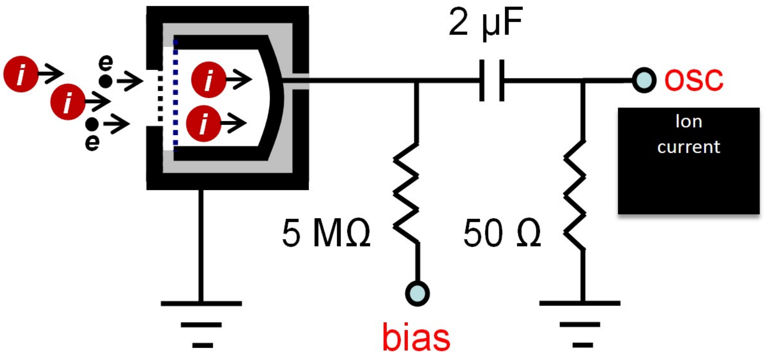

FIGURE 2.18: Schematic of the Faraday Cup system.

can be written as

$$I(t) \propto \sum_z N_z(t) \cdot z \tag{2.13}$$

where N_z is the number of the ion with the valence of Z. An important error source needs to be considered when design a FC system is the secondary electron emission caused by the ion bombardment to the inside wall of the metal cup. The secondary electron emission will enlarge the current signal, hence, cause a deviation from the real value. In order to eliminate the influence of the secondary electron on the FC signal, either passive or active method can be applied. The passive methods include: 1) making deeper and narrower cup, and 2) choosing proper cup material that generates fewer secondary electrons, for example, one can coat the inside of the metal cup with graphite. On the other hand, the active methods include: 1) magnetic field confinement of electrons, and 2) placing a metal mesh at the entrance of the FC, since the metal mesh is capable of capturing the secondary electrons and forcing the electrons to flow back to the cup when it is charged with a negative voltage. In the FC experiment reported here, a negative voltage signal is adopted to bias the FC to collect the ions. The FC is mounted in the radial direction of the Z-pinch to monitor the ion flux in radial direction, which may damage the optics in the lithography system. The schematic of the FC system to measure the ion kinetics is shown in Fig. 2.18.

Typical FC signal with 200 sccm He gas flow rate and -70 V bias voltage is shown in Fig. 2.19. The ion time-of-flight (TOF) profile is represented by a sharp prompt peak,

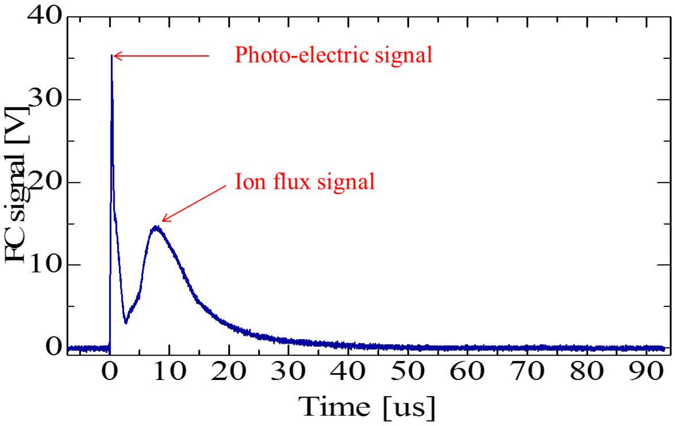

FIGURE 2.19: An example FC signal with 200 sccm He gas flow rate and -70 V bias voltage. The first peak is due to the photo electric effect and the second peak is due to the ion flux collected.

followed by a broad slower peak.The first peak signal is due to the photo electric effect, whose TOF can be neglected; and the second peak is due to the ion flux that is collected by the FC, which has a much longer TOF than light. The first peak is often used as a time marker.

The radial velocity in given by

$$v = \frac{d}{TOF} \tag{2.14}$$

where d is the distance from the Z-axis to the FC. Kinetic Energy (KE) is

$$KE = \frac{mv^2}{2} \tag{2.15}$$

Here we assume the charge state of collected Xe ions is Xe^{1+}, therefore the current density can be converted into a flux, Γ:

$$I = \mathbf{j} \cdot \mathbf{A} = q\mathbf{A} \cdot \mathbf{\Gamma} \tag{2.16}$$

where I is the ion current collected by FC, $\mathbf{j}$ is the current density, $\mathbf{A}$ is the collection area and q is the charge of particle, in this case $q = e$. The ion number density can be written as

$$n(t) = \frac{I}{qAv} \tag{2.17}$$

2.3 Summary

In the first section of this chapter, the experimental setup of the Xe gas jet type EUV source are introduced. In this setup, an RF system working at 13.56 MHz with maximum RF power of 100 W is adopted. It can pre-ionize the Xe gas before sent to the main vacuum chamber, and provide uniform initial plasma distribution which is important to improve the stability of Z-pinch. A double nozzle structure electrode is adopted. Xe gas is ejected through the inner nozzle to form a jet. He gas is supplied through the outer nozzle to form a gas curtain. Such structure can provide a larger collection angle and avoid collecting much debris. The pulsed power supply consists of a gap switch, a high voltage supply, an LC inversion circuit, a 1:3 step-up transformer, and a two-stage MPC. The MPC consists of two magnetic switches. It can compress the pulsed width of the current as well as amplify the current amplitude. The pulsed power supply can provide a pulsed current with peak value of $\sim$22 kA and a rise time of $\sim$110 ns. Such a pulsed current can induce strong magnetic field to compress the plasma to high temperature and high density state, leading to intense EUV radiation.

The diagnostic techniques are introduced in the second section. The EUV emission detector, which consists of a photodiode, a pinhole, and a oscilloscope, can gauge the time-resolved EUV signal. High speed camera is used to record the visible region plasma emission and provide an understanding on the pinch evolution. EUV pinhole imaging system, made up of an x-ray CCD camera, a pinhole of 50 μm in diameter, and a Zr filter with band pass region of 7$\sim$16 nm, is adopted to record the time-integrated EUV emission. It can also provide some information on pinch dynamics, e.g., instabilities in Z-pinch, which will be discussed in Chapter 3. In terms of the electron density measurement, Nomarski interferometer is adopted. It consists of a Nd:YAG laser (532 nm), two polarizers, a Wollaston prism, a high speed camera (Imacon 468), several lenses and several mirrors. The fringe shift is formed in the interferogram is plasma present. Then, the electron density profile can be calculated by means of Abel inversion. Finally, FC is introduced, which is used to diagnose the particle kinetics. The TOF profile is obtained through the FC, and by assuming the constant velocity of each particle species, the velocity spectrum can be calculated.

Chapter 3

Experimental Results of Plasma Diagnostics

In order to find suitable conditions for producing EUV source, quantitatively study the EUV emission characteristics and the plasma dynamics are necessary. This chapter presents the experimental results of the plasma diagnostics. The EUV emission and preferred experimental conditions are quantified. The plasma dynamics in the DPP source are studied extensively through temporal plasma imaging, EUV pinhole imaging, and interferometry, respectively. The existence of EUV emission fluctuation due to MRT instability, whose characteristic wavelength of $\sim$1 mm, is observed through pinhole imaging. The particle kinetics of ions in decay phase is also characterized. The relations between EUV emission and experimental parameters (e.g. inlet gas pressure) or physical parameters (e.g. evolution of electron density) are clarified.

3.1 EUV Emission vs Experimental Parameters

The EUV emission can be influenced by various experimental parameters, for example, the inlet gas pressure, RF pre-ionization power, electrode gap length, etc. In this section, the relationship between the EUV output and those parameters is clarified. Only relative EUV signal intensities are presented as the absolute calibration of the emission detection system is not available.

Fig. 3.1 shows the EUV signal and its corresponding pulsed current waveforms for inlet gas pressures from 10 to 35 Torr with an interval of 5 Torr. The electrode gap length is 16 mm, and RF pre-ionization power is 60 W. The EUV emission is weak ($\sim$ 3 V) when Xe gas input pressure is 10 Torr. The figure tells us that by increasing the inlet gas pressure, the EUV signal waveform can be delayed. In a Z-pinch, the magnetic pressure compresses the plasma and thus plasma pressure increases, which impedes the implosion. Higher initial density means higher plasma pressure and leads to the slower plasma implosion. It essentially changes the pinch time, pinch radius, electron density and temperature at pinch stagnation, etc. A detailed analysis based on MHD simulation will be given in Chapter. 5.

Fig. 3.2 illustrates the relationship between EUV signal intensity and inlet gas pressure for electrode gap lengths of 8 mm, 12 mm, 16 mm, and 20 mm, respectively. From 10 to 25 Torr, the EUV signal increases as the gas pressure increases. The maximum EUV output is realized at gas pressure of 25 Torr. When the pressure exceeds 25 Torr, however, the EUV singal decreases if the pressure is further increased. A qualitative explanation is that, from 10 to 25 Torr, more Xe ions participate into the implosion and contribute to the EUV radiation. However, by further increasing the inlet gas pressure, the pinch radius will be bigger which causes the decreasing of electron temperature at pinch stagnation; therefore the EUV emission signal becomes weak in the pressure range of 25 to 35 Torr.

The relationship between the EUV emission signal and electrode gap length for gas inlet pressures of 25 Torr (red) and 30 Torr (green) is shown in Fig. 3.3. The EUV emission reaches the peak at electrode gap length of 16 mm. Note that changing the electrode gap length only increases EUV output by 40%, whereas changing the Xe gas pressure

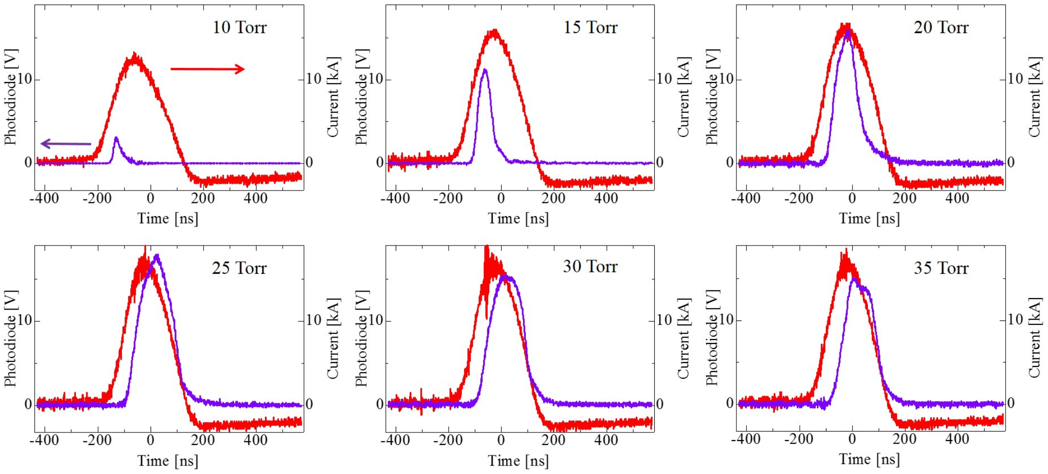

FIGURE 3.1: The EUV signal and its corresponding pulsed current waveforms for various input gas pressures. The electrode gap length is fixed at 16 mm, RF pre-ionization power is fixed at 60 W, and He gas curtain is not applied.

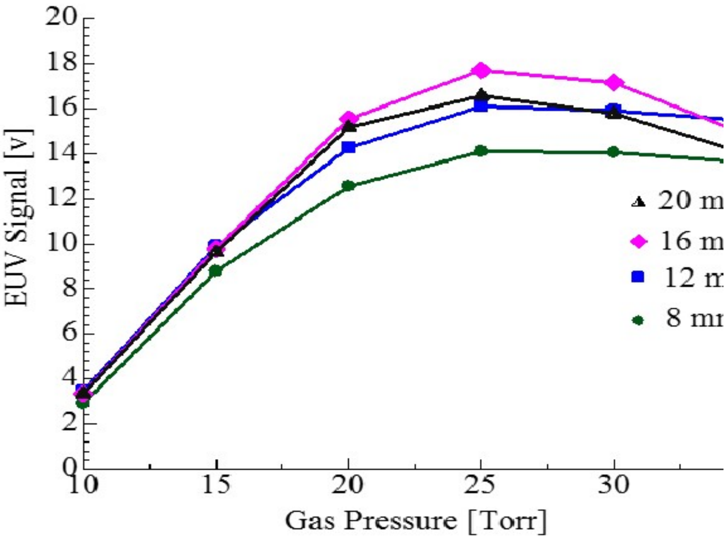

FIGURE 3.2: The EUV emission signal in arbitary unit (a.u.) vs input gas pressure for different electrode gap length.

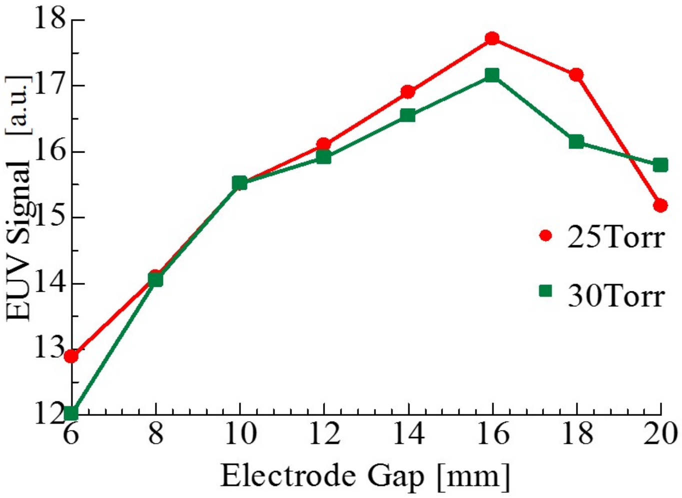

FIGURE 3.3: The EUV emission signal vs electrode gap length for gas input pressure of 25 Torr (red) and 30 Torr (green).

can increase EUV output by up to 300–400%. Thus, Xe gas pressure plays a more important role in determining EUV output than that of electrode gap length. Also, one should note that these "optimum conditions" are in terms of those parameters which can be changed by the experimentalist.

The relationship between the EUV emission signal and RF pre-ionization power with (red) and without (blue) He gas curtain is shown in Fig. 3.4. The electrode gap length is 16 mm and Xe input gas pressure is 25 Torr. By applying He gas curtain, the EUV intensity is enhanced, because the gas curtain can confine the Xe gas in a smaller initial radius so that more particles will take part in the Z-pinch. On the other hand, the increasing of the RF pre-ionization power causes the EUV signal intensity decreases unexpectedly. In general, it is believed that pre-ionization can enhance the stability of Z-pinch[90] and therefore helpful to realize higher EUV emission output.

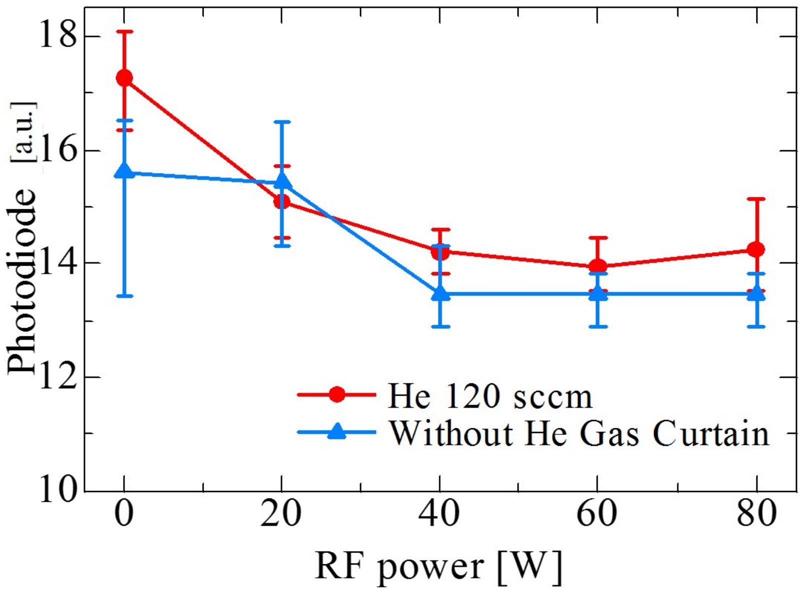

FIGURE 3.4: The EUV emission signal vs RF pre-ionization power with electrode gap length of 16 mm and Xe inlet gas pressure of 25 Torr with (red) 120 sccm He gas curtain and w/o (blue) He gas curtain.

3.2 Time-resolved Plasma Imaging

The framing photographs of the plasma images in visible region for input gas pressure of 24 Torr and RF pre-ionization power of 10 W are shown in Fig. 3.5. The observation domain is 6.3 mm in length and 4.3 mm in height. The photos in red quadrilateral are the standard ones whose brightnesses have not been intensified. The brightnesses have been intensified for 5 times for photos in green quadrilateral, and 100 times for the ones in violet quadrilateral. In the initial phase (65ns), discharge starts and the Xe gas near the cathode nozzle is weakly ionized, thus the visible emission is also weak. The initial pinch radius can be estimated through this figure, which is several mm. Relatively strong emission can be observed since 90 ns. Near the cathode region, a corn sheet shaped emission region is formed. At 107 ns, the radiating plasma volume has been compressed to be a column whose diameter is on the order of 0.1 mm, accompanied with strong emission. With the further evolution of the Z-pinch, the radiating column is

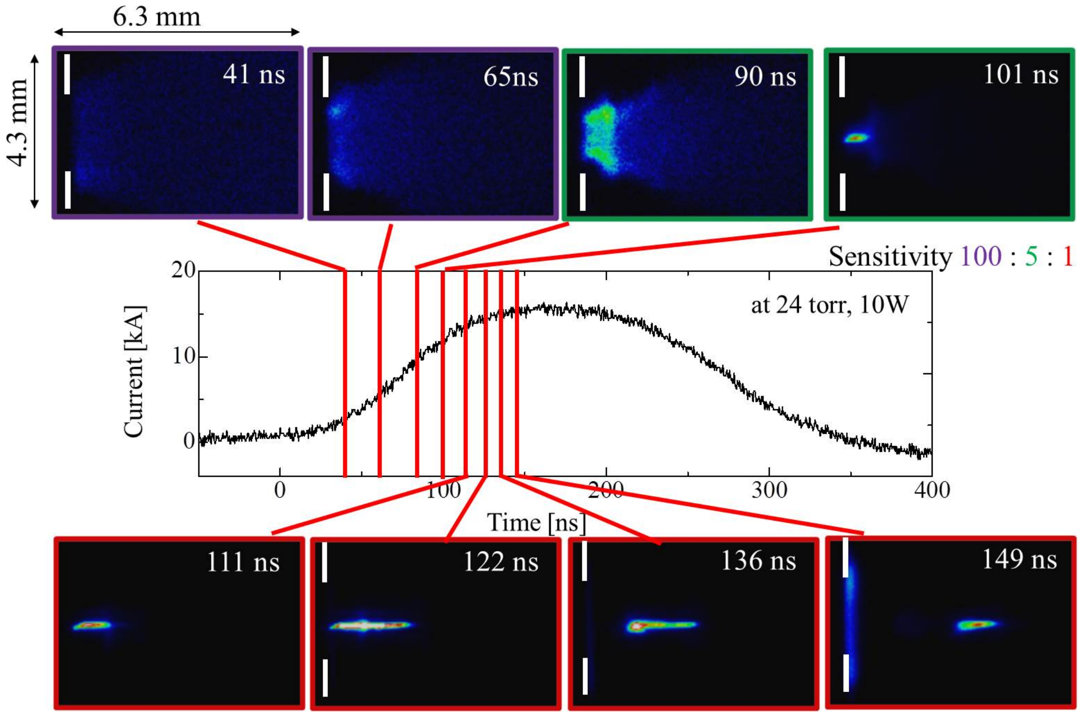

FIGURE 3.5: Framing photographs of the plasma imaging in visible region in Z-pinch gas discharge for gas inlet pressure of 24 Torr, and RF pre-ionization power of 10 W. The time resolution is 10 ns

elongated and then moves along Z axis, which is a typical Zippering effect[119].

3.3 Time-integrated Plasma Imaging

In order to optimized the EUV emission, time-integrated study is also necessary which can provide the information concerning the relative output power, size of the radiating spot, etc. The time-integrated pinhole images of the DPP EUV source with the electrode gap length of 10 mm, Xe gas pressure of 24 Torr, and RF power ranging from 10 to 70 W at an interval of 5 W are shown in Fig. 3.6. According to the EUV pinhole images taken under various RF powers, it is easy to find that when the RF power is low, the Z-pinch suffers from instability. When the RF powers is high enough, the instability phenomenon is negligible because adequate pre-ionization can provide a uniform initial plasma distribution thus stabilize the Z-pinch.

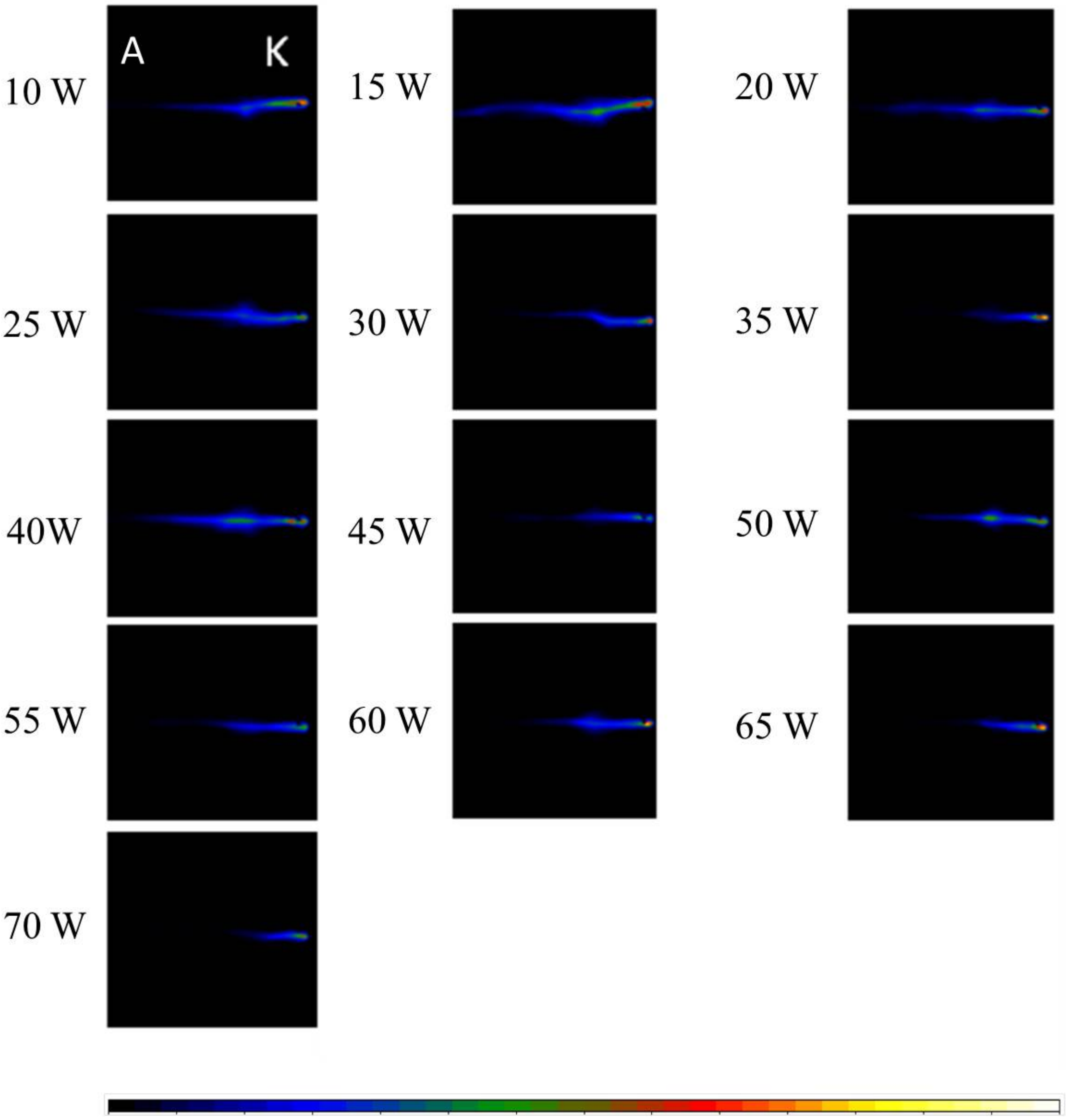

FIGURE 3.6: Time-integrated pinhole image of the EUV when the electrode gap length is fixed at 10 mm, Xe gas pressure is fixed at 24 Torr. The RF power ranges from 10 to 70 W at an interval of 5 W

The relative time-integrated EUV emission intensity as a function of RF power at fix gas inlet pressure of 24 Torr and electrode gap length of 10 mm is shown in Fig. 3.7. The data shown in the figure is the average result of three experimental data. This result is in consistent with those obtained with photodiode, that is, by increasing the RF power, the EUV emission intensity decreases. The reason for this result will be addressed in Chapter 5.

By changing the distance from the RF coil to cathode d, which is shown in Fig. 2.14, the EUV pinhole images differ significantly under fixed inlet gas pressure of 24 Torr

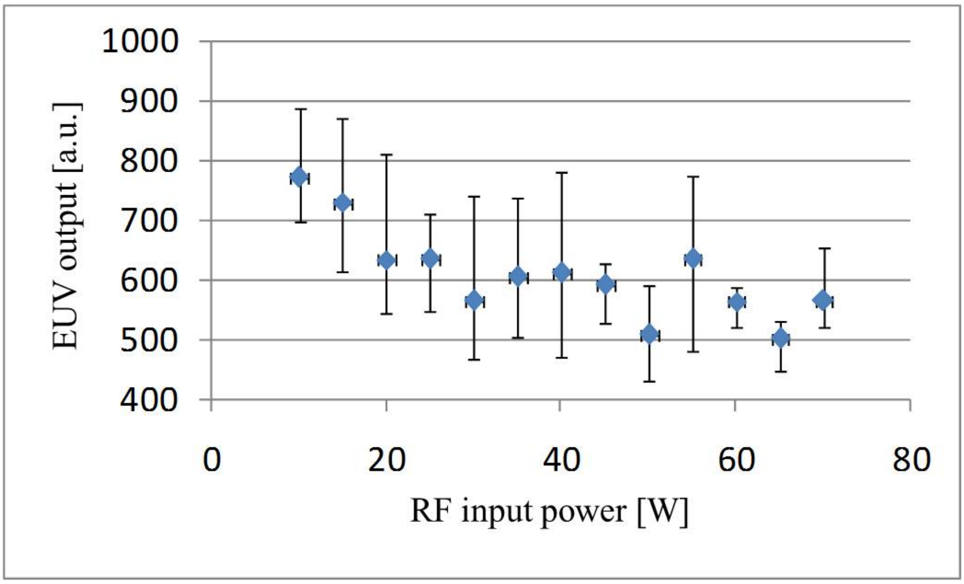

FIGURE 3.7: Relative time-integrated EUV emission intensity as a function of RF power at fix gas input pressure of 24 Torr and electrode gap length of 10 mm

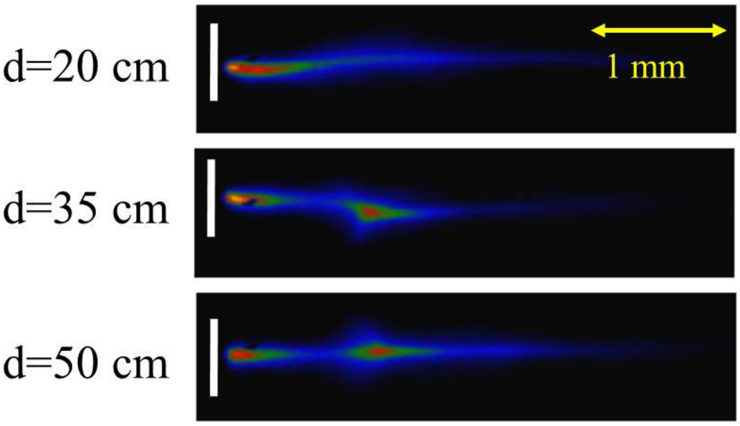

FIGURE 3.8: EUV pinhole image versus the distance of RF coil from electrode of d=20 cm, 35 cm, and 50 cm, respectively. The inlet gas pressure is fixed at 24 Torr and the RF power is 10 W

and fixed RF power of 10 W, as shown in Fig. 3.8. When the RF coil is close to the main discharge, a relative uniform pinch column is formed; on the other hand, if the RF coil is far away from the electrode, instabilities appear. The reason will be explained in Sec. 5.2.2.

3.4 Electron Density Evolution during Z-pinch

As one of the most important parameters in physics of Z-pinch plasma, the electron density plays a significant role in determining the EUV output[95, 96]. In this section, we report the experimental results on the temporal electron density evolution in the Z-pinch gas discharge. Nomarski interferometry was assembled for this experiment. The fringe pattern due to the electron density distribution in the plasma column is recorded by a high speed camera Imacon 456. Then we use Abel inversion to calculate the 2-D electron density distribution profile. Abel inversion requires the axisymmetry of the plasma column[120]. Therefore in the calculation, the plasma column was divided into upper and bottom semi-column in the direction of the Z axis. It was also assumed that both semi-columns are axisymmetric. The position for separating the upper and bottom semi-column was chosen as that where there is minimal difference of electron densities of the upper and bottom parts. In addition, we also assumed that the only factor contributing to the refractive index changes of the plasma was the free electrons. This assumption is justified by the facts that the influence of the magnetic field to the fringe shift is negligible compared to that of the electrons. In addition, it is assumed that there are no transitions of Xe atoms or ions within ± 1 nm of the probe laser wavelength (532 nm)[121].

An example of fringe pattern at electrode gap length of 16 mm, Xe gas pressure of 15 Torr, and He gas curtain of 200 sccm is shown in Fig. 3.9(a). The time recorded the fringe pattern is shown by a vertical red line in Fig. 3.9(b). The exposure time of the high speed camera is 10 ns.

By importing the fringe pattern into Abel inversion code, the electron density distribution profile can be calculated, which is shown in Fig. 3.10. One can see that in this case at an axial position of 1 mm from the cathode, the plasma has been pinched and the peak density is about 4×10^{18} cm^{-3}, which satisfies the pre-requisite of $n_e \ll n_c$. The minimum diameter of the plasma column at the maximum pinch is about 0.2 mm.

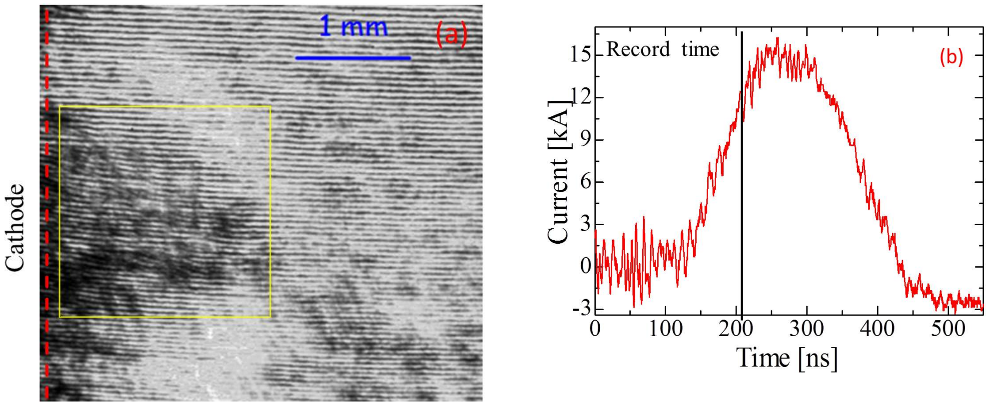

FIGURE 3.9: (a) Fringe pattern of the Nomarski interferometry due to the electron density distribution at electrode gap length of 16 mm, Xe gas input pressure of 15 Torr, and He gas curtain of 200 sccm. (b) the record time of the fringe pattern. The exposure time is 10 ns.

Note that the plasma column close to the cathode does not have the minimum diameter; this shows that the pinch does not occur simultaneously at all axial positions. The electron density evolution is related to the pinch dynamics and is essential for EUV output; therefore it is necessary to have a further understanding of density evolution. The development of density evolution and EUV radiation with current pulse is shown in Fig. 3.11. Initially (100 ns), the electron density is low, EUV signal is almost 0. Since 200 ns, the current pulse rises; electron density and EUV signal also appear and increase. The EUV intensity peaks quite near electron density maximum at about 250 ns. The maximum electron density is about 1×10^{19} cm^{-3}, and consistent with the optimum electron density (10^{18} -10^{19} cm^{-3}) in Refs. [95, 96]. After that, the pinched plasma column expands, lowering the electron density, temperature, and thus EUV signal.

3.5 Particle Kinetics in the Decay Phase

During the implosion phase, the plasma shell accelerates and gains kinetic energy. Since stagnation phase, the kinetic energy is converted into thermal energy. However, the gas pressure of the stagnated plasma will increase significantly thus leading to the radial

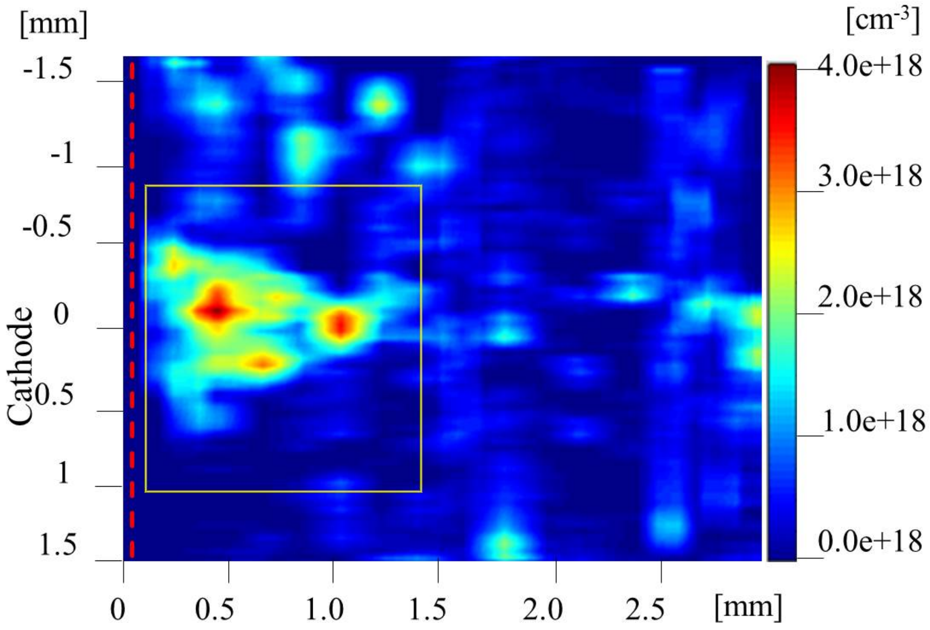

FIGURE 3.10: Electron density distribution corresponding to the fringe pattern in Fig. 3.9(a).

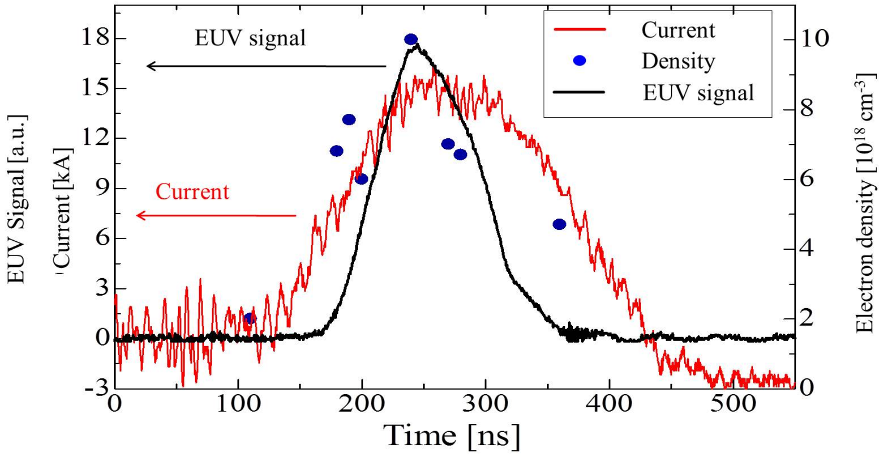

FIGURE 3.11: Development of electron density and EUV intensity with current pulse.

expansion of plasma column. The energetic ions either from the ablation of electrodes or the radial expansion of plasma are important sources of debris, which will damage the optics and restrict the lifetime of the EUV lithography system. In this section, the ion kinetics measured by FC is reported.

A typical FC signal has been shown in previous chapter (see Fig. 2.19 in Chapter. 2). The sharp spike observed at earlier time is the prompt signal that is used as a time marker. In order to gain more insights into the kinetic properties of the plume species, a shifted Maxwell–Boltzmann (SMB) distribution was fitted to the TOF profiles to investigate the kinetic properties of the plume. The SMB fitting function is given by [122]

$$f(v)dv = A(\frac{m_i}{2\pi k_B})^{3/2} v^3 e^{-m_i(v-v_0)^2/2k_BT} dv \tag{3.1}$$

where A is a normalization constant, v and v_0 are the species velocities and the center-of-mass velocity, T the translational temperature, k_B the Boltzmann constant, and m_i the mass of the species. It is assumed here that the speed distribution has equilibrated after propagating a short distance from the target surface. Fig. 3.12 shows the ion velocity spectrum and its corresponding SMB fit with 200 sccm He gas flow rate and -70 V bias voltage. The most probable speed is around 18 km/s. Under closer scrutiny, one could find that the low velocity part fits SMB quite well, while the high velocity part has certain deviations. This is because the low velocity part corresponds to long TOF, and according to Eq. (2.14), even if there is certain measurement error, the velocity uncertainty is small; however, for short TOF, little error may cause obvious velocity uncertainty.

The corresponding kinetic energy spectrum is shown in Fig. 3.13. We find that most ions concentrate in the region where KE $<$ 500 eV, and the number of extreme high KE ions (KE $>$ 1500 eV) is negligible.

The effect of He gas curtain on debris mitigation is also investigated, as shown in Fig. 3.14. With He gas curtain, the total number of ions collected in the radial direction reduces slightly.

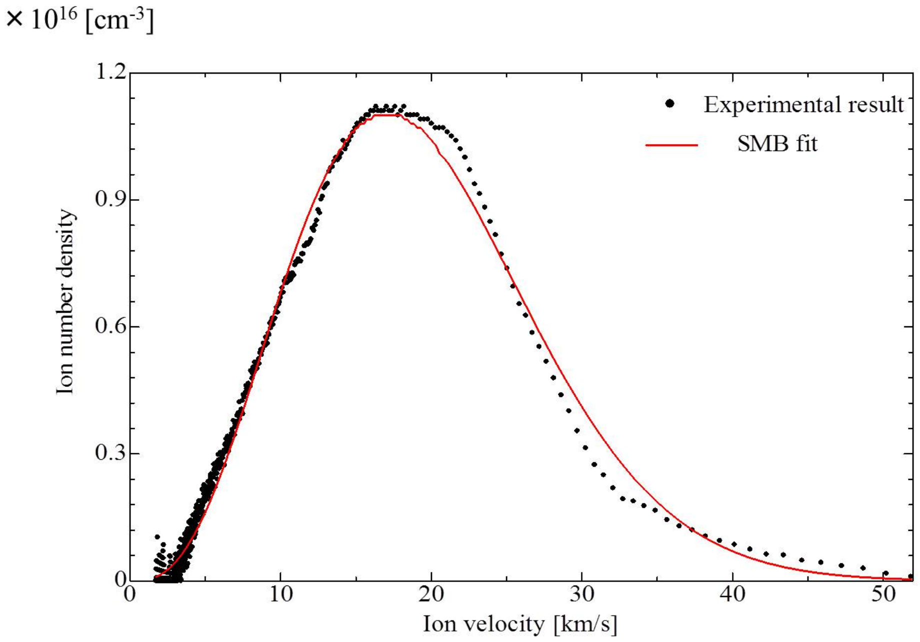

FIGURE 3.12: Ion velocity spectrum (black dot) and its corresponding SMB fit(red line) with 200 sccm He gas flow rate and -70 V bias voltage.

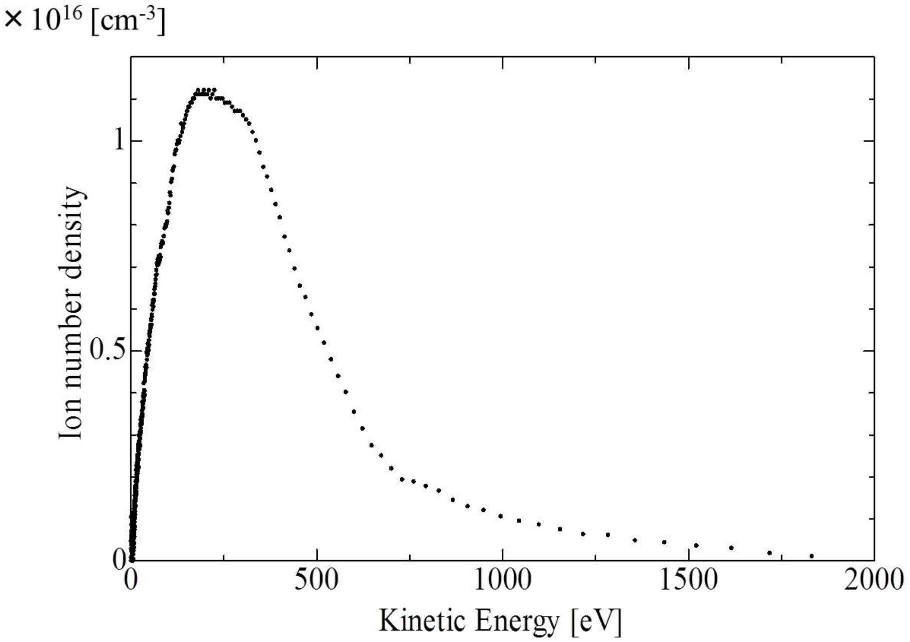

FIGURE 3.13: Corresponding kinetic energy spectrum of Fig. 3.12.

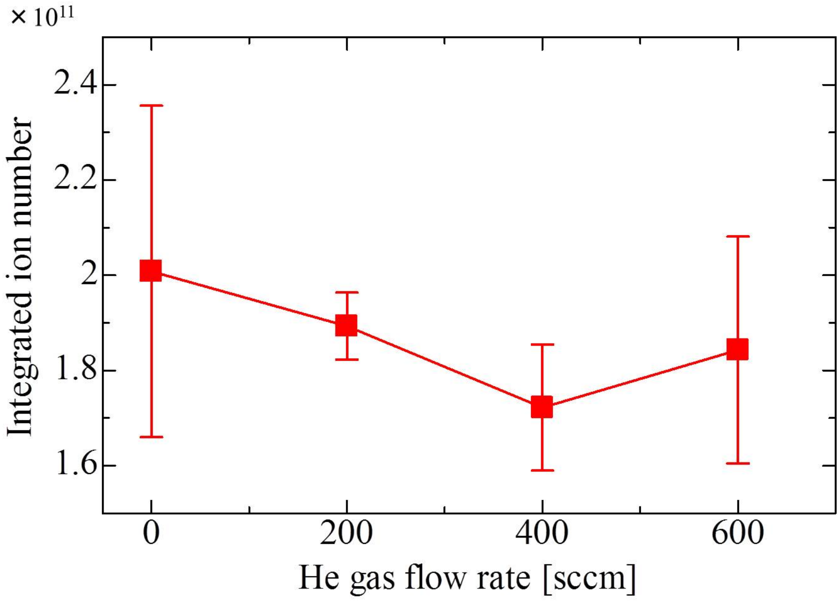

FIGURE 3.14: Influence of He gas curtain on total ion number under different gas flow rate.

3.6 Summary

In the first section of this chapter, the relationship between EUV emission characteristics and experimental parameters was present. Higher gas pressure, thus higher initial density, delays the pinch time and affects the EUV radiation significantly. Besides, the electrode gap length also influenced the EUV output. The optimum inlet gas pressure is 25 Torr, and the optimum electrode gap length is 16 mm. Furthermore, the EUV output was reduced if RF power was increased, the reason will be addressed in Chapter 5 by means of numerical simulation. In the second section, the time-resolved visible region plasma images were present, which provided a direction understanding on the Z-pinch implosion. The diameter of plasma at stagnation was on the order of 0.1 mm. Zippering effect was also confirmed. The EUV pinhole images were shown in the third section. The RF power was demonstrated to be capable of enhance the pinch stability; on the other hand, the RF power plays a negative role on the EUV output, as also shown in Sec. 3.2. The existence of EUV emission fluctuation due to MRT instability, whose characteristic wavelength of $\sim$1 mm, was observed through pinhole imaging.

The electron density evolution during Z-pinch implosion was reported in Sec. 3.4. Abel inversion was adopted to calculate the electron density from the fringe pattern. The electron density is on the order of $10^{18} \sim 10^{19}$ cm^{-3} in the Z-pinch. The EUV intensity peaks quite near electron density maximum ($\sim 10^{19}$ cm^{3}) during the pinch process, in consistent with the theoretical optimum electron density range for EUV radiation. Finally, the ion kinetics measurement results were reported in Sec 3.5. The most probable ion velocity is $\sim$18 km/s. The ion velocity distribution follows SMB fitting.

Chapter 4

Physical Model and Numerical Scheme for Z-pinch Gas Discharge

Simulation is also adopted in this study for two main reasons: 1) To have deeper insights into the plasma dynamics in Z pinch in order to optimize the EUV source. 2) To quantitatively study the MRT instabilities observed in experiment and find methods to mitigate MRT to produce a homogeneous EUV source. This chapter focuses on the construction of physical model and numerical algorithm for solving the governing equations. The MHD model is adopted to describe the physical process. It can include some important processes, e.g., heat conduction, magnetic diffusion, and provide much more valuable information than simple analytical model. On the other hand, it also avoid too detailed descriptions in Vlasov equation. The construction of the MHD model starts from general conservation law in ideal case. The derivation of ideal MHD equations in Cartesian coordinate system are given in Sec. 4.1.1. Then, the equations are transformed to cylindrical coordinates in Sec. 4.1.2. In addition, non-convective terms, i.e. heat transfer and magnetic diffusion, are taken into account in Sec. 4.1.3. In Sec. 4.1.4, the two-temperature approximation is adopted so that the energy equation is separated into two: one for ions and the other for electrons. The diffusion terms are treated implicitly, which is reported in Sec. 4.2.1. The Total Variation Diminishing scheme in

Lax-Frieddrich formulation (TVD-LF) is present in Sec. 4.2. It is a robust algorithm to solve the hyperbolic part of the governing equations explicitly.

4.1 MHD Model for Z-pinch Gas Discharge

This section describes an integrated model for modeling of DPP devices in cylindrical geometry. The MHD model is based on single-fluid, two-temperature approximation. Important processes, including thermal diffusions of electrons and ions, magnetic induction, and atomic processes are incorporated into the model. All equations and transformations are written in Gaussian units, unless stated otherwise.

4.1.1 General Laws of Plasma Motion

The conservation law of any parameter q can be given in differential form:

$$\frac{\partial q}{\partial t} + \nabla \cdot (\mathbf{F}_q) = 0, \tag{4.1}$$

where $\mathbf{F}_q$ is the flux of this parameter. If we assume the plasma to be compressible and continuous, we can derive conservation equations for mass, momentum, and energy respectively from Eq. (4.1)

$$\frac{\partial \rho}{\partial t} + \nabla \cdot (\rho \mathbf{v}) = 0, \tag{4.2a}$$

$$\frac{\partial (\rho \mathbf{v})}{\partial t} + \nabla \cdot (\rho \mathbf{v}\mathbf{v} + p_h) = 0, \tag{4.2b}$$

$$\frac{\partial e_h}{\partial t} + \nabla \cdot (\mathbf{v}(e_h + p_h)) = 0. \tag{4.2c}$$

where ρ is the plasma density, $\mathbf{v}$ the velocity of plasma, p_h the hydrodynamic pressure, and $e_h = \dfrac{(\rho v^2)}{2} + e_{int}$ the sum of kinetic and internal energy densities of plasma.

The equation set (4.2) describes convective motion of a compressible homogeneous medium. Additional external forces and sources will be added, and dissipative terms will be taken into account to derive actual plasma model.

Any current can be the source of a magnetic field in the plasma, and this magnetic field is the source of forces that disturb the initial plasma. This self-consistent process should be included in the hydrodynamic equation set (4.2). Moreover, the conservative form of the set should not be changed. Therefore, it is appropriate to introduce an additional conservative variable: magnetic field $\mathbf{B}$. To keep the conservative form of the initial equation, we does not operate with currents directly. Any external force $\mathbf{F}_{ex}$ can be added into Eq. (4.2) as follows:

$$\frac{\partial \rho}{\partial t} + \nabla \cdot (\rho \mathbf{v}) = 0, \tag{4.3a}$$

$$\frac{\partial (\rho \mathbf{v})}{\partial t} + \nabla \cdot (\rho \mathbf{v}\mathbf{v} + p_h) = \mathbf{F}_{ex}, \tag{4.3b}$$

$$\frac{\partial (e_h)}{\partial t} + \nabla \cdot (\mathbf{v}(e_h + p_h)) = \mathbf{v} \cdot \mathbf{F}_{ex}, \tag{4.3c}$$

In the general case of magnetic hydrodynamics, external forces can be expressed as forces that act on a unit charge, such as force field strength $\mathbf{E}$. It may be given as the sum of three forces: Lorenz, electrical field, and Hall force:

$$\mathbf{E} = -\frac{\mathbf{v} \times \mathbf{B}}{c} + \eta \mathbf{j} + \frac{h_c}{\rho} \mathbf{j} \times \mathbf{B} \tag{4.4}$$

4.1.1.1 Continuity equation

The mass conservation equation keeps its form in the MHD case. The vector form is the same as Eq. (4.3a). The tensor form reads

$$\frac{\partial \rho}{\partial t} + \frac{\partial (\rho v_k)}{\partial x_k} = 0 \tag{4.5}$$

Here and elsewhere we have in mind summation by repeating index.

4.1.1.2 Momentum equation

Only the Lorenz force is taken into account by transformations of the equation of motion; thus we have $\mathbf{F}_{ex} = \frac{1}{c}\,\mathbf{j} \times \mathbf{B}$. According to Ampere's law

$$\nabla \times \mathbf{B} = \frac{\mu}{c}(4\pi \mathbf{j} + \frac{\partial \mathbf{D}}{\partial t}). \tag{4.6}$$

Neglecting the displacement current $\frac{\partial \mathbf{D}}{\partial t}$, we have equation of motion in vector form:

$$\frac{\partial(\rho \mathbf{v})}{\partial t} + \nabla \cdot (\rho \mathbf{v}\mathbf{v} + p_h) - \frac{1}{4\pi\mu}(\nabla \times \mathbf{B}) \times \mathbf{B} = 0 \tag{4.7a}$$

In tensor form, it is

$$\frac{\partial(\rho v_i)}{\partial t} + \frac{\partial}{\partial x_k}(\rho v_i v_k + p_h \delta_{ik} + \frac{B^2 \delta_{ik}}{8\pi\mu} - \frac{1}{4\pi\mu}(B_k B_i)) = -\frac{1}{4\pi\mu} B_i \frac{\partial B_k}{\partial x_k} \tag{4.7b}$$

4.1.1.3 Energy equation

By taking into account of Eq. (4.4), we derive the energy equation from Eq. (4.3c):

$$\frac{\partial e_h}{\partial t} + \nabla \cdot (\mathbf{v}(e_h + p_h)) = \mathbf{j} \cdot \mathbf{E} \tag{4.8}$$

Combing with Ampere's law, we have

$$\frac{\partial e_h}{\partial t} + \nabla \cdot (\mathbf{v}(e_h + p_h)) = \frac{c}{4\pi\mu}(\nabla \times \mathbf{B}) \cdot \mathbf{E} \tag{4.9}$$

Here we assume that the Hall term is negligible. Through theoretical calculation, the energy equation in vector form is given by

$$\frac{\partial e_{tot}}{\partial t}+\nabla\cdot[\mathbf{v}(e_{tot}+p_{tot})-\frac{1}{4\pi\mu}[\mathbf{v}\cdot\mathbf{B}]\cdot\mathbf{B}+\frac{c^2\eta}{16\pi^2}\mu^2(\nabla\times\mathbf{B})\times\mathbf{B}]=-\frac{1}{4\pi\mu}(\mathbf{v}\cdot\mathbf{B})\cdot\nabla\cdot\mathbf{B} \tag{4.10a}$$

In tensor form, it is

$$\begin{aligned}\frac{\partial e_{tot}}{\partial t}+\frac{\partial}{\partial x_k}[v_k(e_{tot}+p_{tot})-\frac{B_kB_mv_m}{4\pi\mu}+\frac{c^2}{16\pi^2\mu^2}(\eta\frac{\partial B_k}{\partial x_m}B_m)\\ -\frac{c^2}{32\pi^2\mu^2}(\eta\frac{\partial B^2}{\partial x_k})]=-\frac{1}{4\pi\mu}B_pv_p\frac{\partial B_k}{\partial x_k}\end{aligned} \tag{4.10b}$$

where $e_{tot}=e_h+\frac{B^2}{8\pi\mu}$ and $p_{tot}=p_h+\frac{B^2}{8\pi\mu}$.

4.1.1.4 Faraday's equation

To close the hydrodynamic equations set, external force must be taken into account, which can be obtained from Faraday's equation. Faraday's equation should be reduced to the conservative form just as the magnetic field conservation law. Through theoretical derivation, we have conservative form of Faraday's equation with in vector form:

$$\frac{\partial\mathbf{B}}{\partial t}+\nabla\cdot(\mathbf{vB}-\mathbf{Bv})+\frac{c^2}{4\pi\mu}\nabla\times(\eta\nabla\times\mathbf{B})=-\mathbf{v}(\nabla\cdot\mathbf{B}). \tag{4.11a}$$

In tensor form, it is

$$\frac{\partial B_i}{\partial t}+\frac{\partial}{\partial x_k}(v_kB_i-B_kv_i+\frac{c^2\eta}{4\pi\mu}(\frac{\partial B_k}{\partial x_i}-\frac{\partial B_i}{\partial x_k}))=-v_i\frac{\partial B_k}{\partial x_k}. \tag{4.11b}$$

Therefore it is possible to write a general system of MHD equations in orthogonalized Cartesian coordinates in tensor form:

$$\begin{cases} \dfrac{\partial \rho}{\partial t} + \dfrac{\partial (\rho v_k)}{\partial x_k} = 0, \\ \\ \dfrac{\partial (\rho v_i)}{\partial t} + \dfrac{\partial}{\partial x_k}(\rho v_i v_k + p_h \delta_{ik} + \dfrac{B^2 \delta_{ik}}{8\pi\mu} - \dfrac{1}{4\pi\mu}(B_k B_i)) = -\dfrac{1}{4\pi\mu} B_i \dfrac{\partial B_k}{\partial x_k}, \\ \\ \dfrac{\partial e_{tot}}{\partial t} + \dfrac{\partial}{\partial x_k}[v_k(e_{tot} + p_{tot}) - \dfrac{B_k B_m v_m}{4\pi\mu} + \dfrac{c^2}{16\pi^2\mu^2}(\eta \dfrac{\partial B_k}{\partial x_m} B_m) - \\ \\ \dfrac{c^2}{32\pi^2\mu^2}(\eta \dfrac{\partial B^2}{\partial x_k})] = -\dfrac{1}{4\pi\mu} B_p v_p \dfrac{\partial B_k}{\partial x_k}, \\ \\ \dfrac{\partial B_i}{\partial t} + \dfrac{\partial}{\partial x_k}(v_k B_i - B_k v_i + \dfrac{c^2 \eta}{4\pi\mu}(\dfrac{\partial B_k}{\partial x_i} - \dfrac{\partial B_i}{\partial x_k})) = -v_i \dfrac{\partial B_k}{\partial x_k}. \end{cases} \tag{4.12}$$

The equation set (4.12) can be directly used for 3D calculation. The corresponding vector form is

$$\begin{cases} \dfrac{\partial \rho}{\partial t} + \nabla \cdot (\rho \mathbf{v}) = 0, \\ \\ \dfrac{\partial (\rho \mathbf{v})}{\partial t} + \nabla \cdot (\rho \mathbf{v}\mathbf{v} + p_{tot} - \dfrac{\mathbf{B}\mathbf{B}}{4\pi\mu}) = -\dfrac{1}{4\pi\mu} \mathbf{B}(\nabla \cdot \mathbf{B}), \\ \\ \dfrac{\partial e_{tot}}{\partial t} + \nabla \cdot [\mathbf{v}(e_{tot} + p_{tot}) - \dfrac{1}{4\pi\mu}(\mathbf{v} \cdot \mathbf{B}) \cdot \mathbf{B}] = -\dfrac{1}{4\pi\mu}(\mathbf{v} \cdot \mathbf{B}) \cdot (\nabla \cdot \mathbf{B}), \\ \\ \dfrac{\partial \mathbf{B}}{\partial t} + \nabla \cdot (\mathbf{v}\mathbf{B} - \mathbf{B}\mathbf{v}) = -\mathbf{v}(\nabla \cdot \mathbf{B}). \end{cases} \tag{4.13}$$

4.1.2 Cylindrical Case of MHD Equations

The DPP device is an axisymmetry system; therefore the MHD equations should be transformed to cylindrical coordinate system. In current study, we neglect the plasma motion along ϕ direction and assume the magnetic field has only azimuthal component B_ϕ. The code can be upgrade to include the azimuthal plasma motion easily if necessary.

The continuity equation in cylindrical coordinate system reads

$$\frac{\partial \rho}{\partial t} + \frac{1}{r}\frac{\partial}{\partial r}(r\rho v_r) + \frac{1}{r}\frac{\partial}{\partial \phi}(\rho v_\phi) + \frac{\partial}{\partial z}(\rho v_z) = 0. \tag{4.14}$$

The derivation of the momentum equation is a little complicated, the final equation in the cylindrical coordinate system in projection to the r, ϕ, and z axes reads

$$\begin{aligned}
&\frac{\partial \rho v_r}{\partial t} + \frac{1}{r}\frac{\partial}{\partial r} r(\rho v_r v_r - \frac{B_r B_r}{4\pi\mu}) + \frac{1}{r}\frac{\partial}{\partial \phi}(\rho v_r v_\phi - \frac{B_r B_\phi}{4\pi\mu}) + \frac{\partial}{\partial z}(\rho v_r v_z - \frac{B_r B_z}{4\pi\mu}) \\
&+\frac{\partial p_{tot}}{\partial r} - \frac{\rho v_\phi v_\phi}{r} + \frac{B_\phi B_\phi}{4\pi\mu r} = -\frac{B_z}{4\pi\mu r}\frac{\partial (rB_r)}{\partial r} - \frac{B_z}{4\pi\mu r}\frac{\partial B_\phi}{\partial \phi} - \frac{B_z}{4\pi\mu}\frac{\partial B_z}{\partial z}.
\end{aligned} \tag{4.15}$$

The energy equation in cylindrical coordinate system is given as follows

$$\begin{aligned}
&\frac{\partial e_{tot}}{\partial t} + \frac{1}{r}\frac{\partial}{\partial r}(r[v_r(e_{tot} + p_{tot}) - \frac{B_r \mathbf{Bv}}{4\pi\mu}]) + \frac{1}{r}\frac{\partial}{\partial \phi}(v_\phi[e_{tot} + p_{tot}] - \frac{B_\phi \mathbf{Bv}}{4\pi\mu}) + \\
&\frac{\partial}{\partial z}(v_z[e_{tot} + p_{tot}] - \frac{B_z \mathbf{Bv}}{4\pi\mu}) = -\frac{\mathbf{Bv}}{4\pi\mu r}\frac{\partial (rB_r)}{\partial r} - \frac{\mathbf{Bv}}{4\pi\mu r}\frac{\partial B_\phi}{\partial \phi} - \frac{\mathbf{Bv}}{4\pi\mu}\frac{\partial B_z}{\partial z}.
\end{aligned} \tag{4.16}$$

The Faraday's equations in $\vec{e}_r$, $\vec{e}_\phi$, and $\vec{e}_z$ directions can be written as

$$\begin{cases} \frac{\partial B_r}{\partial t}+\frac{1}{r}\frac{\partial[v_\phi B_r-B_\phi v_r]}{\partial\phi}+\frac{\partial[v_z B_r-B_z v_r]}{\partial z}=-v_r[\frac{1}{r}\frac{\partial(rB_r)}{\partial r}+ \\ \frac{1}{r}\frac{\partial(B_\phi)}{\partial\phi}+\frac{\partial(B_z)}{\partial z}], \\ \frac{\partial B_\phi}{\partial t}+\frac{1}{r}\frac{\partial[r(v_r B_\phi-B_r v_\phi)]}{\partial r}+\frac{\partial[v_z B_\phi-B_z v_\phi]}{\partial z}+\frac{v_\phi B_r}{r}-\frac{B_\phi v_r}{r}= \\ -v_\phi[\frac{1}{r}\frac{\partial(rB_r)}{\partial r}+\frac{1}{r}\frac{\partial B_\phi}{\partial\phi}+\frac{\partial B_z}{\partial z}], \\ \frac{\partial B_z}{\partial t}+\frac{1}{r}\frac{\partial[r(v_r B_z-B_r v_z)]}{\partial r}+\frac{1}{r}\frac{\partial[v_\phi B_z-B_\phi v_z]}{\partial\phi}=-v_z[\frac{1}{r}\frac{\partial(rB_r)}{\partial r} \\ +\frac{1}{r}\frac{\partial B_\phi}{\partial\phi}+\frac{\partial B_z}{\partial z}]. \end{cases} \tag{4.17}$$

Modeling the laboratory plasmas should take the non-ideal diffusive magnetic effect into account. Dissipation of magnetic energy appears in the form of Joule heating in the energy equation and the diffusive term in Faraday's equation.

$$\begin{aligned} \frac{c^2}{16\pi^2\mu^2}\nabla[\eta(\nabla\times\mathbf{B})\times\mathbf{B}] &= \frac{c^2}{16\pi^2\mu^2 r}\frac{\partial}{\partial r}[r\eta(B_z(\frac{\partial B_r}{\partial z}-\frac{\partial B_z}{\partial r})-\frac{B_\phi}{r}(\frac{\partial(rB_\phi)}{\partial r}-\frac{\partial B_r}{\partial\phi}))] \\ &+\frac{c^2}{16\pi^2\mu^2 r}\frac{\partial}{\partial\phi}[\eta(\frac{B_r}{r}(\frac{\partial(rB_\phi)}{\partial r}-\frac{\partial B_r}{\partial\phi})-B_z(\frac{1}{r}\frac{\partial B_z}{\partial\phi}-\frac{\partial B_\phi}{\partial z}))] \\ &+\frac{c^2}{16\pi^2\mu^2}\frac{\partial}{\partial z}[\eta(B_\phi(\frac{1}{r}\frac{\partial B_z}{\partial\phi}-\frac{\partial B_\phi}{\partial r})-B_r(\frac{\partial B_r}{\partial z}-\frac{\partial B_z}{\partial r}))]. \end{aligned} \tag{4.18}$$

Faraday's equation with resistivity term splitting yields

$$\begin{aligned}\frac{c^2}{4\pi\mu}\nabla\times\eta\nabla\times\mathbf{B} &= \frac{c^2}{4\pi\mu}\{\frac{1}{r}\frac{\partial}{\partial\phi}[\frac{\eta}{r}\frac{\partial}{\partial r}(rB_\phi) - \frac{\eta}{r}\frac{\partial B_r}{\partial\phi}] - \frac{\partial}{\partial z}[\eta\frac{\partial B_r}{\partial z} - \eta\frac{\partial B_z}{\partial r}]\}\vec{e}_r \\ &+\frac{c^2}{4\pi\mu}\{\frac{\partial}{\partial z}[\frac{\eta}{r}\frac{\partial B_z}{\partial\phi} - \eta\frac{\partial B_\phi}{\partial z}] - \frac{\partial}{\partial r}[\frac{\eta}{r}\frac{\partial}{\partial r}(rB_\phi) - \frac{\eta}{r}\frac{\partial B_r}{\partial\phi}]\}\vec{e}_\phi \\ &+\frac{c^2}{4\pi\mu r}\{\frac{\partial}{\partial r}[\eta r\frac{\partial B_r}{\partial z} - \eta r\frac{\partial B_z}{\partial r}] - \frac{\partial}{\partial\phi}[\frac{\eta}{r}\frac{\partial B_z}{\partial\phi} - \eta\frac{\partial B_\phi}{\partial z}]\}\vec{e}_z.\end{aligned} \tag{4.19}$$

Then, we present the MHD equations for our Z-pinch DPP device. We assume that the plasma current is uniform along the ϕ direction. Meanwhile, it has a gradient in the r and z directions. Besides, in the ideal symmetric case, the magnetic field has only one ϕ-projection. Based on these assumptions, the final ideal MHD equation set for Z-pinch in cylindrical coordinate system is given as

$$\begin{cases}\dfrac{\partial\rho}{\partial t} + \dfrac{1}{r}\dfrac{\partial}{\partial r}(r\rho v_r) + \dfrac{1}{z}\dfrac{\partial}{\partial z}(\rho v_z) = 0, \\[2ex] \dfrac{\partial\rho v_r}{\partial t} + \dfrac{1}{r}\dfrac{\partial}{\partial r}r(\rho v_r v_r) + \dfrac{\partial}{\partial z}(\rho v_r v_z) + \dfrac{\partial p_{tot}}{\partial r} = -\dfrac{B_\phi B_\phi}{4\pi\mu r}, \\[2ex] \dfrac{\partial\rho v_z}{\partial t} + \dfrac{1}{r}\dfrac{\partial}{\partial r}r(\rho v_z v_r) + \dfrac{\partial}{\partial z}(\rho v_z v_z + p_{tot}) = 0, \\[2ex] \dfrac{\partial e_{tot}}{\partial t} + \dfrac{1}{r}\dfrac{\partial}{\partial r}\{(r[v_r(e_{tot}+p_{tot})] - \dfrac{c^2\eta B_\phi}{16\pi^2\mu^2}\dfrac{\partial(rB_\phi)}{\partial r}\} + \\[2ex] \dfrac{\partial}{\partial z}\{v_z[e_{tot}+p_{tot}] - \dfrac{c^2\eta B_\phi}{16\pi^2\mu^2}\dfrac{\partial B_\phi}{\partial r}\} = 0, \\[2ex] \dfrac{\partial B_\phi}{\partial t} + \dfrac{\partial}{\partial r}\{v_r B_\phi - \dfrac{c^2\eta}{4\pi\mu r}\dfrac{\partial rB_\phi}{\partial r}\} + \dfrac{\partial}{\partial z}\{v_z B_\phi - \dfrac{c^2\eta}{4\pi\mu}\dfrac{\partial B_\phi}{\partial z}\} = 0.\end{cases} \tag{4.20}$$

4.1.3 Non-convective Terms

In order to represent the energy exchange and main dissipative processes, it is essential to understand the transport processes, such as particle diffusion, heat conduction across the magnetic field, electric resistivity, etc. The complete description of a fully ionized plasma is rather complicated. When the plasma is close to equilibrium, macroscopic variables can be used to describe it. Additional non-convective terms can be represented in the right side of the conservation law equations or transformed to additional dissipative fluxes. Therefore Eq. (4.1) can be expanded to

$$\frac{\partial q}{\partial t} + \nabla \cdot (\mathbf{F}_q - \widetilde{\mathbf{F}}_q) = 0, \tag{4.21}$$

where $\widetilde{\mathbf{F}}_q$ is the dissipative flux. In this study, we mainly consider the heat transport and magnetic diffusion. The general MHD equation set taking into account these processes in Eq. (4.21) is given gy

$$\begin{cases} \dfrac{\partial \rho}{\partial t} + \nabla \cdot (\rho \mathbf{v}) = 0, \\[2ex] \dfrac{\partial (\rho \mathbf{v})}{\partial t} + \nabla \cdot (\rho \mathbf{v}\mathbf{v} + p_{tot} - \dfrac{\mathbf{B}\mathbf{B}}{4\pi\mu}) = -\dfrac{1}{4\pi\mu}\mathbf{B}(\nabla \cdot \mathbf{B}), \\[2ex] \dfrac{\partial e_{tot}}{\partial t} + \nabla \cdot [\mathbf{v}(e_{tot} + p_{tot}) - \dfrac{1}{4\pi\mu}[\mathbf{v} \cdot \mathbf{B}] \cdot \mathbf{B} + \dfrac{c^2\eta}{16\pi^2}\mu^2(\nabla \times \mathbf{B}) \times \mathbf{B} \\[2ex] -\lambda \nabla T - \mathbf{S}_{rad}] = -\dfrac{1}{4\pi\mu}(\mathbf{v} \cdot \mathbf{B}) \cdot \nabla \cdot \mathbf{B}, \\[2ex] \dfrac{\partial \mathbf{B}}{\partial t} + \nabla \cdot (\mathbf{v}\mathbf{B} - \mathbf{B}\mathbf{v}) + \dfrac{c^2}{4\pi\mu}\nabla \times (\eta \nabla \times \mathbf{B}) = -\mathbf{v}(\nabla \cdot \mathbf{B}). \end{cases} \tag{4.22}$$

where λ is thermal conductivity, η the resistivity, and S_{rad} the radiation flux. In current model, the re-absorption of emission due to opacity of plasma is not taken into account.

In general, the radiation transfer plays an important role in Z-pinch process, especially for the EUV radiation output[78]. However, in this study, we do not quantitatively calculate the 13.5 nm EUV emission; instead, we focus on the hydrodynamical process, for example, the MRT instability. K. T. Lee $et\ al.$ investigated the effect of opacity on the hydrodynamic parameters of a Z-pinch plasma, e.g., electron density and electron temperature[123]. The change of the imploding hydrodynamical properties due to opacity is not very obvious. In our case, the density is 1 or 2 order of magnitudes smaller than that of K. T. Lee's case, thus it is reasonable to neglect the opacity effect in the MHD model when we focus on the hydrodynamic processes.

The Eq. (4.21) and Eq. (4.22) are not fully hyperbolic because the dissipative flux $\widetilde{\mathbf{F}}_q$ adds "parabolicity" to the system. Direct use of convective hydrodynamic numerical schemes to Eq. (4.22) leads to nonphysical oscillations. Therefore a special splitting method involving decoupling the full model into a separate component for each process, employing specialized numerical methods to solve each component, and coupling the resulting solutions, is utilized for this problem[124]. We solve the MHD equations as a decoupled set of hyperbolic and parabolic equations. At each time step Eq. (4.22) is split into decoupled subproblems corresponding to the different physical processes occur within the computational domain or in individual regions.

4.1.4 Single-fluid Two-temperature Approximation

The MHD model constructed in previous section treats the plasma as a single fluid with one temperature. For actual plasma, the electrons and ions often have different temperatures. In a plasma, different particles collide with each other. The maximal energy that can be transmitted from one particle to another particle by elastic interaction is given by[125]

$$E_{max} = \frac{4m_1m_2}{(m_1+m_2)^2}E_1 = C_{tr}E_1 \tag{4.23}$$

where m_1 and E_1 are the mass and energy of the bullet particle, and m_2 is the mass of the recoil particle. For the equal particles, the transmission coefficients are ~ 1. While in case of the transmission between electron and ion, Xe$^+$ for example, the transmission coefficient is $\sim 10^{-5}$. Therefore energy transfer between the same particles is considerably higher; that is, the thermal energy will be transferred from the electrons to the ions with a time delay. As a result, electrons and ions usually have different temperature in Z-pinch EUV source. The Eq. (4.22) should be expanded to consider two gas species with different temperatures. Thus the governing MHD equations for the DPP device is given by

$$\begin{cases} \frac{\partial \rho}{\partial t} + \frac{1}{r}\frac{\partial (r\rho v_r)}{\partial r} + \frac{\partial (\rho v_z)}{\partial z} = 0, \\ \frac{\partial (\rho v_r)}{\partial t} + \frac{1}{r}\frac{\partial (r\rho v_r v_r)}{\partial r} + \frac{\partial p_{tot}}{\partial r} + \frac{\partial (\rho v_r v_z)}{\partial z} = -\frac{B^2}{4\pi r}, \\ \frac{\partial (\rho v_z)}{\partial t} + \frac{1}{r}\frac{\partial (r\rho v_z v_r)}{\partial r} + \frac{\partial ((\rho v_z v_z) + p_{tot})}{\partial z} = 0, \\ \frac{\partial E_e}{\partial t} + \frac{1}{r}\frac{\partial (r v_r (E_e + p_e))}{\partial r} + \frac{\partial (v_z (E_e + p_e))}{\partial z} = Q_j + Q_{th,e} \\ -Q_{brem} - Q_{ei} - Q_{atom}, \\ \frac{\partial E_i}{\partial t} + \frac{1}{r}\frac{\partial (r v_r (E_i + p_i))}{\partial r} + \frac{\partial (v_z (E_i + p_i))}{\partial z} = Q_{th,i} + Q_{ei}, \\ \frac{\partial \mathbf{B}}{\partial t} + \frac{\partial (v_r \mathbf{B})}{\partial r} + \frac{\partial (v_z \mathbf{B})}{\partial z} = -\frac{c^2}{4\pi}\nabla \times (\eta \nabla \times \mathbf{B}). \end{cases} \tag{4.24}$$

where ρ is the plasma density, v_r the velocity in the radial direction, and v_z the velocity in the axial direction. $p_{tot} = p_e + p_i + p_{mag}$ is the total pressure, $p_e = n_e k_B T_e$ the electron pressure, k_B the Boltzmann constant, $p_i = n_i k_B T_i$ the ion pressure, $p_{mag} = B^2/(8\pi)$ the magnetic pressure. $E_e = \frac{3}{2} n_e k_B T_e$ is the electron internal energy, $E_i = \frac{3}{2} n_i k_B T_i$ the ion internal energy. The Joule heating is

$$Q_j = \frac{c^2\eta}{16\pi^2}(\nabla \times \mathbf{B}) \times \mathbf{B}, \tag{4.25}$$

where η is the Spitzer resistivity[126]

$$\eta = \frac{1}{2}\sqrt{\frac{\pi^3 m_e}{8(k_B T_e)^3}} Z e^2 \ln\Lambda. \tag{4.26}$$

The electron or ion thermal diffusions are

$$Q_{th,e/i} = \nabla(\lambda_{e/i}\nabla T_{e/i}), \tag{4.27}$$

where $\lambda_{e/i}$ is the thermal conductivity of the electron or ion respectively. Q_{brem} is the energy loss through Bremsstrahlung radiation[126], Q_{ei} the electron-ion energy exchange [127]:

$$Q_{ei} = 3\frac{m_e n_e}{m_i \tau_e}(k_B T_e - k_B T_i). \tag{4.28}$$

where the time between electron interactions is

$$\tau_e = \frac{3\sqrt{m_e}(k_B T_e)^{3/2}}{4\sqrt{2\pi}e^4 Z^2 n_i \ln\Lambda}. \tag{4.29}$$

Q_{atom} is the energy loss in atomic processes, including collisional ionization, radiative recombination, and three-body recombination. In the magnetic induction equation, the time variation of the electric field is neglected[128].

The rate equation is given by[129]

$$\begin{aligned} \frac{dn_{Z+1}}{dt} &= n_e n_Z S(Z, Te) - n_e n_{Z+1}(S(Z+1, Te) \\ &\quad + \alpha_r(Z+1, Te) + n_e \alpha_{3b}(Z+1, Te)) \\ &\quad + n_e n_{Z+2}(\alpha_r(Z+2, Te) + n_e \alpha_{3b}(Z+2, Te)). \end{aligned} \tag{4.30}$$

where S is the collisional ionization rate coefficient:

$$S = \frac{9 \times 10^{-12} \xi_z \sqrt{T_e}}{E_z^2 (4.88 + \dfrac{T_e}{E_z})} \exp(-\frac{E_z}{T_e}) \text{ [eVm}^{-3}] \tag{4.31}$$

α_r is the radiative recombination rate coefficient:

$$\alpha_r = 5.2 \times 10^{-20} \sqrt{\frac{E_z}{T_e}} Z[0.429 + \frac{1}{2} \log(\frac{E_z}{T_e}) + 0.469 \sqrt{\frac{\sqrt{T_e}}{E_z}}] \text{ [eVm}^{-3}] \tag{4.32}$$

and α_{3b} is the three-body recombination rate coefficient:

$$\alpha_{3b} = \frac{2.97 \times 10^{-39} \xi_z}{E_z^2 T_e (4.88 + \dfrac{T_e}{E_z})} \text{ [eVm}^{-6}] \tag{4.33}$$

where E_z is the ionization potential, ξ_z the number of electrons in the outmost layer of the ion. By denoting $\dot{\rho}_j = m_i \dfrac{dn_j}{dt}$, for $j = 1, 2, \ldots, 18$, where ρ_j is the density for Xe^{j+}, the rate equations for ions from Xe^{1+} to Xe^{18+} can be incorporated into the MHD model. Thus the MHD equation set (4.24) can be rewritten as

$$
\begin{cases}
\dfrac{\partial \rho}{\partial t} + \dfrac{1}{r}\dfrac{\partial (r\rho v_r)}{\partial r} + \dfrac{\partial (\rho v_z)}{\partial z} = 0, \\[2ex]
\dfrac{\partial \rho_j}{\partial t} + \dfrac{1}{r}\dfrac{\partial (r\rho_j v_r)}{\partial r} + \dfrac{\partial (\rho_j v_z)}{\partial z} = \dot{\rho_j}, \ (\text{for j=1, 2, \ldots, 18}) \\[2ex]
\dfrac{\partial (\rho v_r)}{\partial t} + \dfrac{1}{r}\dfrac{\partial (r\rho v_r v_r)}{\partial r} + \dfrac{\partial p_{tot}}{\partial r} + \dfrac{\partial (\rho v_r v_z)}{\partial z} = -\dfrac{B^2}{4\pi r}, \\[2ex]
\dfrac{\partial (\rho v_z)}{\partial t} + \dfrac{1}{r}\dfrac{\partial (r\rho v_z v_r)}{\partial r} + \dfrac{\partial (\rho v_z v_z) + p_{tot}}{\partial z} = 0, \\[2ex]
\dfrac{\partial E_e}{\partial t} + \dfrac{1}{r}\dfrac{\partial (r v_r (E_e + p_e))}{\partial r} + \dfrac{\partial (v_z (E_e + p_e))}{\partial z} = Q_j + Q_{th,e} \\[2ex]
-Q_{brem} - Q_{ei} - Q_{atom}, \\[2ex]
\dfrac{\partial E_i}{\partial t} + \dfrac{1}{r}\dfrac{\partial (r v_r (E_i + p_i))}{\partial r} + \dfrac{\partial (v_z (E_i + p_i))}{\partial z} = Q_{th,i} + Q_{ei}, \\[2ex]
\dfrac{\partial \mathbf{B}}{\partial t} + \dfrac{\partial (v_r \mathbf{B})}{\partial r} + \dfrac{\partial (v_z \mathbf{B})}{\partial z} = -\dfrac{c^2}{4\pi}\nabla \times (\eta \nabla \times \mathbf{B}).
\end{cases}
\tag{4.34}
$$

Theoretically, the sum of Xe ion density ρ_j from the charge state of 1 to 18 should be equal to the plasma density ρ. However, the difference of them is not equal to 0 due to truncation errors or other numerical errors. Such difference can be used to control the error of the code, which will be discussed in the numerical scheme section.

In order to study the effect of axial magnetic field on MRT instabilities, the $\vec{e_r}$ and $\vec{e_z}$ components of magnetic field are incorporated into the governing equations. The momentum equations are also changed accordingly, thus the MHD equation set becomes

$$
\left\{
\begin{array}{l}
\dfrac{\partial \rho}{\partial t} + \dfrac{1}{r}\dfrac{\partial (r\rho v_r)}{\partial r} + \dfrac{\partial (\rho v_z)}{\partial z} = 0, \\[2ex]
\dfrac{\partial \rho_j}{\partial t} + \dfrac{1}{r}\dfrac{\partial (r\rho_j v_r)}{\partial r} + \dfrac{\partial (\rho_j v_z)}{\partial z} = \dot{\rho}_j, \text{ (for j=1, 2, \ldots, 18)} \\[2ex]
\dfrac{\partial (\rho v_r)}{\partial t} + \dfrac{1}{r}\dfrac{\partial}{\partial r}(r\rho v_r v_r - \dfrac{B_r B_r}{4\pi}) + \dfrac{\partial p_{tot}}{\partial r} + \dfrac{\partial}{\partial z}(\rho v_r v_z - \dfrac{B_r B_z}{4\pi}) = -\dfrac{B_\phi B_\phi}{4\pi r}, \\[2ex]
\dfrac{\partial (\rho v_z)}{\partial t} + \dfrac{1}{r}\dfrac{\partial}{\partial r}(r\rho v_z v_r - \dfrac{B_z B_r}{4\pi}) + \dfrac{\partial}{\partial z}(\rho v_z v_z + p_{tot} - \dfrac{B_z B_z}{4\pi}) = 0, \\[2ex]
\dfrac{\partial E_e}{\partial t} + \dfrac{1}{r}\dfrac{\partial (r v_r (E_e + p_e))}{\partial r} + \dfrac{\partial (v_z (E_e + p_e))}{\partial z} = Q_j + Q_{th,e} \\[2ex]
-Q_{brem} - Q_{ei} - Q_{atom}, \\[2ex]
\dfrac{\partial E_i}{\partial t} + \dfrac{1}{r}\dfrac{\partial (r v_r (E_i + p_i))}{\partial r} + \dfrac{\partial (v_z (E_i + p_i))}{\partial z} = Q_{th,i} + Q_{ei}, \\[2ex]
\dfrac{\partial B_r}{\partial t} + \dfrac{\partial (v_z B_r - B_z v_r)}{\partial z} = \dfrac{c^2}{4\pi}\{\dfrac{\partial}{\partial z}(\eta\dfrac{\partial B_r}{\partial z} - \eta\dfrac{\partial B_z}{\partial r})\}, \\[2ex]
\dfrac{\partial B_\phi}{\partial t} + \dfrac{1}{r}\dfrac{\partial}{\partial r}(r v_r B_\phi) + \dfrac{\partial v_z B_\phi}{\partial z} - \dfrac{B_\phi v_r}{r} = \dfrac{c^2}{4\pi}(\dfrac{\partial}{\partial z}(\eta\dfrac{\partial B_\phi}{\partial z}) + \dfrac{\partial}{\partial r}(\dfrac{\eta}{r}\dfrac{\partial r B_\phi}{\partial r})), \\[2ex]
\dfrac{\partial B_z}{\partial t} + \dfrac{1}{r}\dfrac{\partial}{\partial r}(r[v_r B_z - B_r v_z]) = -\dfrac{c^2}{4\pi r}\dfrac{\partial}{\partial r}(r\eta\dfrac{\partial B_r}{\partial z} - r\eta\dfrac{\partial B_z}{\partial r}).
\end{array}
\right.
\tag{4.35}
$$

4.2 Numerical Scheme

The governing equations (4.34) constructed in foregoing sections contain both hyperbolic part and diffusion part and should be treated separately. The diffusion terms are solved implicitly, while the hyperbolic governing equations are numerically solved by the Total Variation Diminishing (TVD) scheme[130]. As is well known, predictor-corrector schemes are unstable and need the addition of an energy dissipation mechanism at the front of the shock waves[131]. It can be artificial diffusion, viscosity, etc. The coefficients of the mechanism can be tuned to get better results, but that problem-dependent approach is not in the spirit of modern shock-capturing schemes. The TVD method is a particular case of essentially non-oscillatory schemes. There is no generation of nonphysical oscillations along the shock waves in these solutions. The scheme can solve shock waves within 2-4 cells. In the TVD scheme, a nonlinear numerical limiter is devised to switch the spatial discretization between a monotonic scheme that satisfies the entropy condition and a high-order scheme. This switching eliminate spurious numerical oscillations in the presence of discontinuities while retaining the high order accuracy for smooth solutions. For the hyperbolic flux function, we make use of Lax-Friedrich (LF) splitting[132], which is one of the most robust approximate Riemann solvers for hyperbolic systems. The TVD-LF scheme has been demonstrated to be accurate and efficient for MHD problems[133].The diffusion terms are treated separately to ensure the stability of the calculation. The derivation of the time step for the MHD problem was determined by the Courant-Friedrich-Lewy (CFL) condition given by G. Toth $et\ al.$[134], and is mainly restricted by the plasma diffusion time scale rather than the convection-dominated processes of fluid dynamics.

4.2.1 Treatment of Diffusion Terms

Heat conduction is one of the most important physical processes that should be taken into account when modeling the DPP plasma. Energy redistribution plays a significant role in the thermal conditions of real plasma devices. Decoupled from Eq. (4.34), the heat conduction equation reads

$$\frac{\partial e}{\partial t} - \nabla(\lambda \nabla T) = 0. \tag{4.36}$$

The heat conduction equation in cylindrical coordinates reads

$$\frac{\partial}{\partial t}(\rho c_p T(t,r,z)) - \frac{\partial}{\partial r}(r\lambda\frac{\partial}{\partial r}T(t,r,z)) - \frac{\partial}{\partial z}(\lambda\frac{\partial}{\partial z}T(t,r,z)) = 0. \tag{4.37}$$

The plasma properties are assumed to be constant during each time step. This assumption allows us to consider the first term in Eq. (4.37) as a constant source, like Poisson's equation. The finite-difference approximations for the derivation construction replacements in the r direction reads

$$[\frac{\partial}{\partial r}(r\lambda\frac{\partial}{\partial r}T(t,r,z))]_{i,j} = C_1^r T_{i-1,j} + C_2^r T_{i,j} + C_3^r T_{i+1,j}$$

where

$$\begin{cases} C_1^r = \dfrac{2\lambda_{i-1/2,j} r_{i-1/2}}{r_i \Delta r_i(\Delta r_{i-1} + \Delta r_i)}, \\ \\ C_2^r = -[\dfrac{2\lambda_{i-1/2,j} r_{i-1/2}}{r_i \Delta r_i(\Delta r_{i-1} + \Delta r_i)} + \dfrac{2\lambda_{i+1/2,j} r_{i+1/2}}{r_i \Delta r_i(\Delta r_{i+1} + \Delta r_i)}], \\ \\ C_3^r = \dfrac{2\lambda_{i+1/2,j} r_{i+1/2}}{r_i \Delta r_i(\Delta r_{i+1} + \Delta r_i)}. \end{cases}$$

Plasma properties on the cell borders are calculated by linear interpolation. Derivation in the z direction is given by

$$[\frac{\partial}{\partial z}(\lambda\frac{\partial}{\partial z}T(t,r,z))]_{i,j} = C_1^z T_{i,j-1} + C_2^z T_{i,j} + C_3^z T_{i,j+1},$$

where

$$\begin{cases} C_1^z = \dfrac{2\lambda_{i,j-1/2}}{\Delta z_j(\Delta z_{j-1} + \Delta z_i)}, \\ \\ C_2^z = -[\dfrac{2\lambda_{i,j-1/2}}{\Delta z_j(\Delta z_{j-1} + \Delta z_i)} + \dfrac{2\lambda_{i,j+1/2}}{\Delta z_j(\Delta z_{j+1} + \Delta z_i)}], \\ \\ C_3^z = \dfrac{2\lambda_{i,j+1/2}}{\Delta z_j(\Delta z_{j+1} + \Delta z_i)}. \end{cases}$$

Therefore the heat conduction equation can be presented as a set of linear equations, where the total number of equations is equivalent to the total number of useful cells in the computational domain.

$$A_{i-1,j}T_{i-1,j}^{n+1} + A_{i,j}T_{i,j}^{n+1} + A_{i+1,j}T_{i+1,j}^{n+1} + A_{i,j-1}T_{i,j-1}^{n+1} + A_{i,j+1}T_{i,j+1}^{n+1} = D_{i,j} \quad (4.38)$$

where

$$A_{i-1,j} = C_1^r,\ A_{i,j} = C_2^r + C_2^z - \frac{c_{p(i,j)}^n \rho_{i,j}^n}{\Delta t^n},\ A_{i+1,j} = C_3^r,\ A_{i,j-1} = C_1^z,$$

$$A_{i,j+1} = C_3^z,\ D_{i,j} = -\frac{c_{p(i,j)}^n \rho_{i,j}^n T_{i,j}^n}{\Delta t^n}.$$

Numerical simulation with the implicit scheme is unconditionally stable, and by using combined schemes, the limiting factor on the time step is usually the explicit part.

Decoupled from Eq. 4.34, the magnetic conduction equation reads

$$\frac{\partial \mathbf{B}}{\partial t} + \frac{c^2}{4\pi\mu}\nabla \times (\eta\nabla \times \mathbf{B}) = 0 \quad (4.39)$$

The magnetic diffusion equation in cylindrical coordinates reads

$$\frac{\partial}{\partial t}(B(t,r,z)) - \frac{\partial}{\partial r}\frac{c^2\eta}{4\pi r}\frac{\partial}{\partial r}(rB(t,r,z)) - \frac{\partial}{\partial z}\frac{c^2\eta}{4\pi}\frac{\partial}{\partial z}B(t,r,z) = 0. \tag{4.40}$$

The magnetic diffusion equation has several exceptions in the finite-difference scheme. One concerns the behavior of mesh function near the r zero point. An implicit numerical method is used to solving the discontinuity at the zero point.

The second term is given by

$$[\frac{\partial}{\partial r}\frac{\eta}{r}\frac{\partial}{\partial r}rB(t,r,z)]_{i,j} = C_1^r B_{i-1,j} + C_2^r B_{i,j} + C_3^r B_{i+1,j}$$

where

$$\begin{cases} C_1^r = \dfrac{2\eta_{i-1/2,j} r_{i-1}}{r_{i-1/2}\Delta r_i(\Delta r_{i-1} + \Delta r_i)}, \\ \\ C_2^r = -[\dfrac{2\eta_{i-1/2,j} r_i}{r_{i-1/2}\Delta r_i(\Delta r_{i-1} + \Delta r_i)} + \dfrac{2\eta_{i+1/2,j} r_i}{r_{i+1/2}\Delta r_i(\Delta r_i + \Delta r_{i+1})}], \\ \\ C_3^r = \dfrac{2\eta_{i+1/2,j} r_{i+1}}{r_{i+1/2}\Delta r_i(\Delta r_i + \Delta r_{i+1})}, \text{for } r_{i-1/2} \neq 0, \text{ i.e.}, i > 1. \end{cases}$$

For the singularity point where r=0 and $B|_{r=0} = 0$, we have

$$\frac{\partial B}{\partial r}|_+ = \frac{\partial B}{\partial r}|_-,$$

$$\lim_{r\to 0}\frac{c^2\eta}{4\pi\mu r}\frac{\partial rB}{\partial r} = \frac{c^2\eta}{2\pi\mu}\lim_{r\to 0}\frac{\partial B}{\partial r}$$

Thus

$$\begin{cases} C_1^r = 0, \\ \\ C_2^r = -[\dfrac{2\eta_{3/2,j} r_2}{r_{3/2}\Delta r_1(\Delta r_1 + \Delta r_2)} + \dfrac{4\eta_{1/2,j}}{\Delta r_1^2}], \\ \\ C_3^r = \dfrac{2\eta_{3/2,j} r_2}{r_{3/2}\Delta r_1(\Delta r_1 + \Delta r_2)}, \text{ for } i = 1. \end{cases}$$

The z axis term in the magnetic diffusion equation has no exclusions and can be derived similarly to heat conduction:

$$[\frac{\partial}{\partial z}\eta\frac{\partial}{\partial z}B(t,r,z)]_{i,j} = C_1^z B_{i,j-1} + C_2^z B_{i,j} + C_3^z B_{i,j+1}$$

where

$$\begin{cases} C_1^z = \dfrac{2\eta_{i,j-1/2}}{\Delta z_j(\Delta z_{j-1} + \Delta z_i)}, \\ \\ C_2^z = -[\dfrac{2\eta_{i,j-1/2}}{\Delta z_j(\Delta z_{j-1} + \Delta z_i)} + \dfrac{2\eta_{i,j+1/2}}{\Delta z_j(\Delta z_{j+1} + \Delta z_i)}], \\ \\ C_3^z = \dfrac{2\eta_{i,j+1/2}}{\Delta z_j(\Delta z_{j+1} + \Delta z_i)}. \end{cases}$$

Finally, after transformations, the magnetic diffusion equation (4.40) can be represented as a linear equation system:

$$A_{i-1,j}B_{i-1,j}^{n+1} + A_{i,j}B_{i,j}^{n+1} + A_{i+1,j}B_{i+1,j}^{n+1} + A_{i,j-1}B_{i,j-1}^{n+1} + A_{i,j+1}B_{i,j+1}^{n+1} = D_{i,j} \quad (4.41)$$

where coefficients A and D are given as

$$A_{i-1,j} = C_1^r,\ A_{i,j} = C_2^r + C_2^z - \frac{4\pi\mu}{\Delta t^n c^2},\ A_{i+1,j} = C_3^r,\ A_{i,j-1} = C_1^z,$$

$$A_{i,j+1} = C_3^z,\ D_{i,j} = -\frac{4\pi\mu B_{i,j}^n}{\Delta t^n c^2}.$$

The time steps for implicit magnetic diffusion algorithms is given in Ref. [134]. Finally, the heat conduction equation (4.38) and magnetic diffusion equation (4.41) can be expressed uniformly in matrix form as

$$\mathbf{A}\cdot\mathbf{X} = \mathbf{D} \tag{4.42}$$

where **A** and **D** are matrixes of coefficients A and D, and **X** is a matrix of unknown field (T or B). The matrix expression for the diffusion equations in the $n \times m$ domain where zero elements are indicated is given by

$$\begin{bmatrix}
A_{1,1} & A_{2,1} & 0 & 0 & \dots & A_{1,2} & 0 & 0 & 0 & 0 & 0 \\
A_{1,1} & A_{2,1} & A_{3,1} & 0 & \dots & 0 & A_{2,2} & 0 & 0 & 0 & 0 \\
0 & A_{2,1} & A_{3,1} & A_{4,1} & \dots & 0 & 0 & A_{3,1} & 0 & 0 & 0 \\
\dots & \dots & \dots & \dots & \dots & \dots & \dots & \dots & \dots & \dots & \dots \\
0 & \dots & A_{i,j-1} & \dots & A_{i-1,j} & A_{i,j} & A_{i+1,j} & \dots & A_{i,j+1} & \dots & 0 \\
\dots & \dots & \dots & \dots & \dots & \dots & \dots & \dots & \dots & \dots & \dots \\
0 & 0 & 0 & A_{n-2,m-1} & 0 & 0 & \dots & A_{n-3,m} & A_{n-2,m} & A_{n-1,m} & 0 \\
0 & 0 & 0 & 0 & A_{n-1,m-1} & 0 & \dots & 0 & A_{n-2,m} & A_{n-1,m} & A_{n,m} \\
0 & 0 & 0 & 0 & 0 & A_{n,m-1} & \dots & 0 & A_{n-2,m} & A_{n-1,m} & A_{n,m}
\end{bmatrix}$$

$$\times \begin{bmatrix} T_{1,1}^{n+1} \\ \dots \\ T_{n,1}^{n+1} \\ T_{1,2}^{n+1} \\ \dots \\ T_{n,2}^{n+1} \\ \dots \\ T_{1,m}^{n+1} \\ \dots \\ T_{n,m}^{n+1} \end{bmatrix} = \begin{bmatrix} D_{1,1} \\ \dots \\ D_{n,1} \\ D_{1,2} \\ \dots \\ D_{n,2} \\ \dots \\ D_{1,m} \\ \dots \\ D_{n,m} \end{bmatrix} \tag{4.43}$$

This large sparse matrix has an extremely large number of zero elements. Key to computational efficiency is to store and operate on only nonzero entries of the matrix. By solving the sparse matrix equation system, we can get the magnetic induction and heat conduction terms.

4.2.2 TVD-LF Scheme

The full MHD equations set (4.34) can be represented in matrix form as

$$\frac{\partial \mathbf{U}}{\partial t} + \frac{1}{r}\frac{\partial r\mathbf{F(U)}}{\partial r} + \frac{\partial \mathbf{P(U)}}{\partial r} + \frac{\partial \mathbf{G(U)}}{\partial z} = \mathbf{\Omega} \tag{4.44}$$

where

$$\mathbf{U} = \begin{bmatrix} \rho \\ \rho_1 \\ \vdots \\ \rho_{18} \\ \rho v_r \\ \rho v_z \\ E_e \\ E_i \\ B \end{bmatrix}, \quad \mathbf{F}(\mathbf{U}) = \begin{bmatrix} \rho v_r \\ \rho_1 v_r \\ \vdots \\ \rho_{18} v_r \\ \rho v_r v_r \\ \rho v_z v_r \\ v_r(E_e + p_e) \\ v_r(E_i + p_i) \\ 0 \end{bmatrix}, \quad \mathbf{P}(\mathbf{U}) = \begin{bmatrix} 0 \\ 0 \\ \vdots \\ 0 \\ p_{tot} \\ 0 \\ 0 \\ 0 \\ v_r B \end{bmatrix},$$

$$\mathbf{G}(\mathbf{U}) = \begin{bmatrix} \rho v_z \\ \rho_1 v_z \\ \vdots \\ \rho_{18} v_z \\ \rho v_r v_z \\ \rho v_z v_z + p_{tot} \\ v_z(E_e + p_e) \\ v_z(E_i + p_i) \\ v_z B \end{bmatrix},$$

$$\mathbf{\Omega}(\mathbf{U}) = \begin{bmatrix} 0 \\ 0 \\ \vdots \\ 0 \\ -\frac{B^2}{4\pi r} \\ 0 \\ Q_j + Q_{th,e} - Q_{brem} - Q_{ei} - Q_{atom} \\ Q_{ei} + Q_{th,i} \\ Q_{diff} \end{bmatrix},$$

here $p_{tot} = p_e + p_i + p_{mag}$ is the total pressure, p_e the electron pressure, p_i the ion pressure, and $p_{mag} = B^2/8\pi$ the magnetic pressure.

$$Q_j = \frac{c^2\eta}{16\pi^2}[\frac{1}{r^2}(\frac{\partial rB}{\partial r})^2 + (\frac{\partial B}{\partial z})^2]$$

is the Joule heating. $Q_{th,e/i}$ is the heat conduction terms of electrons and ions respectively, Q_{brem} the Bremsstrahlung radiation, Q_{ei} the electron-ion energy interchange, Q_{atom} the energy loss during atomic processes, including ionization, radiactive recombination, and three-body recombination.

$$Q_{diff} = \frac{c^2}{4\pi\mu}\nabla \times (\eta\nabla \times \mathbf{B})$$

is the magnetic diffusion term.

In the TVD-LF scheme, a predictor at time step of n+1/2 is first calculated, which is

$$\mathbf{U}_{i,j}^{n+1/2} = \mathbf{U}_{i,j}^{n} - \frac{\Delta t^n}{2r_i\Delta r_i}[r_{i+1/2}\mathbf{F}(\mathbf{U}_{i+1/2,j}^{nL}) - r_{i-1/2}\mathbf{F}(\mathbf{U}_{i-1/2,j}^{nR})] - \frac{\Delta t^n}{2\Delta r_i}\cdot \tag{4.45}$$

$$[\mathbf{P}(\mathbf{U}_{i+1/2,j}^{nL}) - \mathbf{P}(\mathbf{U}_{i-1/2,j}^{nR})] - \frac{\Delta t^n}{2\Delta z_j}[\mathbf{G}(\mathbf{U}_{i,j+1/2}^{nL}) - \mathbf{G}(\mathbf{U}_{i,j-1/2}^{nR})] + \frac{\Delta t^n}{2}\mathbf{\Omega}_{i,j}$$

where

$$\begin{cases} \mathbf{U}^{nL}_{i+1/2,j} = \mathbf{U}^{n}_{i,j} + \dfrac{1}{2}\overline{\Delta\mathbf{U}^{r}_{i,j}} \\ \\ \mathbf{U}^{nR}_{i-1/2,j} = \mathbf{U}^{n}_{i,j} - \dfrac{1}{2}\overline{\Delta\mathbf{U}^{r}_{i,j}} \\ \\ \mathbf{U}^{nL}_{i,j+1/2} = \mathbf{U}^{n}_{i,j} + \dfrac{1}{2}\overline{\Delta\mathbf{U}^{z}_{i,j}} \\ \\ \mathbf{U}^{nR}_{i,j-1/2} = \mathbf{U}^{n}_{i,j} - \dfrac{1}{2}\overline{\Delta\mathbf{U}^{z}_{i,j}} \end{cases}$$

with the definition of

$$\begin{cases} \overline{\Delta\mathbf{U}^{r}_{i,j}} = \text{min mod}(\Delta\mathbf{U}^{n}_{i-1/2,j}, \Delta\mathbf{U}^{n}_{i+1/2,j}) \\ \\ \overline{\Delta\mathbf{U}^{z}_{i,j}} = \text{min mod}(\Delta\mathbf{U}^{n}_{i,j-1/2}, \Delta\mathbf{U}^{n}_{i,j+1/2}) \end{cases}$$

where

$$\text{min mod}(x, y) = \text{sgn}(x)\text{max}[0, \text{min}(|x|, \text{sgn}(x)y)]$$

$$\begin{cases} \Delta\mathbf{U}^{n}_{i-1/2,j} = \mathbf{U}^{n}_{i,j} - \mathbf{U}^{n}_{i-1,j} \\ \\ \Delta\mathbf{U}^{n}_{i+1/2,j} = \mathbf{U}^{n}_{i+1,j} - \mathbf{U}^{n}_{i,j} \\ \\ \Delta\mathbf{U}^{n}_{i,j-1/2} = \mathbf{U}^{n}_{i,j} - \mathbf{U}^{n}_{i,j-1} \\ \\ \Delta\mathbf{U}^{n}_{i,j+1/2} = \mathbf{U}^{n}_{i,j+1} - \mathbf{U}^{n}_{i,j} \end{cases}$$

The corrector for a time step of n+1 is evaluated with the quantities at n+1/2 obtained from Eq. (4.45).

$$\mathbf{U}^{n+1}_{i,j} = \mathbf{U}^{n}_{i,j} - \frac{\Delta t^n}{r_i \Delta r_i}[r_{i+1/2}\mathbf{F}(\mathbf{U}^{LR}_{i+1/2,j}) - r_{i-1/2}\mathbf{F}(\mathbf{U}^{LR}_{i-1/2,j})] - \frac{\Delta t^n}{\Delta r_i}\cdot \tag{4.46}$$

$$[\mathbf{P}(\mathbf{U}^{LR}_{i+1/2,j}) - \mathbf{P}(\mathbf{U}^{LR}_{i-1/2,j})] - \frac{\Delta t^n}{\Delta z_j}[\mathbf{G}(\mathbf{U}^{LR}_{i,j+1/2}) - \mathbf{G}(\mathbf{U}^{LR}_{i,j-1/2})] + \Delta t^n \mathbf{\Omega}_{i,j}$$

where

$$\begin{cases} \mathbf{P}(\mathbf{U}^{LR}_{i\pm1/2,j}) = \dfrac{1}{2}(\mathbf{P}(\mathbf{U}^{L}_{i\pm1/2,j}) + \mathbf{P}(\mathbf{U}^{R}_{i\pm1/2,j})) \\[2ex] \mathbf{F}(\mathbf{U}^{LR}_{i\pm1/2,j}) = \dfrac{1}{2}(\mathbf{F}(\mathbf{U}^{L}_{i\pm1/2,j}) + \mathbf{F}(\mathbf{U}^{R}_{i\pm1/2,j}) - c^{LR}_{i\pm1/2,j}\Delta\mathbf{U}^{LR}_{i\pm1/2,j}) \\[2ex] \mathbf{G}(\mathbf{U}^{LR}_{i,j\pm1/2}) = \dfrac{1}{2}(\mathbf{G}(\mathbf{U}^{L}_{i\pm1/2,j}) + \mathbf{G}(\mathbf{U}^{R}_{i,j\pm1/2}) - c^{LR}_{i,j\pm1/2}\Delta\mathbf{U}^{LR}_{i,j\pm1/2}) \end{cases}$$

The $c^{LR}_{i\pm1/2,j}\Delta\mathbf{U}^{LR}_{i\pm1/2,j}$ and $c^{LR}_{i\pm1/2,j}\Delta\mathbf{U}^{LR}_{i\pm1/2,j}$ are TVD corrections. Main fluxes are an average of left and right fluxes on any cell interface $\mathbf{F}(\mathbf{U}^{LR}_{i\pm1/2,j}) = \frac{1}{2}(\mathbf{F}(\mathbf{U}^{L}_{i\pm1/2,j}) + \mathbf{F}(\mathbf{U}^{R}_{i\pm1/2,j}))$ and $\mathbf{G}(\mathbf{U}^{LR}_{i,j\pm1/2}) = \frac{1}{2}(\mathbf{G}(\mathbf{U}^{L}_{i\pm1/2,j}) + \mathbf{G}(\mathbf{U}^{R}_{i,j\pm1/2}))$. The correction term is based on the concept of the maximum propagation speed c^{max}_x of information in direction x. In the case of hydrodynamics it is the speed of sound, v_{ac}. The MHD case also takes into account speed of Alfven wave[133, 136].

With the definition of

$$\begin{cases}
\mathbf{U}^L_{i+1/2,j} = \mathbf{U}^{n+1/2}_{i,j} + \dfrac{1}{2}\overline{\Delta\mathbf{U}^r_{i,j}} \\[2ex]
\mathbf{U}^L_{i-1/2,j} = \mathbf{U}^{n+1/2}_{i-1,j} + \dfrac{1}{2}\overline{\Delta\mathbf{U}^r_{i-1,j}} \\[2ex]
\mathbf{U}^R_{i+1/2,j} = \mathbf{U}^{n+1/2}_{i+1,j} - \dfrac{1}{2}\overline{\Delta\mathbf{U}^r_{i+1,j}} \\[2ex]
\mathbf{U}^R_{i-1/2,j} = \mathbf{U}^{n+1/2}_{i,j} - \dfrac{1}{2}\overline{\Delta\mathbf{U}^r_{i,j}} \\[2ex]
\mathbf{U}^L_{i,j+1/2} = \mathbf{U}^{n+1/2}_{i,j} + \dfrac{1}{2}\overline{\Delta\mathbf{U}^z_{i,j}} \\[2ex]
\mathbf{U}^L_{i,j-1/2} = \mathbf{U}^{n+1/2}_{i,j-1} + \dfrac{1}{2}\overline{\Delta\mathbf{U}^z_{i,j-1}} \\[2ex]
\mathbf{U}^R_{i,j+1/2} = \mathbf{U}^{n+1/2}_{i,j+1} - \dfrac{1}{2}\overline{\Delta\mathbf{U}^z_{i,j+1}} \\[2ex]
\mathbf{U}^R_{i,j-1/2} = \mathbf{U}^{n+1/2}_{i,j} - \dfrac{1}{2}\overline{\Delta\mathbf{U}^z_{i,j}}.
\end{cases}$$

We have

$$\begin{cases} \mathbf{U}^{LR}_{i\pm1/2,j} = \dfrac{1}{2}(\mathbf{U}^{L}_{i\pm1/2,j} + \mathbf{U}^{R}_{i\pm1/2,j}) \\ \\ \mathbf{U}^{LR}_{i,j\pm1/2} = \dfrac{1}{2}(\mathbf{U}^{L}_{i,j\pm1/2} + \mathbf{U}^{R}_{i,j\pm1/2}) \\ \\ \Delta\mathbf{U}^{LR}_{i\pm1/2,j} = \mathbf{U}^{R}_{i\pm1/2,j} - \mathbf{U}^{L}_{i\pm1/2,j} \\ \\ \Delta\mathbf{U}^{LR}_{i,j\pm1/2} = \mathbf{U}^{R}_{i,j\pm1/2} - \mathbf{U}^{L}_{i,j\pm1/2} \\ \\ c^{LR}_{i\pm1/2,j} = |v^{LR}_{r\{i\pm1/2,j\}}| + \sqrt{\dfrac{\gamma p^{LR}_{i\pm1/2,j}}{\rho^{LR}_{i\pm1/2,j}}} \\ \\ c^{LR}_{i,j\pm1/2} = |v^{LR}_{z\{i,j\pm1/2\}}| + \sqrt{\dfrac{\gamma p^{LR}_{i,j\pm1/2}}{\rho^{LR}_{i,j\pm1/2}}} \end{cases}$$

where γ is the ratio of specific heats. Therefore we can derive $\mathbf{U}^{n+1}$ from $\mathbf{U}^{n}$. Given the initial and boundary conditions, the MHD equation system (4.34) can be solved numerically.

In actual calculation, the truncation error exists; in addition, the time step might be too big for the rate equation. Therefore error control is needed to ensure the accuracy of the computation. We define a parameter

$$\varepsilon = \max(|\frac{\rho - \sum\limits_{k=1}^{18} \rho_k}{\rho}|_{i,j}) \tag{4.47}$$

which indicates the maximum relative density error of all the cells (i, j) in the computational domain. To ensure the convergence, the condition that

$$\varepsilon < 10^{-6} \tag{4.48}$$

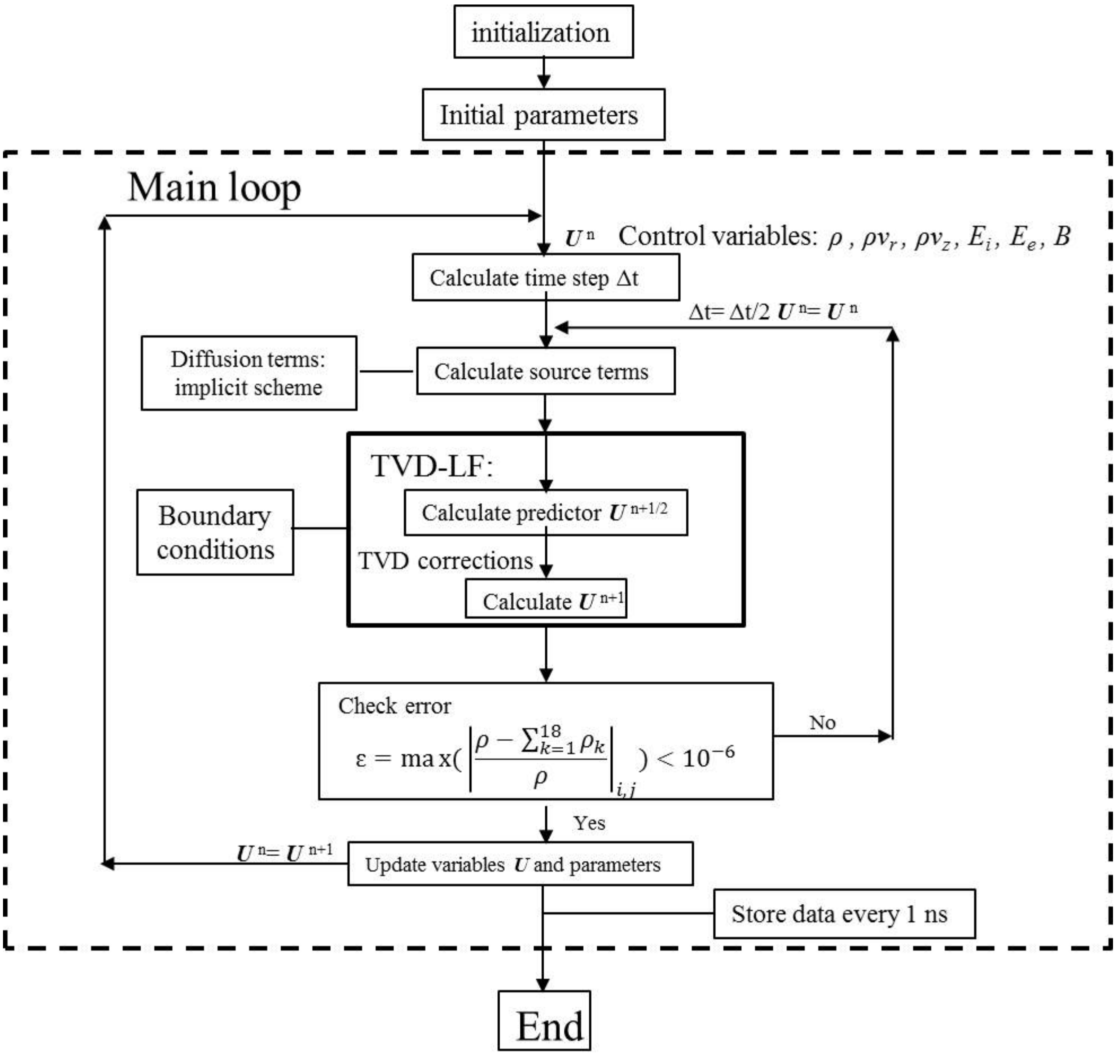

FIGURE 4.1: Flow charter of the MHD code computational process

is imposed in each time step. The computational process flow chart is shown in Fig. 4.1. The first step is the initialization of the code. The initial variables, such as n_e, T_e, are input into the code. Then the initial physical parameters (thermal conductivity, resistivity, ionization coefficient, etc.) are calculated. In the main loop, based on the variables and parameters of previous time step t^n, the time step Δt is calculated; then the source terms, including heat conduction, magnetic diffusion, etc., are also calculated. After that, the code comes to the TVD-LF subroutine. In this subroutine, a predictor $\mathrm{U}^{n+1/2}$ is first calculated; and then the control variables U^{n+1} at the time step of $n+1$ is calculated based on the predictor. Then the error of the calculation is checked. If the condition (4.48) is not satisfied, the code will return and recalculate the source term with $\Delta t = \Delta t/2$, and run the main loop again until it is satisfied. If the condition (4.48) is satisfied, all the control variables are updated. Then physical parameters are also updated based on the new control variables. For example, the current density is calculated from the control variable $\mathbf{B}$ through Eq.(4.6). Data is stored in files for post processing. Then the main loop goes to next time step.

4.3 Summary

In this chapter, the physical model was developed for the simulation of the main processes that occur in Z-pinch gas discharge of a DPP EUV source: MHD model of the plasma motion, theoretical models of the magnetic diffusion, and thermal conduction in plasma. Atomic processes, including collisional ionization, radiactive recombination, and three-body recombination are taken into account. The single-fluid two-temperature approximation was assumed to be valid in the MHD model. Thus energy equation was split into two: one for ions and one for electrons. The governing equations were written in axisymmetric cylindrical coordinate. An algorithm based on separation of different physical processes was developed. For each physical process, the most efficient numerical scheme was constructed. Hydrodynamic processes were solved based on an essentially non-oscillatory schemes called TVD-LF; an implicit scheme with the sparse matrix solver was adopted for solving linear equations of magnetic diffusion and heat conduction. The TVD-LF scheme had certain advantages, including simple to code, good computation speed, and robust. In terms of the larger sparse matrix solver, only nonzero entries of the matrix was stored and operated it is a high efficient method.

Chapter 5

Simulation of Plasma Behaviors in Z-pinch

In Z-pinch, the radial implosion is the dominant movement while the axial flow is relatively weak. Therefore the simulation reported here is restricted to initial uniform plasma instead of actual plasma jet with density gradient in z direction. There are two main purposes in this chapter. The first one is to numerically study the plasma dynamics for ideal Z-pinch (without perturbation), and find preferred initial conditions for the EUV source. The second one is to quantitatively study the characteristics of MRT instabilities and try to mitigate them, in order to optimize the EUV source. In Sec. 5.1, the plasma structure, important parameters' evolutions (Te, Ti, Ne, Ni) are present. Then the influences of initial density and current rise time on plasma dynamics and pinch stagnation states (such as Te and Ne at stagnation) are studied; preferred initial conditions are proposed. In Sec. 5.2, the MRT instabilities are comprehensively studied. The evolutions of MRT with various kinds of perturbations (single mode, multi-mode, and random mode) are investigated. The growth rate of MRT and its dependences on wavelengths are clarified. The experimentally observed dominant mm-scale MRT wavelength 1 mm is explained. The influences of MRT on pinch stagnation states are discussed. Three possible ways to suppress the MRT instabilities are discussed in detail, including RF pre-ionization, axial magnetic field, and shorter rise time of the current pulse.

5.1 Plasma Evolution without Initial Perturbation

In this section, we analyze the pinch evolution in a uniform density distribution without initial perturbation. We assume that the initial distribution of the plasma is uniform and in Local Thermodynamic Equilibrium (LTE). This simplification is sufficient for the essentials of Z-pinch dynamics to be grasped. The initial Xe ion density is assumed to be a uniform, and the initial electron and ion temperatures $T_e = T_i$ =1 eV. Under such circumstance, the number density of Xe^{2+} or higher charge states is negligible compared with Xe^{1+}. The initial radius is assumed to be 3 mm, estimated from the visible region plasma imaging experiment.

Due to axial symmetry, the boundary conditions on axis (r =0) are

$$\frac{\partial T_i}{\partial r} = \frac{\partial T_e}{\partial r} = 0,$$

$$B = 0,\ v_r = 0,$$

$$\frac{\partial v_z}{\partial r} = 0.$$

On the outer boundary ($r = r_0$), the magnetic field is given as

$$B = \frac{2I}{r_0 \cdot c}$$

where the current waveform is $I = I_0 sin(\omega_0 t)$, here I_0 =22 kA and $\omega_0 = 1 \times 10^7$ rad s^{-1}.

$$\frac{\partial v_r}{\partial r} = \frac{\partial v_z}{\partial r} = 0,$$

$$T_e = T_i = \text{const.}$$

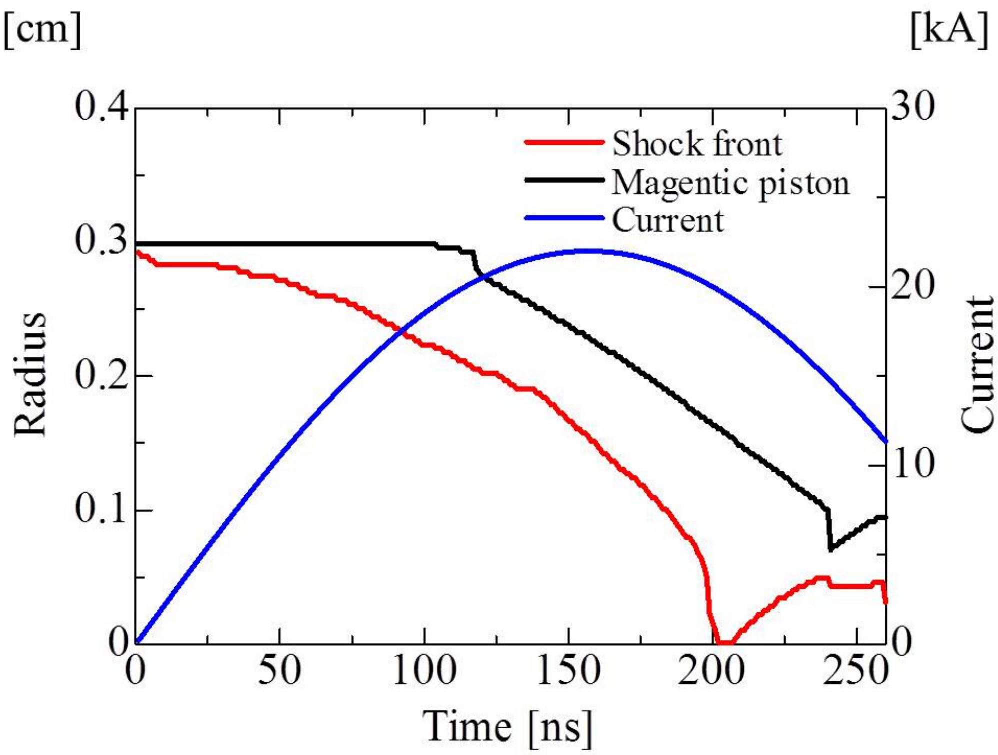

FIGURE 5.1: Position of shock front (r_s), magnetic piston (r_p) as a function of time without initial perturbation.

On both ends of z axis, namely $z = z_0$ and $z = z_t$, the boundary conditions are

$$\frac{\partial T_i}{\partial z} = \frac{\partial T_e}{\partial z} = 0,$$

$$\frac{\partial B}{\partial z} = 0,$$

$$\frac{\partial v_r}{\partial z} = \frac{\partial v_z}{\partial z} = 0.$$

5.1.1 Z-pinch Dynamics without Initial Perturbation

We denote the position of the shock front, r_s, to be at the ion density maximum and the magnetic piston position, r_p, to be at the magnetic field maximum. Fig. 5.1 shows r_s and r_p as a function of time without initial perturbation. During the implosion phase, the magnetic field pushes on the plasma and starts to form a high density layer, as in the snowplow effect. The plasma shell becomes denser as it accumulates, and also obtains kinetic energy through $\mathbf{J} \times \mathbf{B}$. However, the pressure prevents the density from becoming too high. Instead a shock forms ahead of the magnetic field. The shock front reaches the Z axis at 203 ns, ahead of the magnetic piston. This moment is the beginning of pinch stagnation. The shock front reflects at about 210 ns, having stagnated on the axis for several nanoseconds, while the magnetic piston continues to compress the plasma. At 241 ns, the shock front again turns back toward the axis. There is an abrupt decrease of r_p near 240 ns shown in the figure. This is because r_p is defined as the maximum magnetic field position and is thus particularly sensitive to the magnetic field radial profile. Fig. 5.2 shows the radial profile of (a) ion temperature, (b) electron temperature, (c) ion density, and (d) current density during implosion when at t=150 ns. During the implosion phase, a shock wave is formed ahead of magnetic piston, heating the ions, as shown in Fig. 5.2(a) and Fig. 5.2(c). In stead, the electrons are mainly heated by Joule heating, as shown in Fig. 5.2(b) and Fig. 5.2(d). The shell thickness, which is defined as the FWHM of the peak density, is on the order of 1 mm, which is important for later discussion.

Fig. 5.3 shows the electron temperature, electron density, ion temperature and ion density on axis as a function of time without initial perturbation. The electron and ion temperatures increase significantly immediately before stagnation, as is shown in Fig. 5.3(a). This is due to the combined effect of adiabatic heating and energy transfer from kinetic to internal energy. During pinch stagnation, the electron and ion densities are high enough (Fig. 5.3(b)) for sufficient electron-ion collisions to occur, so that the temperature difference between electrons and ions becomes small. $T_e \approx T_i$ at about 220 ns. High temperature and high density conditions are necessary to produce EUV radiation at pinch stagnation. The optimum electron temperature and density for 13.5 nm EUV emission from Xe plasmas are $25 \sim 30$ eV and $10^{18} \sim 10^{19}$ cm^{-3}, respectively[95]. Although the electron temperature in this figure is higher than the optimum at stagnation, it is tunable by changing the initial density distribution.

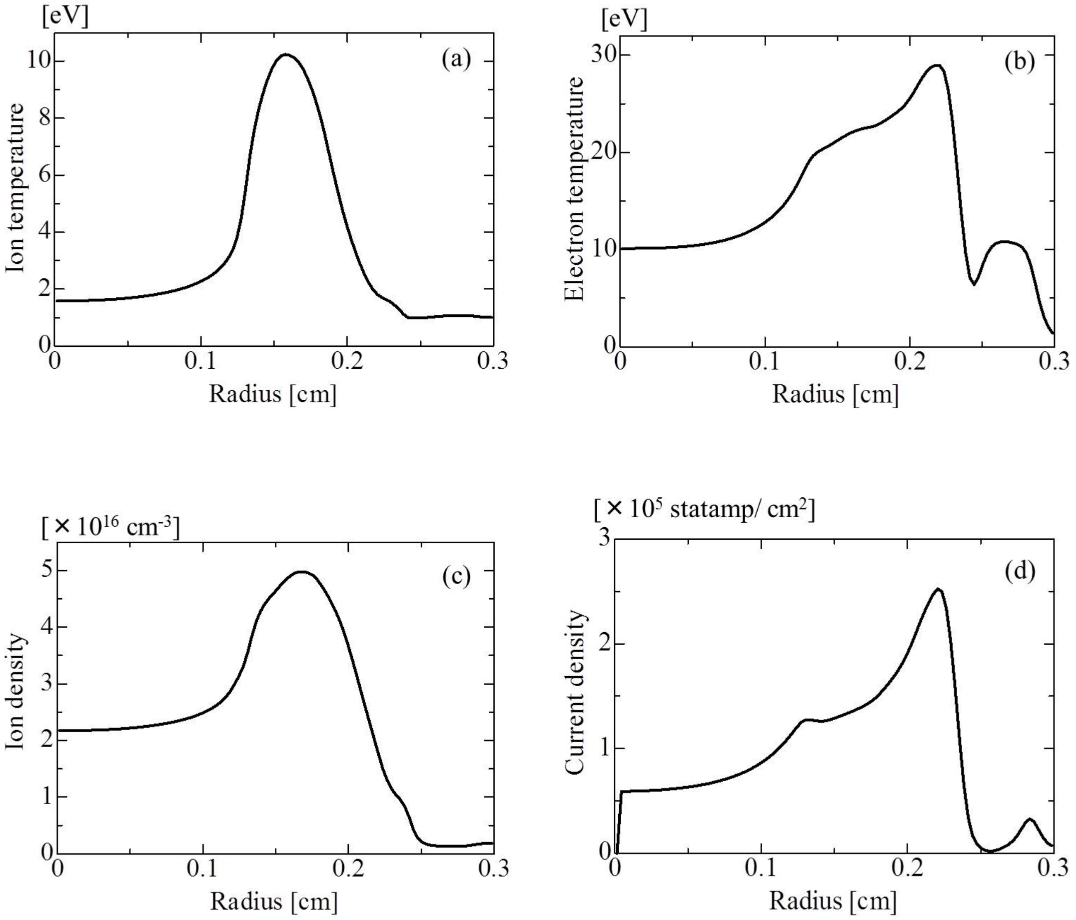

FIGURE 5.2: Radial distribution of (a) ion temperature, (b) electron temperature, (c) ion density, and (d) current density during implosion (t=150 ns).

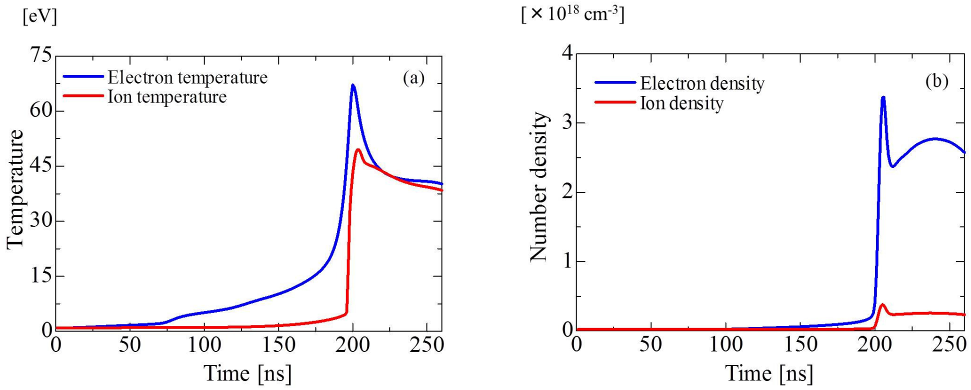

FIGURE 5.3: On axis electron and ion temperatures (a), electron and ion densities (b), as a function of time without initial perturbation.

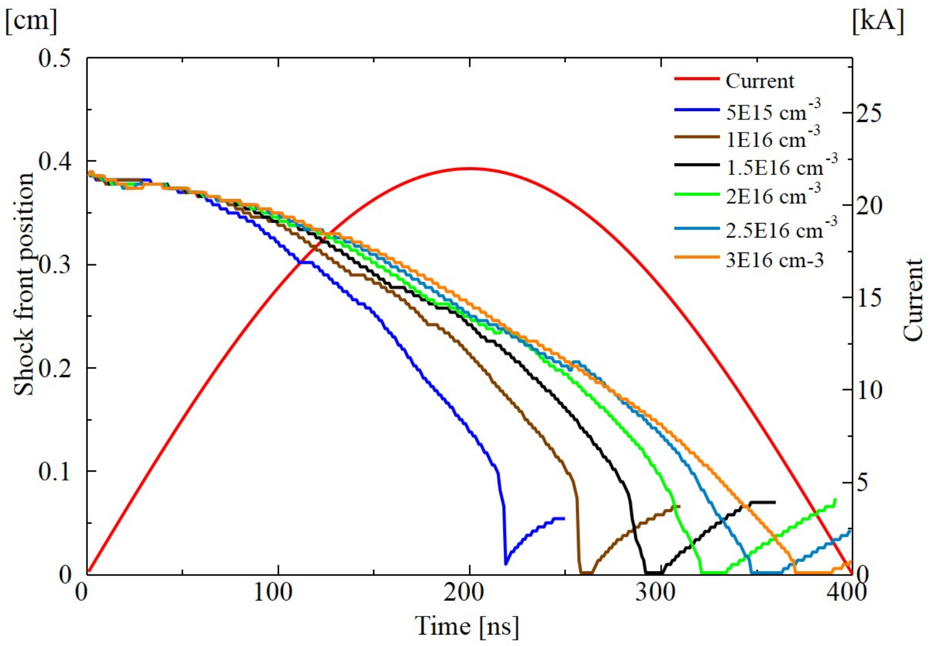

FIGURE 5.4: Position of shock front r_s as a function of time for different initial uniform densities.

5.1.2 Influence of Initial Conditions on Z-pinch Dynamics

From the mathematical perspective, given the governing equations and corresponding initial and boundary conditions, the behavior of the whole system can be described numerically. In the time-resolved EUV radiation measurement, we found that the gas inlet pressure, and thus initial density, plays an important role in determining the pinch evolution. In this section, its influence on pinch dynamics is numerically analyzed.

Fig. 5.4 illustrates the position of shock front r_s as a function of time for different initial uniform densities (from $5{\times}10^{15}$ to $3{\times}10^{16}$ cm^{-3}). In Z-pinch, we define the time when the shock front reaches the axis as the pinch time. It is shown in the figure that by increasing the initial density, the pinch time is delayed. The dependences of pinch electron temperature and electron density at stagnation on initial density can provide us a further understanding. As shown in Fig. 5.5, the increasing of the initial density leads to monotonic decreasing of the electron temperature at pinch stagnation. On the other hand, for the initial density range of $0.5 - 2 \times 10^{16}$ cm^{-3}, the electron density at stagnation also increases monotonically; however, it decreases when the initial density

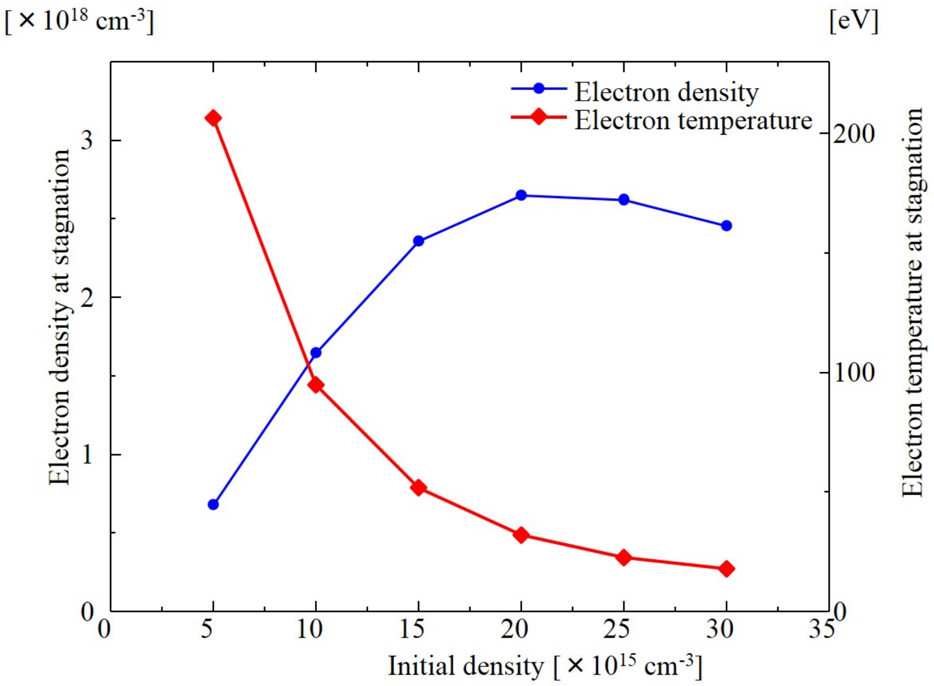

FIGURE 5.5: Electron temperature (red) and electron density (blue) at stagnation versus initial density.

exceeds 2×10^{16} cm^{-3}. We can relate this result to the experimental results in Sec. 3.1. Considering that there are optimum ranges for electron density and temperature[95] (T_e : $25 - 30$ eV, n_e : $10^{18} - 10^{19}$ cm^{-3}), there exists an optimum inlet gas pressure (namely optimum initial density) for EUV radiation. According to Fig. 5.5, the optimum initial density is between $2 - 3 \times 10^{16}$ cm^{-3}.

5.2 Magneto-Rayleigh-Taylor Instabilities in Z-pinch

In a Z-pinch, the pulsed current induces an azimuthal magnetic field so that the magnetic piston compresses the plasma column toward the axis, accompanied by a shock wave. The arrival of the shock front at the axis marks the start of the stagnation phase[88], during which the plasma kinetic energy is converted to thermal, ionization and radiation energies[88, 137]. The initial non-uniformity of the electron density in the plasma column is inevitable because of the stochastic nature of the breakdown process[87]. Z-pinches are thus inherently susceptible to MRT instabilities, especially for large-radius and long-time implosions. This instability[138, 139] occurs at the plasma-magnetic piston interface and is believed to be capable of degrading implosion symmetry and limiting the Z-pinch source performance.[140] The HVM of EUV lithography requires the light source not only to have efficient output power but also to have high spatial stability, pulse-to-pulse energy stability, and a smaller spot size. It is therefore necessary to investigate the evolution of MRT instability and mitigation methods in order to design a suitable EUV radiation source. In the MRT simulation, the initial Xe ion density is assumed to be $n_0 = 2 \times 10^{16}$ cm^{-3}, and the initial electron and ion temperatures $T_e = T_i =$1 eV.

5.2.1 MRT Instability Simulations

MRT instability is an inherent problem for Z-pinches. In this section, we focus on the simulation of a Z-pinch with a uniform initial density distribution on which perturbations are superimposed. The density perturbation for a single mode is given by

$$\rho(r, z) = \rho_0(1 + \delta_0 \cdot \cos(\frac{2\pi}{\lambda} \cdot z))$$

where δ_0 is the initial perturbation amplitude, λ the wavelength of the perturbation, and ρ_0 the unperturbed density. For unperturbed region, the density is still ρ_0. The multi-mode perturbation is a superposition of single mode perturbations.

Fig. 5.6 shows an example of ion density evolution with initial multi-mode perturbation wavelengths of λ=0.75 mm, λ=1.5 mm, and λ=3 mm at (a) 145 ns, (b) 223 ns, and (c) 260 ns, respectively. The initial perturbation amplitude is $\delta_0 = 0.1$. The simulation shows that the shock front is MRT stable during the implosion phase (t=145 ns); while the region between shock front and magnetic piston is MRT unstable. The shock front remains stable even after it is reflected from the axis (t=223 ns), whereas the magnetic

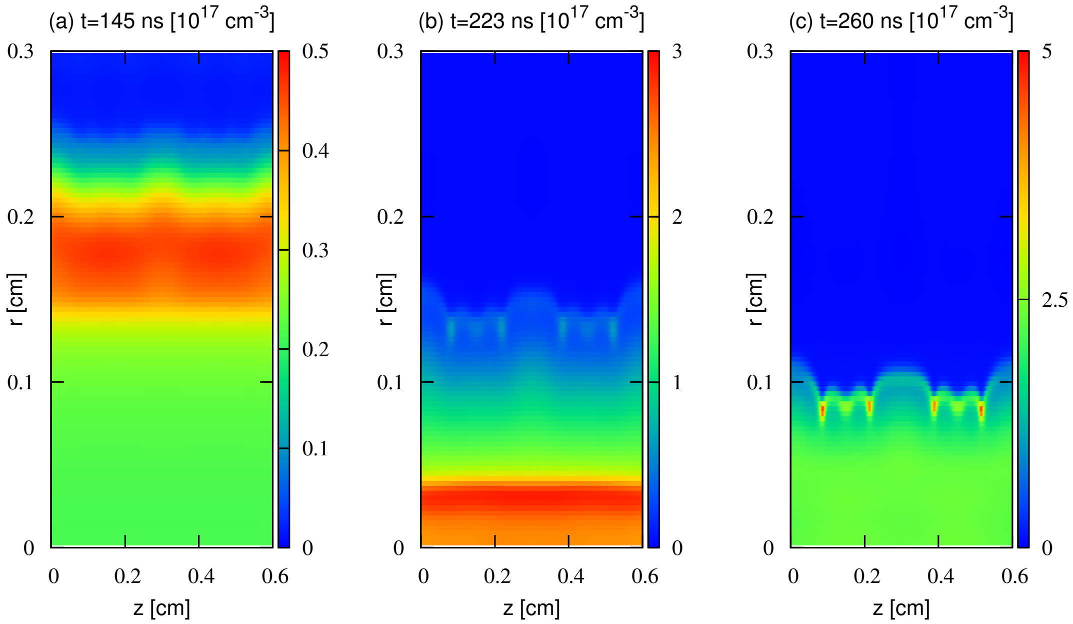

FIGURE 5.6: Ion density distribution during implosion with an initial multi-mode perturbation amplitude of 0.1 and wavelengths of λ=0.75 mm, λ=1.5 mm , and λ=3 mm at (a) 145 ns, (b) 223 ns, and (c) 260 ns.

piston region is severely perturbed. Shortly after, the magnetic piston arrives and interacts with the reflected shock indirectly at $r \sim 0.1$ cm. The turbulent motion is therefore transferred from the magnetic piston to the stagnated plasma[141], and perturbs the plasma column.

5.2.1.1 Single mode seeds

To better understand the evolution of the MRT instability, we simulate perturbations of single mode, multi-modes, and random modes respectively. The Fast Fourier Transform (FFT) is used to analyze the characteristics of the MRT instability. Fig. 5.7 shows the normalized FFT spectrum at the plasma-magnetic piston interface, r_p, with λ=1.5 mm and $\delta_0 = 0.1$ at 1 ns, 75 ns, 170 ns, and 205 ns, respectively for a single mode perturbation. Initially, only the fundamental harmonic originating from the single mode seed is present. The second harmonic appears after 75 ns, declaring the end of the linear

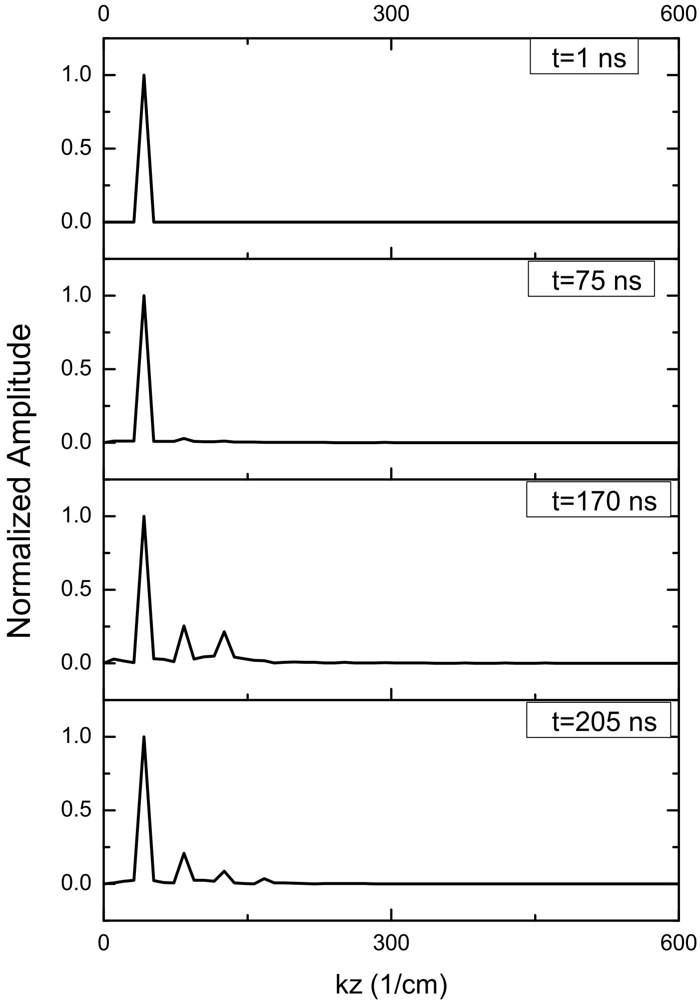

FIGURE 5.7: FFT spectrum of perturbation amplitude (λ=1.5 mm) and $\delta_0 = 0.1$ at 1 ns, 75 ns, 170 ns, and 205 ns, respectively

regime as the MRT instability enters the weak non-linear regime. As the MRT instability evolves, the third (t=170 ns) and higher order harmonics (t=205 ns) appear, indicating the MRT instability reaching the deep non-linear regime. According to classical linear theory, in the linear regime the fundamental harmonic grows exponentially as

$$\delta = \delta_0 \cdot e^{\gamma t}$$

where δ_0 is the initial perturbation amplitude, γ the growth rate. M. R. Douglas $et\ al.$ point out that the growth rate may remain in the exponential form after the onset of nonlinear development[139]. Fig. 5.8(a) shows the fundamental density amplitude (in arbitrary unit) as a function of time and its exponential fit for λ=1.5 mm and $\delta_0 = 0.1$. The growth rate for linear regime is γ=0.0492 ns^{-1}. In the final stage, the fundamental amplitude deviates from the exponential fit, indicating a much faster growth rate than in the linear regime. The growth rates for mm-scale perturbations up to 4 mm are shown in Fig. 5.8, and we find that longer wavelength modes have relatively smaller growth rates.

5.2.1.2 Multi-mode seeds

For multi-mode perturbation structures, the mode coupling effect becomes much more significant and further complicates the MRT evolution. Fig. 5.9(a) shows the spectral evolution of a two-mode structure comprised of λ=1.5 mm and λ=3 mm; and Fig. 5.9(b) shows the spectral evolution of a three-mode structure comprised of λ=0.75 mm, λ=1.5 mm, and λ=3 mm, respectively. The initial perturbation amplitude is $\delta_0 = 0.1$. During the initial stage($t = 1$ ns), only fundamental harmonics are present and their amplitudes are equal. During the implosion phase other harmonics are induced due to the mode coupling effect. At 205 ns, the mode coupling effect becomes so significant that the amplitudes of some induced modes reach more than 30% of the fundamental modes amplitudes. In the case of the three-mode structure, if we define the initial perturbation modes as $k1$ for λ=3 mm, $k2$ for λ=1.5 mm, and $k3$ for λ=0.75 mm, it is easy to find that a series of modes generated, including $k3 - k1,\ k1 + k3,\ k2 + k3,\ k1 + k2 + k3$, amongst others. In this situation, a severe bubble-and-spike structure is formed near the plasma-magnetic piston interface, as shown in Fig. 5.6. The lower density and larger local magnetic field cause high acceleration in the bubble regions between spikes, and also cause the severe perturbation observed. The magnetic field diffuses through the spike regions so that the driving forces reside at the bubble front, elongating the spikes.

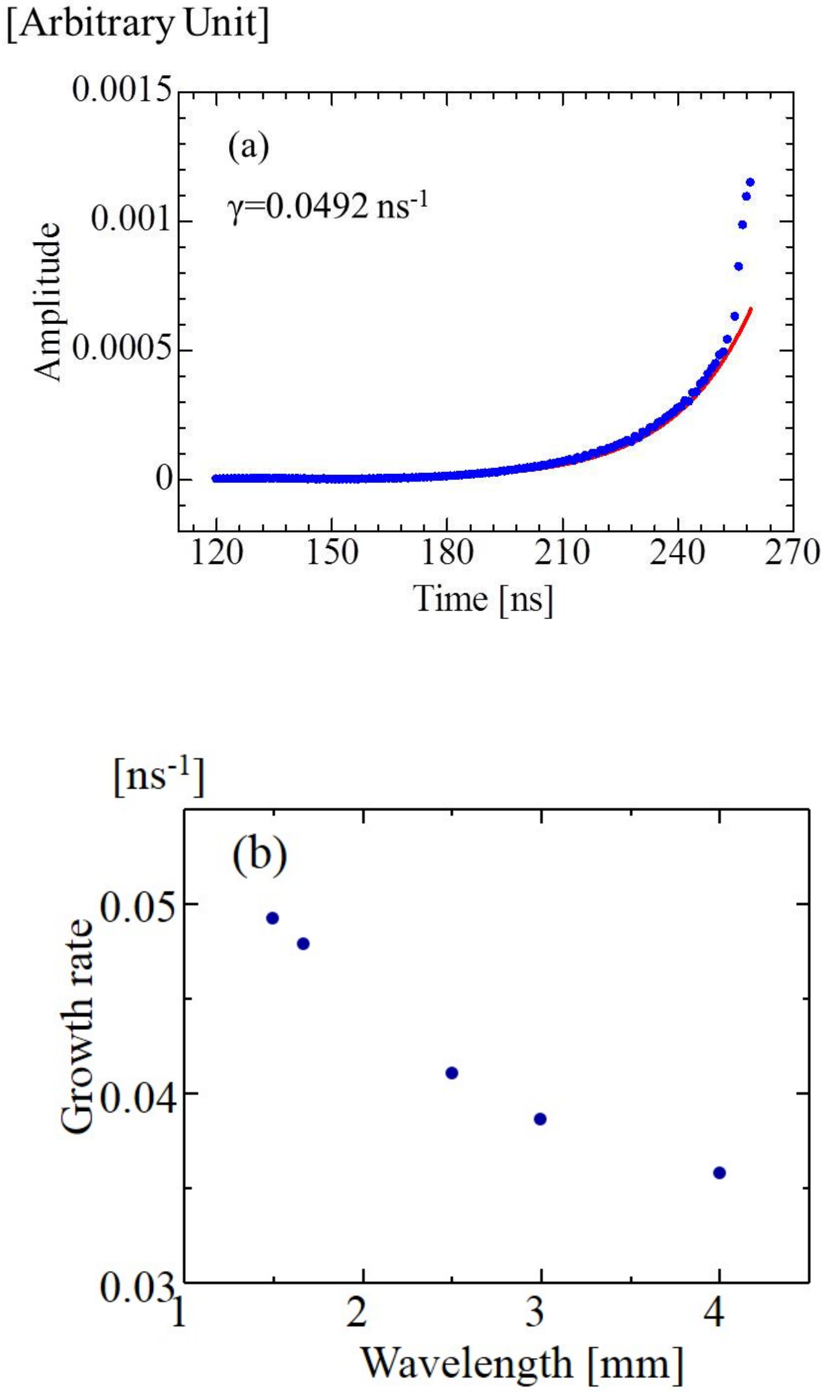

FIGURE 5.8: Time evolution of the fundamental FFT spectrum amplitude and its exponential fit for λ=1.5 mm and $\delta_0 = 0.1$ (a), and growth rate of the fundamental harmonic versus mm-scale wavelengths (b).

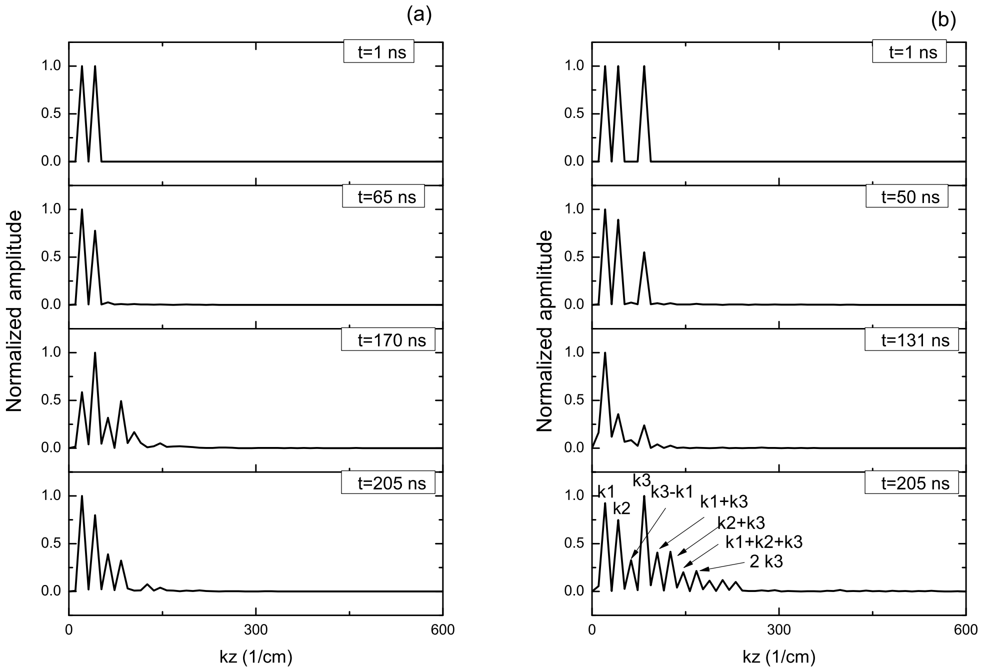

FIGURE 5.9: The temporal evolution of multi-mode structure FFT spectrum. (a) two-mode structure with λ=1.5 mm and λ=3 mm at 1 ns, 65 ns, 170 ns, and 205 ns; (b) three-mode structure with λ=0.75 mm, λ=1.5 mm, and λ=3 mm at 1 ns, 50 ns, 148 ns, and 205 ns. The perturbation amplitude is $\delta_0 = 0.1$.

5.2.1.3 Random seeds

Random density seeds have been used to model the MRT instability in Z-pinches and shown good agreement with experimental results[142–145]. The random seeds can be decomposed into a series of single mode seeds. For the perturbed region, the density perturbation for the random seeds is given by

$$\rho(r, z) = \rho_0(1 + \delta_0 \cdot Random\_Number)$$

where the initial amplitude $\delta_0 = 0.05$ and $Random\_Number$ is a random number between -1 and 1. For unperturbed region, the density is ρ_0. The spectral evolution of the random seeds perturbation at (a) 1 ns, (b) 50 ns, (c) 170 ns and (d) 205 ns are shown in Fig. 5.10. In the initial stage (t=1 ns), the FFT spectrum is distributed over a wide

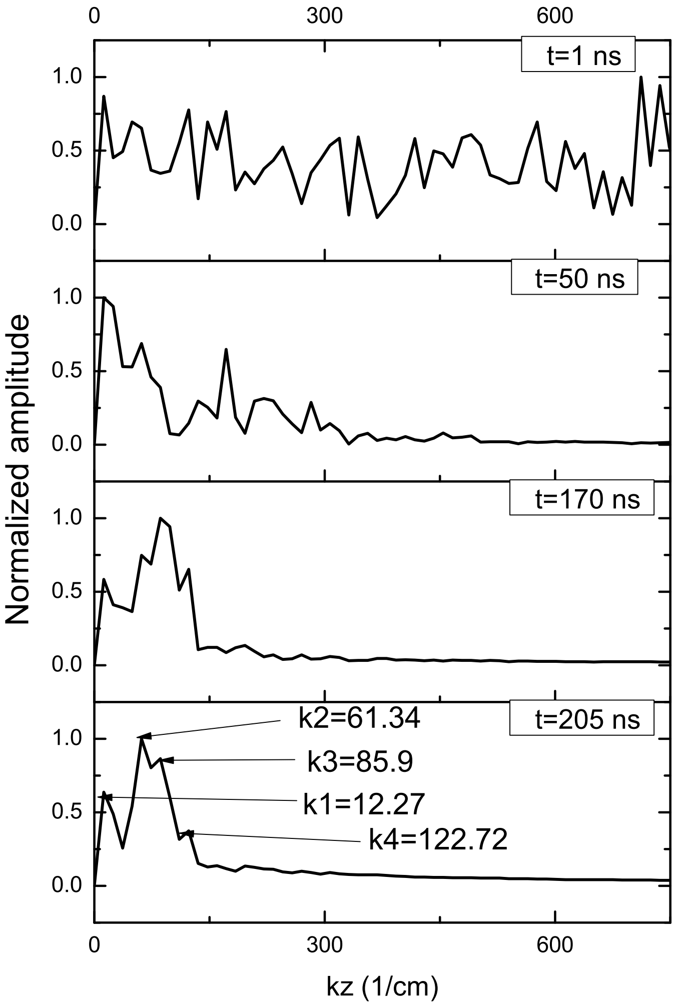

FIGURE 5.10: FFT spectrum of the MRT instability with random seeds for initial perturbation amplitude $\delta = 0.05$.

range of wave numbers. As the Z pinch evolves (t=50 ns), the shorter wavelength modes gradually vanish, and longer wavelength amplitudes increase. In the final image(t=205 ns), the dominant modes are $k1$=12.27 cm^{-1}, $k2$=61.34 cm^{-1}, and $k3$=85.9 cm^{-1}, corresponding to wavelengths of 5.12 mm, 1.02 mm, and 0.73 mm, respectively. The most dominant wavelength is $\lambda = 1.02$ mm. In our case, the thickness of the imploding plasma shell is on the order of 1 mm, as shown in Fig. 5.6. T. W. Hussey $et\ al.$ point out that the final dominant wavelength should be on the order of shell thickness of the imploding plasma[146]. In order to explain such characteristic wavelength, we employ an analytical MRT model that incorporating the structure of the imploding plasma shell.

The derivation of the analytical model and two characteristic scale δ and Δ are given in Appendix A. According to this model, the displacement perturbation ξ and the magnetic field perturbation B_1 due to MRT instability decreases exponentially along the radial direction toward axis, following the form of $\sim e^{kx}$, where $k = 2\pi/\lambda$ is the wave number of the MRT. Therefore, for small wavelength modes with large wave number, the perturbation cannot penetrate into the plasma shell deeply, localized near the surface within a very small depth. For adequate long wavelength that satisfies $2\pi\delta/\lambda \approx 1$, the exponential factor $e^{kx} = e^{k\delta} = e^{-1}$, indicating that the perturbation can penetrate into the shell. Therefore MRT modes with wavelengths longer than δ can further develop. On the other hand, the growth rate of single mode MRT is given by

$$\gamma = \sqrt{kg}$$

and thus shorter wavelength grows faster. Therefore for the resting modes, the final dominant one have the wavelength on the order of plasma shell thickness.

The MRT instability is also observed in our Z-pinch gas discharge experiment. An X-ray CCD camera, a 50 μm diameter pinhole, and a Zr filter (7 $\sim$ 16 nm) are assembled to form a pinhole imaging system to record the time-integrated EUV image. The detailed description is given in Sec.2.2.3.

The time-integrated EUV pinhole image for an inlet gas pressure of 24 Torr and d =50 cm is shown in Fig. 5.11. When weak pre-ionization (10 W) is applied, the EUV radiating column at stagnation suffers from instability. The wavelength of the instability is about 1 mm, consistent with our random seeds simulation. The inhomogeneity of the pinched plasma column causes two bright spots, which is undesirable for EUV source design. When the RF power is raised to 30 W, the initial uniformity of the plasma is improved so that the instability is suppressed. By further increasing the RF power, the MRT instability is completely mitigated and a homogeneous pinched plasma column is formed. However, the peak EUV radiation intensity decreases at the same time. Higher

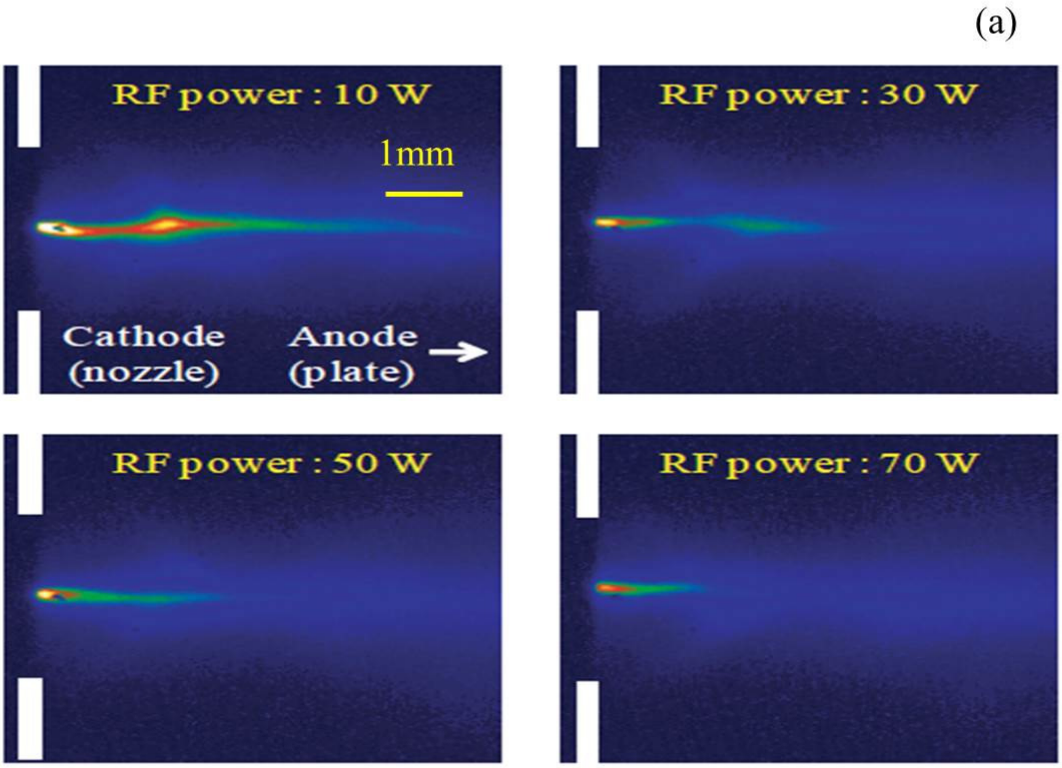

FIGURE 5.11: Time-integrated EUV pinhole image near the cathode region with pre-ionization powers of 10 W, 30 W, 50 W, and 70 W, respectively.

RF power will further heat the plasma and cause radial expansion of initial plasma distribution; thus affect the final pinch radius and temperature.

By changing the distance from the RF coil to cathode d, the EUV pinhole images differ significantly under fixed inlet gas pressure of 24 Torr and fixed RF power of 10 W, as shown in Fig. 3.8 in Sec. 3.3. For d =20 cm, the RF coil is close to the cathode, and sustains a uniform initial plasma distribution; therefore the pinched plasma at stagnation is relatively homogeneous. The MRT instability appears when d increases. Note that the final dominant wavelength of the MRT instability always remains around 1 mm. As discussed before, this characteristic wavelength is related with the shell thickness of the imploding plasma.

5.2.2 Mitigation of MRT instabilities

The influence of the MRT instability on pinch stagnation is important to determine the EUV radiation output. Fig. 5.12 shows the simulation results of on axis electron temperature and density at pinch stagnation. For single mode perturbation, the on axis electron temperature fluctuation is more pronounced at longer initial perturbation wavelengths than at shorter wavelengths, as shown in Fig. 5.12(a). The MRT instability stems from the plasma-magnetic piston interface and has a sinusoidal profile. This type of profile intensifies the magnetic pressure difference between bubble and spike region, and thus further deteriorates the Z-pinch. Therefore a temperature and density fluctuation along Z axis at pinch stagnation is formed. The temperature fluctuation is about 3.5 eV for a $\lambda = 4$ mm perturbation. Such a fluctuation would significantly alter the 13.5 nm EUV generation because the optimum electron temperature is between 25 eV and 30 eV[95], and thus has an optimum range of only 5 eV. On the other hand, in Fig. 5.12(b), while the on axis electron density distribution also fluctuates, it does not exceed the optimum electron density range (10^{18} to 10^{19} cm^{-3})[95]. Therefore the main reason for the non-uniformity of the EUV radiation at stagnation is the temperature fluctuation caused by the MRT instability.

RF pre-ionization can suppress the initial amplitude of instabilities[90], and contribute to MRT instability suppression in Z-pinches. Fig. 5.13 shows the simulation results of the peak to peak electron density and temperature fluctuations versus initial perturbation amplitude, for λ =3 mm at pinch stagnation. The on-axis fluctuations of both temperature and density are almost proportional to the initial amplitude; that means the uniformity at pinch stagnation is improved by decreasing the initial amplitude. Double bright spots are observed in the pinhole imaging experiment with RF power of 10 W, as shown in Fig. 3.8, because the instability causes the local temperature to be higher and satisfies the optimum condition. By increasing the RF pre-ionization power the initial

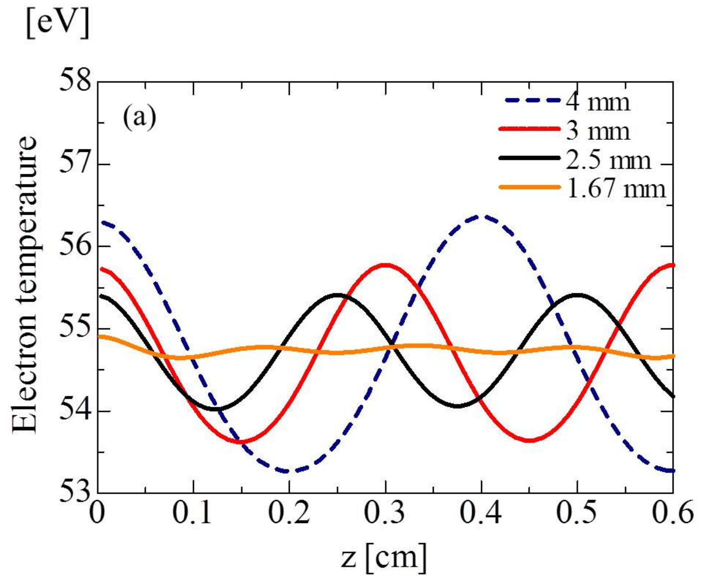

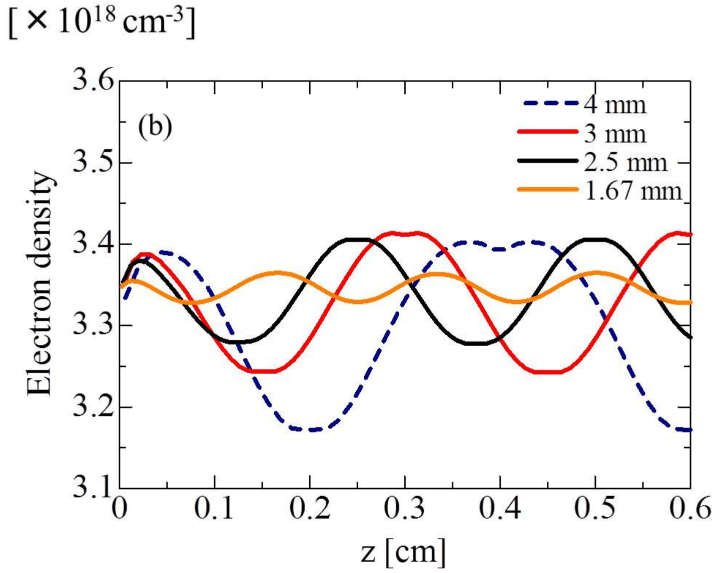

FIGURE 5.12: On axis distribution of electron temperature and density at stagnation (t=207 ns). (a) Single mode on axis electron temperature distribution with wavelengths of 4 mm, 3 mm, 2.5 mm, and 1.67 mm. (b) Single mode on axis electron density distribution with wavelengths of 4 mm, 3 mm, 2.5 mm, and 1.67 mm.

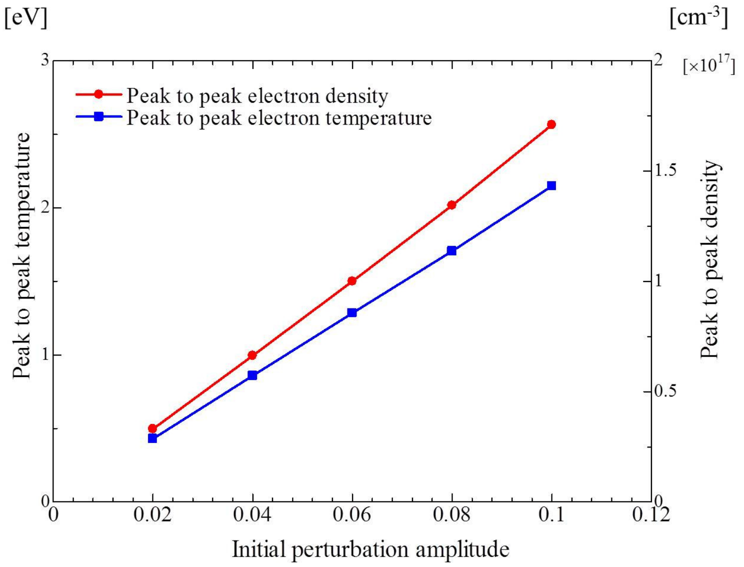

FIGURE 5.13: Peak to peak electron density and temperature fluctuation versus initial amplitude for λ=3 mm single mode perturbation at pinch stagnation.

amplitude of instabilities is suppressed so that more uniform pinched plasma column can be formed.

In previous experiment[147], increasing dI/dt was shown to be an effective method to enhance the stability of the Z-pinch EUV source. By increasing dI/dt, the shell thickness of the imploding plasma becomes thinner, thus shortening the final dominant wavelength of the instability. As shown in Fig. 5.12, shorter wavelength leads to weaker temperature and density fluctuations in the stagnation phase, which can improve the uniformity of the pinched plasma column. On the other hand, shorting the current rise time also leads to the change of pinch time, and plasma dynamics. Fig. 5.14(a) shows the pinch time as a function of frequency with random seed perturbation. The pinch time is postponed when the current rise time is elongated. The axial kinetic energy $KEz = \sum \frac{1}{2} n_i m_i v_z^2$ is used to characterize the MRT instabilities[149]. The effect of MRT mitigation through shorting the current rise time is confirmed by simulation results and shown in Fig. 5.14(b). From 0.6 to 1.0 ω_0, increasing the current frequency can suppress the MRT instabilities significantly. From 0.6 to 1.0 ω_0, the suppression effect becomes weaker. The electron temperature and electron density are also affect

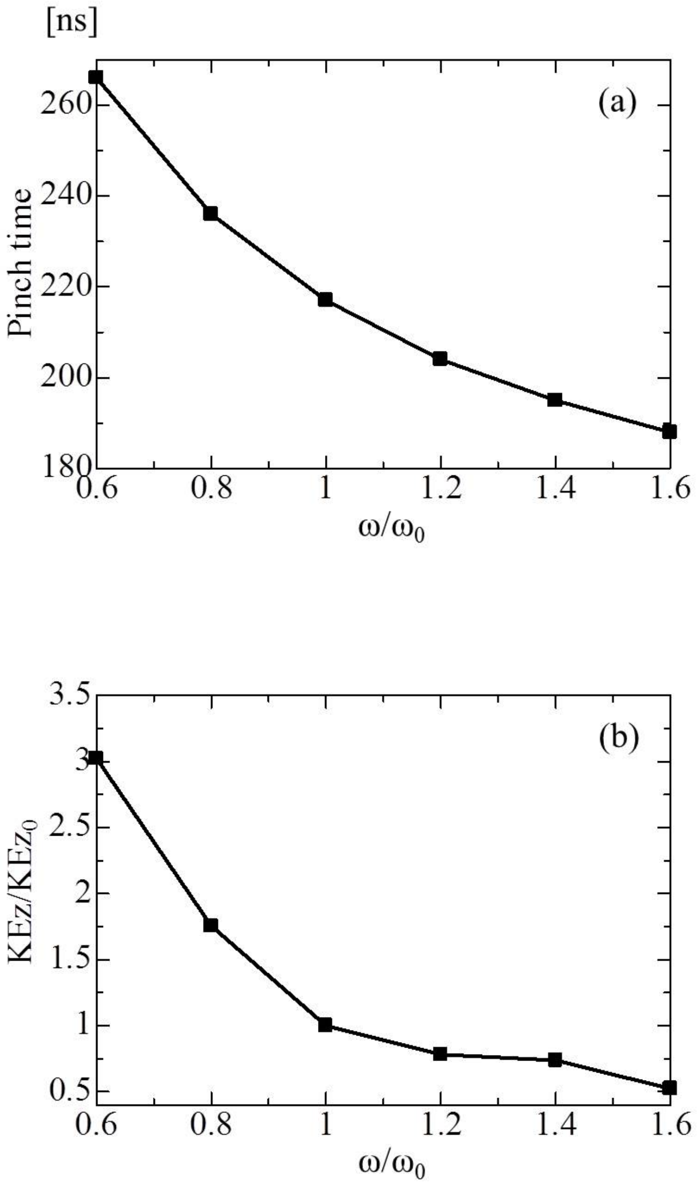

FIGURE 5.14: Random seed MRT simulation results of (a) pinch time as a function of current frequency; (b) axial kinetic energy as a function of current frequency, where $\omega_0 = 1 \times 10^7$ rad s^{-1}, initial density $n_0 = 2 \times 10^{16}$ cm^{-3}. KEz$_0$ indicates the axial kinetic energy of plasma due to MRT instabilities with current frequency of ω_0.

by changing the current frequency, as shown in Fig. 5.15. There is a maximum electron temperature near $\omega = 1.2\omega_0$, while the electron density increases monotonically by increasing current frequency. Thus, according to the above discussions, a current frequency around 1.4-1.6 $\times 10^7$ rad s^{-1} is preferred for EUV generation.

Applying an axial magnetic field is believed to be capable of mitigating MRT instability[87,

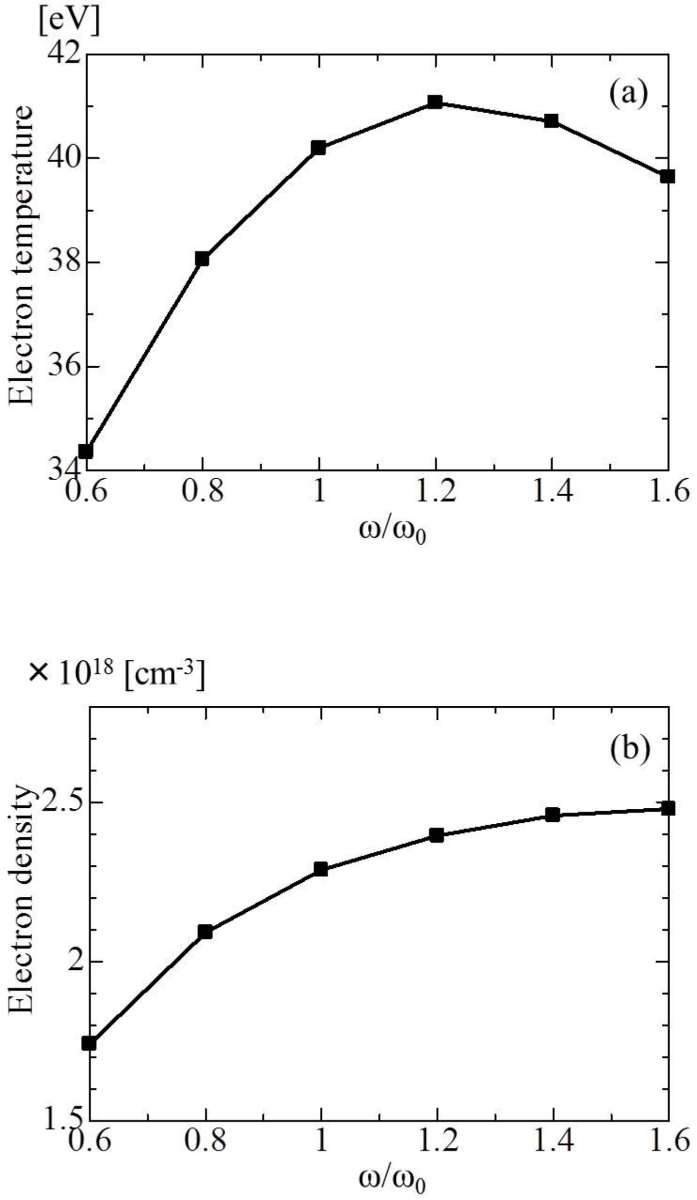

FIGURE 5.15: Random seed MRT simulation results of (a) electron temperature at pinch stagnation as a function of current frequency; (b) electron density at pinch stagnation as a function of current frequency, where $\omega_0 = 1 \times 10^7$ rad s^{-1}, initial density $n_0 = 2 \times 10^{16}$ cm^{-3}.

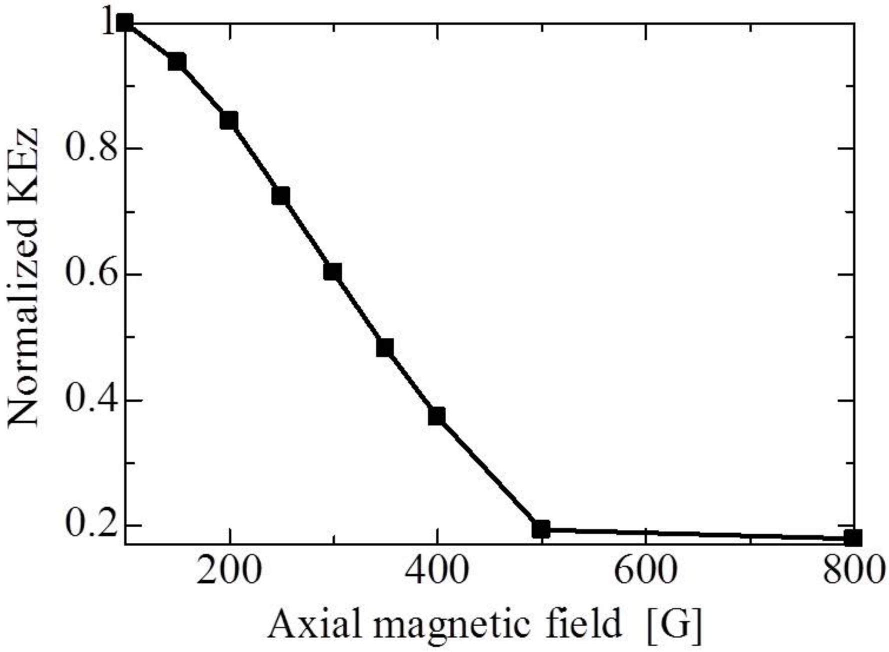

FIGURE 5.16: Normalized axial kinetic energy as a function of axial magnetic field at $t = 210$.

148]. The mitigation effect of an axial magnetic field can be explained by an analytical model. The derivation of that analytical model is given in Appendix B.

The growth rate of MRT when axial magnetic field applied is:

$$\Gamma \approx |gk|^{1/2} 2^{7/4} (s\chi)^{1/2} \text{exp}(-\pi\chi/2) \tag{5.1}$$

Where d is plasma shell thickness. χ is a dimensionless parameter defined as

$$\chi^2 \approx \text{min}(B_1^2, B_2^2)/|B_1^2 - B_2^2|. \tag{5.2}$$

and acceleration

$$g \approx (B_1^2 - B_2^2)/8\pi\rho_0 d, \tag{5.3}$$

The MRT evolution with an axial magnetic field B_z up to 800 G is simulated. Fig. 5.16 shows the normalized axial kinetic energy at $t = 210$ ns versus axial magnetic field.

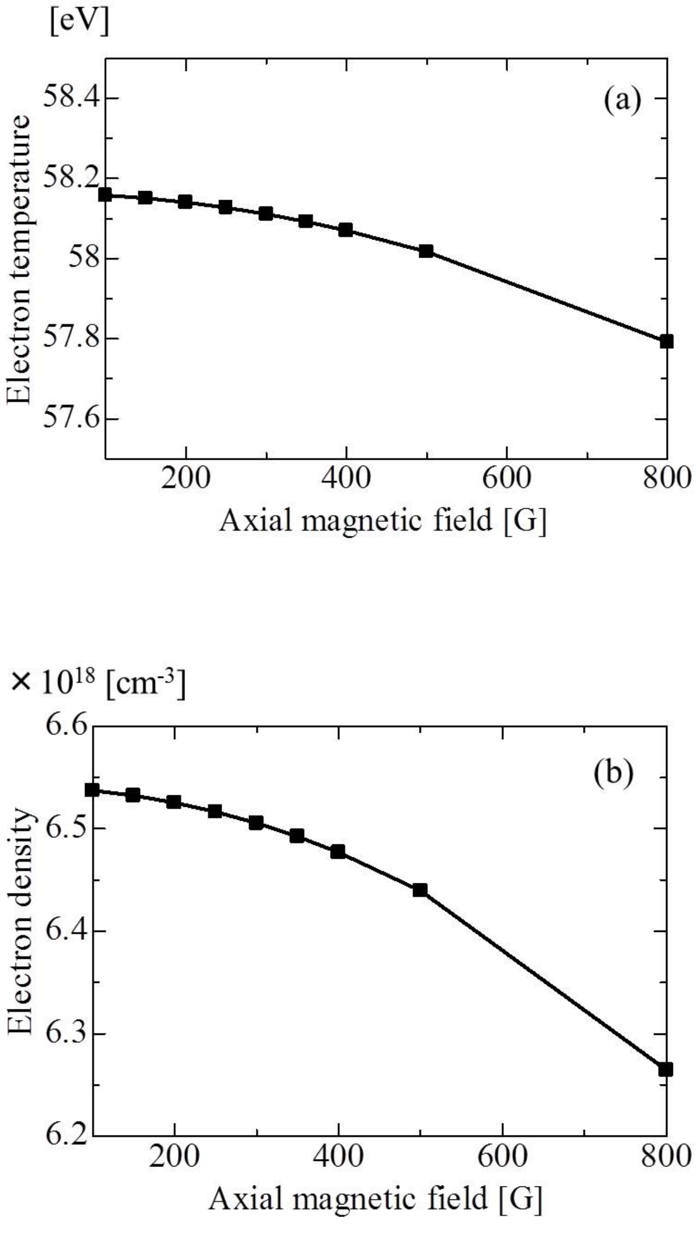

FIGURE 5.17: Simulation results of single mode MRT perturbation with wavelength of 1.5 mm. (a) electron temperature at pinch stagnation as a function of axial magnetic field; (b) electron density at pinch stagnation as a function of axial magnetic field.

From 100 to 500 G, the axial kinetic energy have almost been mitigated; by further increasing the axial magnetic field up to 800 G, the KEz changes little. The influences of axial magnetic field on electron temperature and electron density at pinch stagnation are shown in Fig. 5.17. The influences are not quite significant because the axial magnetic field is weak compared with the azimuthal magnetic field; although during implosion phase the axial magnetic field is frozen within the plasma column and thus be stronger than the initial field. However, if the initial magnetic field is too strong, the axial magnetic field may change the plasma dynamics significantly or even conquer the azimuthal magnetic field and stop the pinch. Therefore, Bz $\sim$ 500 G is preferred for MRT mitigation.

5.3 Summary

In the first section of this chapter, the simulation results of plasma evolution without initial perturbation were present. The motions of shock front and magnetic piston, and on axis density and temperature evolution were investigated. In addition, the plasma and current structure during implosion were shown. Shock heating heats the ions; while Joule heating heats electrons. The shell thickness of the imploding plasma was about 1 mm. Then the influences of initial density on Z-pinch was also studied. It was demonstrated that higher initial density caused the delay of pinch time. The relationship between electron density/temperature at stagnation and initial density was also clarified. The increasing of the initial density led to monotonic decreasing of the electron temperature at pinch stagnation. On the other hand, the relation between pinched electron density and initial density is not a monotonic function. For the initial density range between 0.5 and 2×10^{16} cm^{-3}, the electron density at stagnation increased monotonically when initial density increased; however, it decreased when the initial density exceeded 2×10^{16} cm^{-3}. Such tendency provided an explanation for the optimum inlet gas pressure for EUV radiation in Sec. 3.1. The optimum initial density is between

$2 - 3 \times 10^{16}$ cm^{-3}. In the second section, the MRT instabilities were studied. The characteristics of MRT instabilities with single mode, multi-mode, and random mode initial perturbations were present. In case of single mode perturbation, shorter wavelength modes grew faster than that of longer wavelength modes. High order harmonics appeared when the MRT entered into non-linear regime. For multi-mode perturbation, the mode coupling effect led to the generation of new modes, complicated the MRT evolution. It was shown in the random seeds simulation that the final dominant modes tend to converge to mm-scale wavelength around 1 mm. Such characteristic wavelength was also observed in EUV pinhole experiment. It was on the order of the shell thickness. MRT instabilities was proved to cause the temperature and density fluctuations along Z axis, which is responsible for the non-uniformity of the EUV radiation. The fluctuations caused by perturbation of longer wavelength was more pronounced than that of shorter wavelength. Finally, the mechanisms of MRT mitigation methods, including applying an axial magnetic field, RF pre-ionization, and shortening current rise time, were present. The RF pre-ionization can suppress the amplitude of initial perturbation, thus mitigate the MRT instability. Higher dI/dt caused a thinner plasma shell during implosion, which shortening the final dominant wavelength of the MRT instabilities. Whereas smaller wavelength of MRT instability led to weaker density and temperature fluctuation, preferred by EUV radiation. A current frequency about 1.4-1.6 $\times 10^7$ rad s^{-1} is preferred for the DPP EUV source. The suppression of MRT instability by applying an axial magnetic field was verified. The preferred axial magnetic field is about 500 G.

Chapter 6

Conclusions

The main goals of the research reported in this thesis are as follows. The first one is to diagnose the plasma produced in a 13.5 nm Xe DDP EUV source, in order to understand the plasma dynamics during the whole discharge process. Then, in order to further understand the plasma dynamics in the EUV source and explain some experimental phenomena, the second goal is to simulate the plasma behaviors in the DPP EUV source. Finally, based on both experimental and numerical investigations, we propose possible ways to optimize the EUV source. Although this work focuses on the 13.5 nm Xe DPP EUV source for EUV lithography, the extent of the plasma diagnostic techniques and simulation code are not limited to this specific devices. Instead, they can be applied to other plasma sources with similar properties. In this chapter, a summary of the main conclusions of this work is present.

I. The time-resolved EUV emission was measured and the preferred experimental conditions were quantified, and analyzed with MHD simulation. The preferred inlet gas pressure was 25 Torr, and the preferred electrode gap length was 16 mm. The inlet gas pressure played a dominant role in determining the EUV radiation. According to the simulation, higher pressure (and thus initial density) can delay the pinch time, alter the final pinch state, and lead to a lower pinch temperature. In contrast, there was a peak pinch density when initial density was 2×10^{16} cm^{-3}. The optimum initial density range for EUV output is $2 - 3 \times 10^{16}$ cm^{-3}.

II. The plasma dynamics in Z-pinch were studied with both time-resolved plasma imaging and MHD simulation. The initial discharge radius was about several mm. At stagnation, the emission became strongest, with a pinch radius of $\sim$0.1 mm. After that, due to Zippering effect, the radiating column was elongated and then moved along z axis. The simulation showed that during implosion phase, a shock front was formed ahead of the magnetic piston. The heating mechanisms for ions and the electrons during implosion were shock heating and Joule heating, respectively. At pinch stagnation, the kinetic energy of plasma was transferred to thermal energy, and caused the abrupt increasing of electron and ion temperature, achieving an ideal condition for EUV radiation.

III. The electron density distribution and evolution were investigated with both Nomarski interferometer and MHD code. The electron density was on the order of $10^{18} \sim 10^{19}$ cm^{-3} in the Z-pinch. The EUV intensity peaked quite near electron density maximum ($\sim 10^{19}$ cm^{3}) during the pinch process. The order of magnitude of the electron density was consistent with the MHD simulation results and within the theoretical optimum electron density range for EUV radiation.

IV. The ion kinetics was measured with a FC. The most probable ion velocity was $\sim$18 km/s. Most ions had kinetic energy smaller than 500 eV. The ion velocity distribution follows SMB fitting.

V. The EUV radiation fluctuation due to MRT instabilities was observed experimentally (time-integrated EUV pinhole imaging), and studied numerically (MHD simulation) and analytically (MRT analytical model). Pinhole imaging reveals that the MRT instabilities can be suppressed with sufficient RF pre-ionization; however, when it existed, its wavelength was always around 1 mm. Then MHD code was used to quantitatively investigate the characteristics of MRT instabilities in Z-pinch. The evolution of MRT with single mode, multi-mode, and random mode perturbations were analyzed. Higher order harmonics appeared when the MRT entered into non-linear regime. Modes with shorter wavelengths grew faster than longer ones. The mode coupling effect played an important role in the evolution of multi-mode MRT instabilities, which led to the generation of a series of new modes. For random mode perturbation, the final dominant modes tended to converge to a mm-scale wavelength around 1 mm, consistent with the experimental result. According to the analytical solution of the MRT instabilities, short wavelength modes perturbation cannot penetrate into the plasma shell deeply, and were thus localized near the surface region. Only those modes with wavelength on the order of shell thickness or longer can penetrate into the shell and further develop during Z-pinch. For the resting modes, the ones with shorter wavelengths grow faster; thus the final dominant modes are those with wavelengths $\sim$ 1 mm.

VI. The influences of MRT instabilities on pinch stagnation and EUV output were investigated and three mitigation methods were proposed to optimize the EUV source. MRT instabilities was proved to cause the temperature and density fluctuations along Z axis, which was responsible for the non-uniformity of the EUV radiation. Longer wavelength perturbation caused a more pronounced the fluctuation. According to the numerical simulation, the RF pre-ionization can suppress the initial amplitude of perturbation and thus mitigate the MRT instability. The EUV pinhole experiment validated the effect of RF pre-ionization on MRT mitigation. In addition, higher dI/dt caused a thinner plasma shell during implosion, thus shorter wavelength MHD modes can penetrate into the shell and developed to be the dominant mode. The shorter wavelength caused smaller temperature and density fluctuation along Z axis, namely the uniformity was better. The preferred pulsed current frequency is $\sim$ 1.4-1.6 $\times 10^7$ rad s^{-1}. Finally, the simulation results showed that the MRT instability can be suppressed by applying an axial magnetic field. The preferred axial magnetic field is 500 G.

In conclusion, the experiments and simulations described above provided a comprehensive understanding of the plasma dynamics in DPP EUV source. For the first time the characteristics of MRT instabilities and their influences on a Z-pinch DPP EUV source were investigated qualitatively. Favorable experimental conditions for EUV generation were analyzed, potential ways to scale up the in-band EUV power with high homogeneity were present, including controlling the initial density to be $2 - 3 \times 10^{16}$ cm^{-3}, designing a pulsed current with frequency of $\sim$ 1.4-1.6 $\times 10^{7}$ rad s^{-1}, and applying axial magnetic field $\sim$ 500 G. This study provided useful information for the EUVL industrial for further optimizing the EUV source.

In the future, we will further investigate the influences initial RF plasma conditions, such as density profile and temperature distribution, on final pinch stagnation and the EUV emission. Besides, we will also experimental mitigate the MRT instability to achieve a more homogeneous EUV source.

Appendix A

Analytical MRT Modeling

The density profile for a thin annular plasma accelerated by a magnetic field has two characteristic scales, $\Delta = \sqrt{\eta t}$ (we use resistivity units such that η is the magnetic diffusivity, i.e. $\eta \to \eta c^2/4\pi$ in Gaussian units) and $\delta = c_s^2/g$, where c_s is the sound speed and g the acceleration[150]. The schematic of the density profile is sketched in Fig. A.1. We can estimate the ration of scales from force balance:

$$\rho \Delta g \approx B^2/8\pi, \tag{A.1}$$

we have

$$\Delta/\delta \approx B^2/8\pi\rho c_2^2 = 1/\beta. \tag{A.2}$$

where $\beta = 8\pi P/B^2$ is the ratio of plasma pressure and magnetic pressure. We exploit this separation of spatial scales in the following to derive an approximate linear theory.

Defining $x = r_{sh} - r$, where r_{sh} is the outer radius of the sheath, and assuming δ, $\Delta \ll r_{sh}$, we can write the MHD equilibrium equation in an accelerated reference frame as:

$$\rho g = -\frac{\partial}{\partial x}(P + \frac{B^2}{8\pi}) \tag{A.3}$$

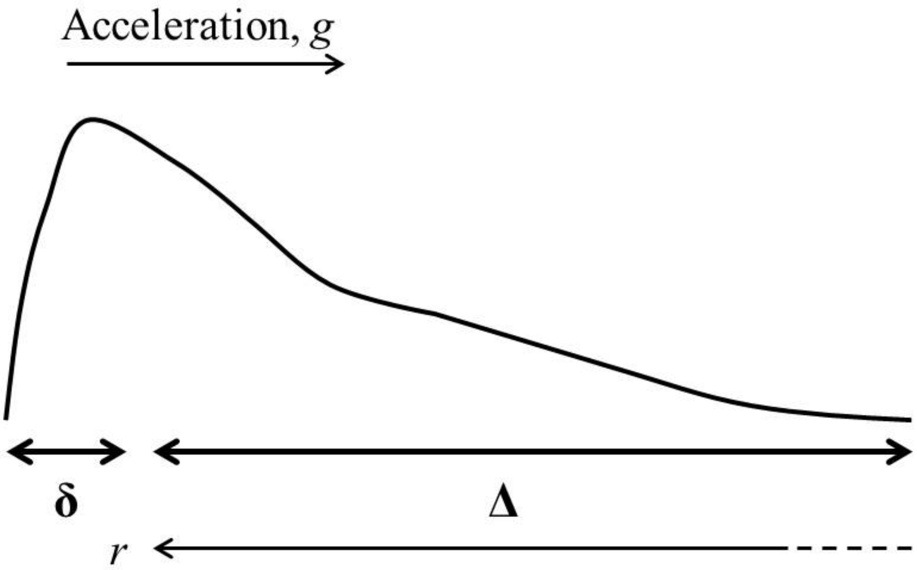

FIGURE A.1: Schematic of the density profile of a thin annular plasma accelerated by a magnetic field.

For simplicity, we assume constant temperature so that the pressure is given by $P = \rho c_s^2$, with c_s a constant. For scales much shorter than the resistive skin depth, Δ, the current density will be uniform, $\partial B/\partial x = \text{const}$. Assuming $\beta \ll 1$, we can then solve Eq. (A.3) for the density profile,

$$\rho = \rho_0(1 - e^{-x/\delta}). \tag{A.4}$$

This solution shows the density rise at the outer portion of the sheath depicted in Fig. A.1. This is unstable region from the point of view of MRT instability. Next, we consider linear stability of the accelerated equilibrium. Azimuthal symmetry is assumed for the modes. Since $g \approx r_{sh}/t_{implosion}^2$, and restricting to $kr_{sh} \gg 1$, we have $\gamma t_{implosion} \approx \sqrt{kr_{sh}} \gg 1$. Since the growth rate is large compared to the rate of change of equilibrium quantities, we can assume perturbations vary approximately as exp($\int \gamma dt$), with γ calculated from the instantaneous linearized equations. In order to make use of the analytical equilibrium in Eq. (A.4), we are also restricted to $k\Delta > 1$.

The linearized resistive MHD equations are given by

$$\begin{cases} \rho_1 = \nabla \cdot \rho \boldsymbol{\xi}, \\ \rho \dfrac{\partial^2 \boldsymbol{\xi}}{\partial t^2} + \rho_1 \mathbf{g} = -\boldsymbol{\nabla}(P_1 + BB_1), \\ \dfrac{\partial \mathbf{B_1}}{\partial t} = \boldsymbol{\nabla} \times (\dfrac{\partial \boldsymbol{\xi}}{\partial t} \times \mathbf{B}) + \eta(\nabla)^2 \mathbf{B_1}, \\ P_1 = \rho_1 c_s^2. \end{cases} \tag{A.5}$$

We have assume uniform resistivity and an isothermal equation of state for the perturbations. Taking the perturbed density, displacement, and magnetic field, ρ_1, ξ, and $B_1 \propto \exp(ikz + \int \gamma dt)$, we can algebraically eliminate ρ_1 and ξ_{1z}. The resulting equations are

$$\begin{cases} -\gamma^2 \rho \xi + \rho' g \xi - g \dfrac{\rho}{B}(RB_1 + \xi B') = -\dfrac{\gamma^2}{k^2}(\rho \xi' + \dfrac{\rho}{B}(RB_1 + \xi B'))', \\ B_1 + (\dfrac{c_s^2}{v_A^2} + \dfrac{\gamma^2}{k^2})(RB_1 + \xi B') = -\dfrac{\gamma^2}{k v_A^2} \xi' + \dfrac{\xi \rho' c_s^2}{B}. \end{cases} \tag{A.6}$$

where $\xi = \boldsymbol{\xi}_x$, $RB_1 = B_1 - (\eta/\gamma)(\partial^2/\partial x^2 - k^2)B_1$, $(\,)' = (\partial/\partial x)(\,)$, and $v_A^2 = B^2/4\pi\rho$. The boundary conditions are $\xi = 1$, $B_1 = -\xi B'$ at $x = 0$, and ξ, $B_1 \to 0$ as $x \to \infty$.

For the density profile given in Eq. (A.4), the largest eigenvalue of Eq. (A.6) can be found analytically an its growth rate is given exactly by

$$\gamma = \sqrt{kg}. \tag{A.7}$$

with solutions

$$\xi = e^{-kx}. \tag{A.8}$$

and

$$B_1 = -B' e^{-kx}. \tag{A.9}$$

This eigen-mode can be considered as a surface mode since it decays as e^{-kx}, and the short wavelength that grow most rapidly are localized to the region near $x = 0$.

Appendix B

MRT Mitigation by Axial Magnetic Field

Consider a plasma layer with width $2a$ being accelerated in the $+\vec{z}$ direction by the pressure of a uniform magnetic field, $\mathbf{B} = B_x\vec{\mathbf{e}}_x + B_y\vec{\mathbf{e}}_y$, which is in the ($x$,$y$) plane, as shown in Fig. B.1. We will transform to a frame of reference moving with the plasma layer. In this reference frame there will be an effective gravitational field

$$\mathbf{g}(z,t) = g\vec{e}_z = -\frac{du_z}{dt} \tag{B.1}$$

We assume that the plasma is in a stationary equilibrium in the co-moving frame of reference in a gravitational field, and there is no equilibrium flow of the plasma in this frame of reference. Then, the equilibrium force equation will be

$$\frac{dP}{dz} + \frac{1}{8\pi}\frac{d}{dz}(B_x^2 + B_y^2) = \rho g, \tag{B.2}$$

and the equation of motion reads

$$\rho\frac{d\mathbf{u}}{dt} = -\nabla P + \frac{1}{4\pi}(\nabla \times \mathbf{B}) \times \mathbf{B} + \rho g. \tag{B.3}$$

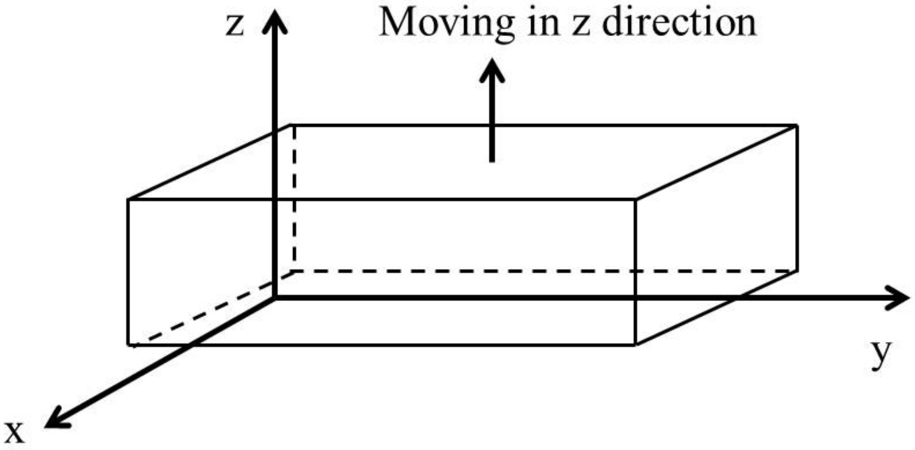

FIGURE B.1: Schematic of a plasma layer accelerated in the $+\vec{z}$ direction by the pressure of a uniform magnetic field.

This configuration of a heavy fluid that is supported by a massless fluid is evidently MRT unstable. We assume a small perturbation of the layer and that all quantities are linearized about the equilibrium state. Introducing the displacement vector $\xi(\mathbf{r}, t)$, and tanking into account that for a plane geometry, equilibrium symmetry implies that the perturbation in Cartesian coordinate system can be Fourier analyzed as

$$\boldsymbol{\xi}(\mathbf{r}, t) = \xi(z)\text{exp}(\Gamma t + ik_x x + ik_y y) \tag{B.4}$$

In cylindrical coordinate system, it is

$$\boldsymbol{\xi}(\mathbf{r}, t) = \xi(r)\text{exp}(\Gamma t + im\theta + jkz) \tag{B.5}$$

Thus we can derive an equation for the z component of the displacement vector in Cartesian coordinate system:

$$\frac{d}{dz}(K\frac{d\xi_z}{dz}) - L\xi_z = 0. \tag{B.6}$$

with the definition of

$$\begin{cases} K = \dfrac{1}{D}(\rho\Gamma^2 + F^2)[\rho\Gamma^2(\dfrac{B^2}{4\pi} + \gamma P) + \gamma P F^2], \\ \\ L = \rho\Gamma^2 + F^2 + g\dfrac{d\rho}{dz} - (g^2k^2\rho^2/D)(\rho\Gamma^2 + F^2) - \dfrac{d}{dz}[\dfrac{\rho^2\Gamma^2 g}{D}(\rho\Gamma^2 + F^2)], \\ \\ D = \rho^2\Gamma^2 + k^2[\rho\Gamma^2(\gamma P + \dfrac{B^2}{4\pi}) + \gamma P F^2)], \\ \\ F = \dfrac{1}{4\pi}(k_x B_x + k_y B_y), \\ \\ k^2 = k_x^2 + k_y^2,\ B^2 = B_x^2 + B_y^2. \end{cases}$$

where γ is the specific heat ratio. In cylindrical coordinate system, Eq. (B.6) can be rewritten as

$$\frac{d}{dr}(\frac{K}{r}\frac{d}{dr}(r\xi_r)) - L\xi_r = 0. \tag{B.7}$$

where

$$\begin{cases} K = \dfrac{1}{D}(\rho\Gamma^2 + F^2)[\rho\Gamma^2(\dfrac{B^2}{4\pi} + \gamma P) + \gamma P F^2], \\ \\ L = \rho\Gamma^2 + F^2 + \dfrac{B_\phi}{2\pi}\dfrac{d}{dr}(\dfrac{B_\phi}{r}) - \dfrac{k^2 B_\phi^2}{\pi r^2 D}(\rho\Gamma^2\dfrac{B^2}{4\pi} + \gamma P F^2) - \\ \\ r\dfrac{d}{dr}\{\dfrac{kB_\phi}{2\pi r^2 D}(kB_\phi - \dfrac{m}{r}B_z)[\rho\Gamma^2(\dfrac{B^2}{4\pi} + \gamma P) + \gamma P F^2]\}, \\ \\ D = \rho\Gamma^4 + (k^2 + \dfrac{m^2}{r^2})[\rho\Gamma^2(\dfrac{B^2}{4\pi} + \gamma P) + \gamma P F^2], \\ \\ B^2 = B_\phi^2 + B_z^2,\ F = \dfrac{1}{4\pi}(kB_z + \dfrac{m}{r}B_\phi), \end{cases}$$

The well-known expression of the classical growth rate of perturbation in linear regime is

$$\Gamma = \sqrt{|gk|} \tag{B.8}$$

We discuss this problem in the Cartesian coordinate system. Let us choose $z = 0$ to be the lower boundary of the plasma, $\mathbf{B} = B_1\vec{\mathbf{e}}_y$ in the lower half-space,$\mathbf{k} = k\vec{\mathbf{e}}_x$,$\rho(0) = 0$, and the magnetic field to be continuous at $z = 0$; then we find $F^2 = k^2B_x^2/4\pi$. Integrating the equilibrium force equation (B.2), we find

$$\frac{B_x^2}{8\pi} + \frac{1}{8\pi}(B_y^2 - B_1^2) + P = \int_0^z g\rho(z')dz' \tag{B.9}$$

Let us, for simplicity, restrict our discussion to the power-law density profiles, $\rho = \rho_0(z/h)^s$, near the boundary. Then we have

$$F^2 = (k^2B_{||}^2/4\pi)(z/h)^{s+1}, \tag{B.10}$$

where h is the characteristic length of the non-uniformity in the z direction and ρ_0 and $B_{||}^2$ are the characteristic values of the plasma density and $(\mathbf{k}\cdot\mathbf{B})^2/k^2$, respectively. The influence of axial magnetic field is characterized by the dimensionless parameter

$$\chi^2 = B_{||}^2/4\pi\rho_0 sh|g| \tag{B.11}$$

In the limit $\chi \to 0$, the growth rate of MRT instability is given by (B.8), as it should be. In the opposite case when $\chi \ll 1$, the MRT instability is stabilized by the magnetic field. A rough estimate of the growth rate reads

$$\Gamma \approx |gk|^{1/2}2^{7/4}(s\chi)^{1/2}\text{exp}(-\pi\chi/2) \tag{B.12}$$

shows that the value of Γ can be made arbitrary small, if the value of χ is sufficiently high. If the magnetic field below (B_1) and above (B_2) a plasma layer of finite thickness, d, are perpendicular to each other, then the layer acceleration and parameter χ can be estimate as

$$g \approx (B_1^2 - B_2^2)/8\pi\rho_0 d, \tag{B.13}$$

and

$$\chi^2 \approx \min(B_1^2, B_2^2)/|B_1^2 - B_2^2|. \tag{B.14}$$

Bibliography

[1] C. Mack. *Fundamental principles of optical lithography: the science of microfabrication*. Wiley, Hoboken, NJ, USA, (2008).

[2] H. Xiao. *Introduction to semiconductor manufacturing technology*. Prentice Hall, Upper Saddle River, NJ, USA, (2001).

[3] G. E. Moore. "Cramming more components onto integrated circuits". *Electronics*, **38**, 114, (1965).

[4] B. Fay. "Advanced optical lithography development, from uv to euv". *Microtron. Eng.*, **61**, 11, (2001).

[5] J. Finders, M. Dusa, P. Nikolsky, Y. Van Dommelen, R. Watso, T. Vandeweyer, T. Beckaert, B. Laenens, and L. Van Look. "Litho and patterning challenges for memory and logic applications at the 22-nm node". *Proc. SPIE*, **7640**, 76400C1, (2010).

[6] T. Castenmiller, F. van de Mast, T. De Kort, C. van de Vin, M. De Wit, R. Stegen, and S. van Cleef. "2010 towards ultimate optical lithography with NXT:1950i dual stage immersion platform". *Proc. SPIE*, **7640**, 76401N, (2010).

[7] I. Bouchoms, J. Mulkens, S. De Putter, P. Gunter, R. De Graaf, M. Beems, E. Verdurnen, H Jasper, N. Dieckmann N, and F. Bornebroek. "2010 advanced imaging with 1.35 NA immersion systems for volume production". *Proc. SPIE*, **7640**, 76401R1, (2010).

[8] Banqiu Wu and Ajay Kumar. “Extreme ultraviolet lithography: A review”. *J. Vac. Sci. Technol. B*, **25**, 1743, (2007).

[9] V. Bakshi. *EUV Lithography*. SPIE, Bellingham, WA, USA, (2008).

[10] J. Miyazaki. “EUV lithography into production at chipmakers: update on ASML’s NXE platform”. In *SEMATECH symposium Japan and ISMI regional meeting series*, Tokyo, Japan, 22 June 2011.

[11] T. Namioka. “Current research activities in the field of multilayers for soft-rays in Japan”. *Revue. Phys. Appl.*, **23**, 1711, (1988).

[12] W. T. Silfvast and O. R. Wood II. “Tenth micro lithography with a 10 Hz 37.2 nm sodium laser”. *Microelectron. Eng.*, **8**, 3, (1988).

[13] A. M. Hawryluk and L. G. Seppala. “Soft x-ray projection lithography using a x-ray reduction camera”. *J. Vac. Sci. Technol. B*, **6**, 2162, (1988).

[14] J. Bjorkholm, J. Bokor, L. Eichner, R. R. Freeman, J. Gregus, T. E. Jewell, W. M. Mansfield, A. A. MacDowell, E. L. Raab, W. T. Silfvast, L. H. Szeto, D. M. Tennant, W. K. Waskiewicz, D. L. While, D. L. Windt, O. R. Wood II, and J. H. Burning. “Reduction imaging using multipayer coated optics: printing of features smaller than 0.1 microns”. *J. Vac. Sci. Technol. B*, **8**, 1509, (1990).

[15] A. M. Hawryluk and N. M. Ceglio. In *OSA Proceedings on Extreme Ultraviolet Lithography*, Monterey, CA, 19-21 Sept. 1994.

[16] D. R. Kania, D. P. Gaines, M. Hermann, and J. Honig. In *OSA Proceedings on Extreme Ultraviolet Lithography*, Monterey, CA, 19-21 Sept. 1994.

[17] M. Mermann, J. Honig, and L. Hackel. In *OSA Proceedings on Extreme Ultraviolet Lithography*, Monterey, CA, 19-21 Sept. 1994.

[18] R. C. Spitzer and D. P. Gaines. In *OSA Proceedings on Extreme Ultraviolet Lithography*, Monterey, CA, 19-21 Sept. 1994.

[19] G. D. Kubiak, K. D. Kren, K. W. Berger, T. G. Trucano, P. W. Fisher, and M. J. Gouge. In *OSA Proceedings on Extreme Ultraviolet Lithography*, Monterey, CA, 19-21 Sept. 1994.

[20] A. M. Hawryluk, D. R. Kania, P. Celliers, L. DaSilva, A. Stith, D. Stewart, and S. Mrowka. In *OSA Proceedings on Extreme Ultraviolet Lithography*, Monterey, CA, 19-21 Sept. 1994.

[21] D. R. Kania, F. J. Weber, S. P. Veron, A. Hawryluk, and S. L. Baker. In *OSA Proceedings on Extreme Ultraviolet Lithography*, Monterey, CA, 19-21 Sept. 1994.

[22] S. P. Vermon, M. J. Carey, D. P. Gaines, and F. J. Weber. In *OSA Proceedings on Extreme Ultraviolet Lithography*, Monterey, CA, 19-21 Sept. 1994.

[23] D. P. Gaines, S. P. Vermon, G. E. Sommargren, and D. R. Kania. In *OSA Proceedings on Extreme Ultraviolet Lithography*, Monterey, CA, 19-21 Sept. 1994.

[24] K. Skulina, C. Alford, R. Bionta, D. Makowiecki, E. M. Gullikson, R. Soufli, J. B. Kortright, and J. H. Underwood. In *OSA Proceedings on Extreme Ultraviolet Lithography*, Monterey, CA, 19-21 Sept. 1994.

[25] C. Cerjan. In *OSA Proceedings on Extreme Ultraviolet Lithography*, Monterey, CA, 19-21 Sept. 1994.

[26] D. P. Gaines, S. P. Vermon, G. E. Sommargren, and D. Fuchs. In *OSA Proceedings on Extreme Ultraviolet Lithography*, Monterey, CA, 19-21 Sept. 1994.

[27] G. E. Sommargren. In *OSA Proceedings on Extreme Ultraviolet Lithography*, Monterey, CA, 19-21 Sept. 1994.

[28] S. J. Cohen and L. G. Seppala. In *OSA Proceedings on Extreme Ultraviolet Lithography*, Monterey, CA, 19-21 Sept. 1994.

[29] S. P. Vermon and S. L. Baker. In *OSA Proceedings on Extreme Ultraviolet Lithography*, Monterey, CA, 19-21 Sept. 1994.

[30] P. D. Rockett, J. A. Hunter, G. D. Kubiak, K. Krenz, H. S. Shields, and M. Powers. In *OSA Proceedings on Extreme Ultraviolet Lithography*, Monterey, CA, 19-21 Sept. 1994.

[31] K. B. Nguyen, P. Resnick, B. Draper, P. Mahl, J. H. Underwood, D. Chen, and P. Denham. In *OSA Proceedings on Extreme Ultraviolet Lithography*, Monterey, CA, 19-21 Sept. 1994.

[32] A. K. Ray-Chaudhuri, R. H. Stulen, W. Ng, and F. Certina. In *OSA Proceedings on Extreme Ultraviolet Lithography*, Monterey, CA, 19-21 Sept. 1994.

[33] D. A. Tichenor, A. K. Ray-Chaudhuri, G. D. Kubiak, and S. J. Haney. In *OSA Proceedings on Extreme Ultraviolet Lithography*, Monterey, CA, 19-21 Sept. 1994.

[34] W. C. Sweatt and W. W. Chow. In *OSA Proceedings on Extreme Ultraviolet Lithography*, Monterey, CA, 19-21 Sept. 1994.

[35] T. D. Nguyen, C. Khan-Malek, and J. H. Underwood. In *OSA Proceedings on Extreme Ultraviolet Lithography*, Monterey, CA, 19-21 Sept. 1994.

[36] J. H. Underwood, E. M. Gullikson, W. Ng, A. Ray-Chaudhuri, and F. Cerrina. In *OSA Proceedings on Extreme Ultraviolet Lithography*, Monterey, CA, 19-21 Sept. 1994.

[37] K. A. Goldberg, R. Beguiristain, J. Bokor, and H. Medecki. In *OSA Proceedings on Extreme Ultraviolet Lithography*, Monterey, CA, 19-21 Sept. 1994.

[38] D. C. Lee and A. R. Neureuther. In *OSA Proceedings on Extreme Ultraviolet Lithography*, Monterey, CA, 19-21 Sept. 1994.

[39] D. L. Windt and W. K. Waskiewicz. In *OSA Proceedings on Extreme Ultraviolet Lithography*, Monterey, CA, 19-21 Sept. 1994.

[40] Z. Tan, A. A. MacDowell, B. La Fontaine, , and J. Russo. In *OSA Proceedings on Extreme Ultraviolet Lithography*, Monterey, CA, 19-21 Sept. 1994.

[41] B. La Fontaine, D. L. White, A. A. MacDowell, Z. Tan, D. M. Tennant, and O. R. Wood. In *OSA Proceedings on Extreme Ultraviolet Lithography*, Monterey, CA, 19-21 Sept. 1994.

[42] B. La Fontaine, A. A. McDowell, Z. Tan, G. N. Taylor, D. L. White, D. M. Tennant, and O. R. Wood II. In *OSA Proceedings on Extreme Ultraviolet Lithography*, Monterey, CA, 19-21 Sept. 1994.

[43] O. R. Wood, J. E. Bjorkholm, K. F. Dreyer, L. Fetter, and M. D. Himel. In *OSA Proceedings on Extreme Ultraviolet Lithography*, Monterey, CA, 19-21 Sept. 1994.

[44] G. N. Taylor, R. S. Hutton, S. M. Stein, C. H. Boyce, B. La Fontaine, A. MacDowell, and D. R. Wheeler. In *OSA Proceedings on Extreme Ultraviolet Lithography*, Monterey, CA, 19-21 Sept. 1994.

[45] F. Jin and M. Richardson. In *OSA Proceedings on Extreme Ultraviolet Lithography*, Monterey, CA, 19-21 Sept. 1994.

[46] M. Richardson and F. Jin. In *OSA Proceedings on Extreme Ultraviolet Lithography*, Monterey, CA, 19-21 Sept. 1994.

[47] F. Cerrina. In *OSA Proceedings on Extreme Ultraviolet Lithography*, Monterey, CA, 19-21 Sept. 1994.

[48] B. M. Lum and A. R. Neureuther. In *OSA Proceedings on Extreme Ultraviolet Lithography*, Monterey, CA, 19-21 Sept. 1994.

[49] K. B. Nguyen, D. T. Attwood, T. Mizota, T. Haga, and H. Kinoshita. In *OSA Proceedings on Extreme Ultraviolet Lithography*, Monterey, CA, 19-21 Sept. 1994.

[50] H. Kinoshita, K. Kuirhara, Y. Ishii, and Y. Torii. “Soft x-ray reduction lithography using multilayer mirrors”. *J. Vac. Sci. Technol. B*, **7**, 1648, (1989).

[51] Y. Saito. In *OSA Proceedings on Extreme Ultraviolet Lithography*, Monterey, CA, 19-21 Sept. 1994.

[52] H. Takenaka, T. Kawamura, Y. Ishii, T. Haga, and H. Kinoshita. In *OSA Proceedings on Extreme Ultraviolet Lithography*, Monterey, CA, 19-21 Sept. 1994.

[53] K. Murakami, H. Nagata, M. Ohtani, H. Oizumi, Y. Yamashita, and N. Atoda. In *OSA Proceedings on Extreme Ultraviolet Lithography*, Monterey, CA, 19-21 Sept. 1994.

[54] K. Suzuki, A. Miyake, and N. Harned. “Joint requirements for EUV source”. In *2009 International symposium on extreme ultraviolet lithography*, Prague, Czech Republic, 18-21 Oct. 2009.

[55] V. Banine, S. Young, and R. Moores. “EUV Lithography: today and tomorrow”. In *2012 International Workshop on EUV and Soft X-ray Sources*, Dublin, Ireland, 8-12 Oct. 2012.

[56] D.T. Attwood. *Soft X-rays and EUV radiation*. Cambridge University Press, Cambridge, UK, (1999).

[57] D. G. Stearns, R. S. Rosen, and S. P. Vernon. “Multilayer mirror technology for soft-x-ray projection lithography”. *Appl. Opt.*, **32**, 6952, (1993).

[58] A. M. Hawryluk and N. M. Ceglio. “Wavelength considerations in soft-x-ray projection lithography”. *Appl. Opt.*, **32**, 7062, (1993).

[59] H. Kinoshita, K. Kurihara, Y. Ishii, and Y. Torii. “Soft-x-ray reduction lithography using multilayer mirrors”. *J. Vac. Sci. Technol. B*, **7**, 1648, (1989).

[60] B. Wu and A. Kumar. *Extreme Ultraviolet Lithography*. McGraw-Hill, New York, USA, 2009.

[61] E. R. Kieft. *Transient behavior of EUV emitting discharge plasmas: a study by optical methods*. PhD thesis, Eindhoven University of Technology, 2005.

[62] V. Banine, J. Benschop, M. Leenders, and R. Moors. "The relationship between an EUV source and the performance of an EUV lithographic system". *Proc. SPIE*, **3997**, 126, (2000).

[63] R. Stuik. *Characterization of XUV sources*. PhD thesis, Eindhoven University of Technology, 2000.

[64] E. R. Kieft, K. Garloff, J. J. A. M. Van der Mullen, and V. Banine. "Comparison of experimental and simulated extreme ultraviolet spectra of xenon and tin discharges". *Phys. Rev. E*, **71**, 036402, (2005).

[65] T. Tomie *et al.* "Use of tin as a plasma source material for high conversion efficiency". *Proc. SPIE*, **5037**, 147, (2003).

[66] M. Richardson, C. S. Koay, K. Takenoshita, C. Keyser, and M. Al-Rabban. "High conversion efficiency mass-limited Sn-based laser plasma source for extreme ultraviolet lithography". *J. Vac. Sci. Technol. B*, **22**, 785, (2004).

[67] I. V. Fomenkov *et al.* "Laser-produced plasma source system development". *Proc. SPIE*, **6517**, 65173, (2007).

[68] Y. Ueno, G. Soumagne, A. Sumitani, A. Endo, and T. Higashiguchi. "Enhancement of extreme ultraviolet emission from a CO2 laser-produced Sn plasma using a cavity target". *Appl. Phys. Lett.*, **91**, 231501, (2007).

[69] K. Nishihara, A. Sunahara, A. Sasaki, M. Nunami1, H. Tanuma, S. Fujioka, Y. Shimada, K. Fujima, H. Furukawa, T. Kato, F. Koike, R. More, M. Murakami, T. Nishikawa, V. Zhakhovskii, K. Gamata, A. Takata, H. Ueda, H. Nishimura, Y. Izawa, N. Miyanaga, and K. Mima. "Plasma physics and radiation hydrodynamics in developing an extreme ultraviolet light source for lithography". *Phys. Plasmas*, **15**, 056708, (2008).

[70] S. S. Harilal, T. Sizyuk, V. Sizyuk, and A. Hassanein. "Efficient laser-produced plasma extreme ultraviolet sources using grooved Sn targets". *Appl. Phys. Lett.*, **96**, 111503, (2010).

[71] S. F. Horne, F. M. Niell, M. J. Partlow, M. M. Besen, D. K. Smith, P. A. Blackborow, and D. Gustafson. "Development of a high pulse rate EUV source". *Proc. SPIE*, **7271**, 72713A, (2009).

[72] R. Lebert, U. Wiesemann, D. Schafer, T. Wilhein, C. Phiesel, D. Esser, M. Hoefer, D. Hoffmann, K. Bergmann, and H. Stiel. "The request for high-brilliant XUV sources: a first principle approach". In *2010 International Workshop on Extreme Ultraviolet Sources*, Dublin, Ireland, 13-15 Nov. 2010.

[73] T. Tomie, T. Aota, Y. Ueno, G. Niimi, H. Yashiro, J. Lin, I. Matsushima, K. Komiyama, D. Lee, K. Nishigori, and H. Yokota. "Use of tin as a plasma source material for high conversion efficiency". *Proc. SPIE*, **5037**, 147, (2003).

[74] M. Richardson, C. S. Koay, K. Takenoshita, C. Keyser, and M. Al-Rabban. "High conversion efficiency mass-limited Sn-based laser plasma source for extreme ultraviolet lithography". *J. Vac. Sci. Technol. B*, **22**, 785, (2004).

[75] I. V. Fomenkov, D. C. Brandt, A. N. Bykanov, A. I. Ershov, W. N. Partlo, D. W. Myers, N. R. Böwering, G. O. Vaschenko, O. V. Khodykin, J. R. Hoffman, Ernesto Vargas L., R. D. Simmons, J. A. Chavez, and C. P. Chrobak. "Laser-produced plasma source system development". *Proc. SPIE*, **6517**, 65173J–1, (2007).

[76] V. Bakshi. *EUV sources for Lithography*. SPIE, Bellingham, WA, USA, 2005.

[77] V. Y. Banine, K. N. Koshelev, and G. H. P. M. Swinkels. "Physical processes in EUV sources for microlithography". *J. Phys. D*, **44**, 253001, (2011).

[78] S. Fujioka, H. Nishimura, K. Nishihara, A. Sasaki, A. Sunahara, T. Okuno, N. Ueda, . Ando, Y. Tao, Y. Shimada, K. Hashimoto, M. Yamaura, Keiji Nagai1

Takayoshi Norimatsu1 Takeshi Nishikawa4 N. Miyanaga Keisuke Shigemori1, Mitsuo Nakai1, Y. Izawa, and K. Mima. “Opacity Effect on Extreme ultraviolet radiation from laser-produced tin plasmas”. *Phys. Rev. Lett.*, **95**, 235004, (2005).

[79] M. Lysaght, D. Kilbane, N. Murphy, A. Cummings, P. Dunne, and G. O’Sullivan. “Opacity of neutral and low ion stages of sn at the wavelength 13.5 nm used in extreme-ultraviolet lithography”. *Phys. Rev. A*, **72**, 014502, (2005).

[80] K. Bergmann, G. Schriever, O. Rosier, M. Müller, W. Neff, and R. Lebert. “Highly Repetitive, Extreme-Ultraviolet Radiation Source Based on a Gas-Discharge Plasma”. *Appl. Opt.*, **38**:5413, (1999).

[81] U. Stamm. “Extreme Ultraviolet light sources for use in semiconductor lithography: state of the art and future development”. *J. Phys. D*, **37**, 3244, (2004).

[82] V. M. Borisov, A. V. Eltsov, A. S. Ivanov, Y. B. Kiryukhin, O. B. Khristoforov, V. A. Mishchenko, A. V. Prokofiev, A. Y. Vinokhodov, and V. A. Vodchits. “EUV sources using Xe and Sn discharge plasmas”. *J. Phys. D*, **37**, 3254, (2004).

[83] I. V. Fomenkov, N. Böwering, C. L. Rettig, S. T. Melnychuk, I. R. Oliver, J. R. Hoffman, O. V. Khodykin, R. M. Ness, and W. N. Partlo. “EUV discharge light source based on a dense plasma focus operated with positive and negative polarity”. *J. Phys. D*, **37**, 3266, (2004).

[84] J. Pankert $et\ al.$ “2006 EUV sources for the alpha-tools”. *Proc. SPIE*, **6151**, 61510Q, (2006).

[85] W. H. Bennett. “Magnetically self-focussing streams”. *Phys. Rev.*, **45**, 890, (1934).

[86] B. A. M. Hansson. *Laser-plasma sources for extreme-ultraviolet lithography*. PhD thesis, KTH Physics, 2003.

[87] M. A. Liberman, J. S. De Groot, A. Toor, and R. B. Spielman. *Physics of High-Density Z-Pinch Plasmas*. Springer, New York, USA, 1999.

[88] D. D. Ryutov, M. S. Derzon, and M. K. Matzen. “The physics of fast Z pinches”. *Rev. Mod. Phys.*, **72**, 167, (2000).

[89] W. G. Chace and H. K. Moore. *Exploding Wires. Volume 4, Proceedings of the Conference on the Exploding Wire Phenomenon (4th)*. Plenum Press, NY, USA, (1968).

[90] E. Ruden, H. U. Rahman, A. Fisher, and N. Rostoker. “Stability enhancement of a low initial density hollow gas-puff Z pinch by e^- beam preionization”. *J. Appl. Phys.*, **61**, 1131, (1987).

[91] T. Miyamoto. “Analysis of high-density Z-pinches by a snowplow energy equation”. *Nucl. Fusion*, **24**, 337, (1984).

[92] J. P. Freidberg. “Ideal magnetohydrodynamic theory of magnetic fusion systems”. *Rev. Mod. Phys.*, **54**, 801, (1982).

[93] M. Masnavi, M. Nakajima, E.Hotta, K. Horioka, G. Niimi, and A. Sasaki. “Estimation of optimum density and temperature for maximum efficiency of tin ions in Z discharge extreme ultraviolet sources”. *J. Appl. Phys.*, **101**, 033306, (2007).

[94] A. Bar-Shalom, M. Klapisch, and J. Oreg. “HULLAC, an integrated computer package for atomic processes in plasmas”. *J. Quant. Spectrosc. Radiat. Transf.*, **71**, 169, (2001).

[95] N. Bowering, M. Martins, W. N. Partlo, and I. V. Fomenkov. “Extreme ultraviolet emission spectra of highly ionized xenon and their comparison with model calculations”. *J. Appl. Phys.*, **95**, 16, (2004).

[96] M. Masnavi, M. Nakajima, A. Sasaki, E. Hotta, and K. Horioka. “Characteristics of Extreme Ultraviolet Radiation Conversion Efficiency of Xenon Plasma”. *Jpn. J. Appl. Phys.*, **43**, 8285, (2004).

[97] A. Hasegawa. *Plasma Instabilities and Nonlinear Effects*. Springer-Verlag, NY, USA, (1975).

[98] F. Cap. *Handbook on plasma instabilities, Volume 1*. Academic Press, Waltham, Massachusetts, USA, (1976).

[99] J. Choi, T. Yamaguchi, K. Yamamoto, T. Namihira, T. Sakugawa, S. Katsuki, and H. Akiyama. "Feasibility studies of EMTP simulation for the design of the pulsed power generator using MPC and BPFN for water treatments". *IEEE Trans. Plasma Sci.*, **34**, 1744, (2006).

[100] J. Choi, T. Namihira, T. Sakugawa, S. Katsuki, and H. Akiyama. "Simulation of 3-staged MPC using custom characteristics of magnetic cores". *IEEE Trans. Dielectrics and Electrical Insulations.*, **14**, 1025, (2007).

[101] J. Choi. "Introduction of the magnetic pulse compressor (MPC)- fundamental review and practical application". *J. Electr. Eng. Sci.*, **5**, 484, (2010).

[102] I. H. Hutchinson. *Principles of plasma diagnostics*. Cambridge University Press, Cambridge, UK, (1987).

[103] R. H. Huddlestone and S. L. Leonard. *Plasma diagnostic techniques*. Academic Press, Waltham, Massachusetts, USA, (1965).

[104] G Mettivier, M.C Montesi, and P Russo. "Design of a compact gamma camera with semiconductor hybrid pixel detectors: imaging tests with a pinhole collimator". *Nuclear Instruments and Methods in Physics Research A*, **509**, 321, (2003).

[105] T. Kreis. *Handbook of holographic interferometry: optical and digital methods*. Wiley-VCH, Weinheim, Germany, (2005).

[106] P. Hariharan. *Basics of Interferometry, 2nd edition*. Academic Press, Waltham, Massachusetts, USA, (2006).

[107] S. L. Jackson and U. Shumlak. “Abel inversion of a holographic interferogram for determination of the density profile of a sheared-flow pinch”. *Rev. Sci. Instrum.*, **81**, 033108, (2010).

[108] Hui Yang, Jie Zhang, Yingjun Li, Jun Zhang, Yutong Li, Zhenglin Chen, Hao Teng, Zhiyi Wei, and Zhengming Sheng. “Characteristics of self-guided laser plasma channels generated by femtosecond laser pulses in air”. *Phys. Rev. E*, **66**, 016406, (2002).

[109] S. S. Harilal, B. O’Shay, Y. Tao, and M. S. Tillack. “Ion debris mitigation from tin plasma using ambient gas, magnetic field and combined effects”. *Appl. Phys. B: Lasers Opt.*, **86**, 547, (2007).

[110] J. P. Allain, M. Neito, M. R. Hendricks, P. Plotkin, S. S. Harilal, and A. Hassanein. “IMPACT: A facility to study the interaction of low-energy intense particle beams with dynamic heterogeneous surfaces”. *Rev. Sci. Instrum.*, **78**, 113105, (2007).

[111] S. S. Harilal, M. S. Tillack, Y. Tao, B. O’Shay, R. Paguio, and A. Nikroo. “Extreme-ultraviolet spectral purity and magnetic ion debris mitigation by use of low-density tin targets”. *Opt. Lett.*, **31**, 1549, (2006).

[112] Y. Ueno, G. Soumagne, A. Sumitani, A. Endo, T. Higashiguchi, and N. Yugami. “Reduction of debris of a CO_2 laser-produced Sn plasma extreme ultraviolet source using a magnetic field”. *Appl. Phys. Lett.*, **92**, 211503, (2008).

[113] V. Sizyuk, Vivek Bakshi, and A. Hassanein. “Modeling and optimization of debris mitigation systems for laser and discharge-produced plasma in extreme ultraviolet lithography devices”. *J. Micro/Nanolith. MEMS MOEMS.*, **6**, 043003, (2007).

[114] S. Bollanti, F. Bonfigli, E. Burattini, P. Di Lazzaro, F. Flora, A. Grilli, T. Letardi, N. Lisi, A. Marinai, L. Mezi, D. Murra, and C. Zheng. “High-efficiency clean

EUV plasma source at 10–30 nm, driven by a long-pulse-width excimer laser". *Appl. Phys. B: Lasers Opt.*, **76**, 277, (2003).

[115] Y. Tao, M. S. Tillack, S. S. Harilal, K. L. Sequoia, and F. Najmabadi. "Investigation of the interaction of a laser pulse with a preformed gaussian sn plume for an extreme ultraviolet lithography source". *J. Appl. Phys.*, **101**, 023305, (2007).

[116] S. S. Harilal, B. O'Shay, M. S. Tillack, Y. Taoand R. Paguio, A. Nikroo, and C. A. Back. "Spectral control of emissions from tin doped targets for extreme ultraviolet lithography". *J. Phys. D*, **39**, 484, (2006).

[117] T. Okuno, S. Fujioka, H. Nishimura, Y. Tao, K. Nagai, Q. Gu, N. Ueda, T. Ando, K. Nishihara, T. Norimatsu, N. Miyanaga, Y. Izawa, K. Mima, A. Sunahara, H. Furukawa, and A. Sasaki. "Low-density tin targets for efficient extreme ultraviolet light emission from laser-produced plasmas". *Appl. Phys. Lett.*, **88**, 161501, (2006).

[118] R. Janmohamed, G. Redman, and Y. Y. Tsui. "Space charge effects in Faraday cup ion detectors". *IEEE Trans. Plasma Sci.*, **34**, 455, (2006).

[119] C. Stallings, K. Childers, I. Ross, and R. Schneider. "Imploding argon plasma experiments". *Appl. Phys. Lett.*, **35**, 524, (1979).

[120] R. Bracewell. *The Fourier Transform and its Applications*. McGraw-Hill, NY. USA, (1965).

[121] National Institute of Standard Technology. URL `http://physics.nist.gov/PhysRefData/ASD/lines_form.html`.

[122] R. W. Coons, S. S. Harilal, D. Campos, and A. Hassanein. "Analysis of atomic and ion debris features of laser-produced Sn and Li plasmas". *J. Appl. Phys.*, **108**, 063306, (2010).

[123] K. T. Lee, S. H. Kim, D. Kim, and T. N. Lee. “Numerical study on the dynamics of Z-pinch carbon plasma ”. *Phys. Plasmas*, **3**, 4, (1996).

[124] R. J. Leveque. *Finite volume methods for hyperbolic problems*. Cambridge University Press, Cambridge , UK, (2002).

[125] L. D. Landau and E. M. Lifshits. *The classical theory of fields*. Butterworth Heinemann, Oxford, UK, (1995).

[126] L. Spitzer. *Physics of fully ionized gases, 2nd edition*. Interscience Publishers, New York, USA, 1962.

[127] D. Duchs and H. R. Griem. “Computer study of the dynamic phase of a small θ pinch”. *Phys. Fluids*, **9**, 1099, (1966).

[128] N. H. Burnett and A. A. Offenberger. “Magnetohydrodynamic behavior of a laser-heated solenoid”. *Comput. Phys. Commun.*, **45**, 2155, (1974).

[129] D. Colombant and G. F. Tonon. “X-ray emission in laser-produced plasmas”. *J. Appl. Phys.*, **44**, 3524, (1973).

[130] A. Harten. “High-resolution schemes for hyperbolic conservation-laws”. *J. Comp. Phys*, **49**, 357, (1983).

[131] P. J. Roach. *Computational fluid dynamics*. Hermosa Publishers, Albuquerque, NM, USA, (1976).

[132] C. W. Shu and S. Osher. “Efficient implementation of essentially non-oscillatory shock-capturing schemes”. *J. Comp. Phys.*, **77**, 439, (1988).

[133] G. Toth and D. Odstrcil. “Comparison of some Flux Corrected Transport and Total Variation Diminishing Numerical Schemes for Hydrodynamic and Magnetohydrodynamic Problems”. *J. Comp. Phys.*, **128**, 82, (1996).

[134] G. Toth, R. Keppens, and M. A. Botchev. “Implicit and semi-implicit schemes in the Versatile Advection Code: numerical tests”. *Astron. Astrophys.*, **332**, 1159, (1998).

[135] O. V. Diyankov, I. V. Glazurin, and S. V. Koshelev. “MAG—Two-Dimensional Resistive MHD Code using an Arbitrary Moving Coordinate System”. *Comput. Phys. Commun.*, **106**, 76, (1997).

[136] G. Toth. “The $\nabla \cdot \mathbf{B}$ Constraint in Shock-Capturing Magnetohydrodynamics Codes”. *J. Comp. Phys.*, **161**, 605, (2000).

[137] E. Kroupp, D. Osin, A. Starobinets, V. Fisher, V. Bernshtam, L. Weingarten, Y. Maron, L. Uschmann, E. Forster, A. Fisher, M. E. Cuneo, C. Deeney, and J. L. Giuliani. “Ion temperature and hydrodynamic-energy measurements in a Z-pinch plasma at stagnation”. *Phys. Rev. Lett.*, **107**, 105001, (2011).

[138] Y. Zhang, W. Jiming, D. Zihuan, D. Ning, N. Cheng, Y. Yanzhong, X. Delong, S. Shunkai, G.Tongxiang, C. Yi, H. Jun, X. Chuang, and S. Xiaojian. “Computational investigation of the magneto-Rayleigh-Taylor instability in Z-pinch implosions”. *Phys. Plasmas*, **17**, 042702, (2010).

[139] M. R. Douglas, C. Deeney, and N. F. Roderick. “Computational investigation of single mode vs multimode Rayleigh-Taylor seeding in Z-pinch implosions”. *Phys. Plasmas*, **5**, 4183, (1998).

[140] J. S. De Groot, A. Toor, S. M. Golberg, and M. A. Liberman. “Growth of the Rayleigh-Taylor instability in an imploding Z-pinch”. *Phys. Plasmas*, **4**, 737, (1997).

[141] H. R. Strauss. “Stagnation of a gas puff Z pinch”. *Phys. Plasmas*, **19**, 032705, (2012).

[142] D. L. Peterson, R. L. Bowers, J. H. Brownell, A. E. Greene, K. D. McLenithan, T. A. Oliphant, N. F. Roderick, and A. J. Scannapieco. “Two dimensional modeling of magnetically driven Rayeigh-Taylor instabilities in cylindrical Z pinches”. *Phys. Plasmas*, **3**, 368, (1996).

[143] R. L. Bowers, G. Nakafuji, A. E. Greene, K. D. McLenithan, D. L. Peterson, and N. F. Roderick. “Two dimensional modeling of x ray output from switched foil implosions on Procyon”. *Phys. Plasmas*, **3**, 3448, (1996).

[144] J. H. Hammer, J. L. Eddleman, P. T. Springer, M. Tabak, A. Toor, K. L. Wong, G. B. Zimmerman, C. Deeney, R. Humphreys, T. H. Nash, T. W. L. Sanford, R. B. Spielman, and J. S. De Groot. “Two dimensional radiation magnetohydrodynamic simulation of SATURN imploding Z pinches”. *Phys. Plasmas*, **3**, 2063, (1996).

[145] M. R. Douglas, C. Deeney, and N. F. Roderick. “Effect of Sheath Curvature on Rayleigh-Taylor Mitigation in High-Velocity Uniform-Fill, Z pinch Implosions”. *Phys. Rev. Lett.*, **78**, 4577, (1997).

[146] T. W. Hussey, N. F. Roderick, U. Shumlak, R. B. Spielman, and C. Deeney. “A heuristic model for the nonlinear Rayleigh-Taylor instability in fast Z pinches”. *Phys. Plasmas*, **2**, 2055, (1995).

[147] I. Song, K. Iwata, Y. Homma, S.R. Mohanty, M. Watanabe, T. Kawamura, A. Okino, K. Yasuoka, K. Horioka, and E. Hotta. “A comparative study on the performance of a xenon capillary Z-pinch EUV lithography light source using a pinhole camera”. *Plasma Sources Sci. Technol.*, **15**, 322, (2006).

[148] S. Katsuki, A. Kimura, Y. Kondo, H. Horita, and T. Namihira. “Effects of an axial magnetic field on Z-pinch plasmas for extreme ultraviolet sources”. *J. Appl. Phys.*, **99**, 013305, (2006).

[149] A. L. Velikovich, F. L. Cochran, and J. Davis. "Suppression of Rayleigh-Taylor Iinstability in Z-pinch Loads with Tailored Density Profiles ". *Phys. Rev. Lett.*, **77**, 853, (1996).

[150] T. W. Hussey and N. F. Roderick. "Diffusion of magnetic field into an expanding plasma shell ". *Phys. Fluids*, **24**, 7, (1981).